THÈSE

En vue de l'obtention du

DOCTORAT DE L'UNIVERSITÉ DE TOULOUSE

Délivré par :
L'Université Toulouse III – Paul Sabatier
Discipline ou spécialité :
Génie Electrique

Présentée et soutenue par :
Francesco Gullo
Le 25 Avril 2018

Titre :
ETUDE DES PROCESSUS PHYSIQUES Á
L'INTERFACE ISOLANT / POLYMERE SEMICONDUCTEUR
Title :
INVESTIGATION OF PHYSICAL PROCESS AT
POLYMER INSULATION/CONDUCTIVE FILLER INTERFACE

JURY

P. NOTINGHER	Professeur, Université Montpellier II	Rapporteur
H. KLIEM	Professeur, Université Saarland, Saarbruecken	Rapporteur
N. BERCU	Ingénieur de Recherche, LRN, Reims	Examinateur
T. CHRISTEN	Senior Principal Scientist, ABB Switzerland Ltd.	Examinateur
G. TEYSSEDRE	Directeur de Recherches CNRS, LAPLACE, Toulouse	Directeur de thèse
C. VILLENEUVE-FAURE	Maître de Conférences, Université Paul Sabatier, Toulouse	Co-directrice de thèse

---

Ecole doctorale : *Génie Electrique, Electronique et Télécommunications (GEET)*
Unité de recherche : *LAboratoire PLAsma et Conversion d'Energie (LAPLACE) UMR 5213*
Directeurs de Thèse : *Gilbert TEYSSEDRE - Christina Villeneuve-FAURE*
Rapporteurs : *Petru NOTINGHER - Herbert KLIEM*

Table of Contents

Abbreviations and Symbols

AC - Alternating Current

AFM - Atomic Force Microscopy

Al - Aluminium

AM-KPFM - Amplitude Modulation - Kelvin Probe Force Microscopy

ATR - Attenuated Total Reflexion

Au - Gold

C-AFM - Conductive Atomic Force Microscopy

CB - Carbon Black

CCD - Charge Coupled Device

CPD - Contact Potential Difference

cps - Counts Per Second (cp10s, Counts per 10 seconds)

DC - Direct Current

DSC - Differential Scanning Calorimetry

EFM - Electrostatic Force Microscopy

FDC - Force Distance Curve

FM-KPFM - Frequency Mode - Kelvin Probe Force Microscopy

FV - Force Volume

FTIR - Fourier Transform Infrared Spectroscopy

HOMO - Highest Occupied Molecular Orbital

HV - High Voltage

HVAC - High Voltage Alternating Current

HVDC - High Voltage Direct Current

IR - Infrared

KPFM - Kelvin Probe Force Microscopy

LDPE - Low Density Polyethylene

LFM - Lateral Force Microscopy

LUMO - Lowest Unoccupied Molecular Orbital

MFM = Magnetic Force Microscopy

MWS - Maxwell-Wagner-Sillars

PD - Partial discharge

PE - Polyethylene

PEA - Pulse Electro-Acoustic method

PET - Polyethylene Terephthalate

PF - Peak Force

PF-QNM - Peak-Force Quantitative NanoMechanical

PI - Polyimide

PMMA - Polymethylmethacrylate

PL-Photoluminescence

PVFD - Polyvinylidene Fluoride

RT - Room Temperature

SC - Semicon

SCLC - Space Charge Limited Currents

SSRM - Scanning Spreading Resistance Microscopy

SThM Scanning ThermoMicroscopy

TFL - Trap Filled Limit

TL - Thermostimulated Luminescence

TSC - Thermostimulated Currents

UV - Ultraviolet

VL - Vacuum Energy Level

VTFL - Voltage Trap Filled Limit

XLPE - Cross-Linked Polyethylene

Acknowledgements

The work presented in this thesis was performed in the framework of a collaboration between many people from different institutes in different nations. Without their effort the results could never have been obtained.

Firstly, I would like to thank the Laplace laboratory of Toulouse, the University Paul Sabatier (UPS) of Toulouse and the ABB Corporate Research centers of Dätwill, Switzerland, and Västeras, Sweden.

All my sincere gratitude to my two directors Dr. Gilbert Teyssedre and Dr. Christina Villeneuve-Faure, from the UPS site of the LAPLACE laboratory, for the continuous support of my Ph.D study and related research, for their patience, motivation, and immense knowledge. Their guidance helped me in all the time of research and writing of this thesis.

I wish likewise thanks Dr. Thomas Christen from the ABB Corporate Research center of Dätwill, Switzerland, to him my infinite gratitude for his valuable and constructive suggestions during the planning and development of this research work. His willingness to give his time so generously has been very much appreciated.

I wish to acknowledge the help provided by Dr. Christian Laurent, Dr. Severine Le Roy, from the Diélectriques Solides et Fiabilité (DSF) research group of the LAPLACE laboratory, as the second reader of this thesis, and I am gratefully indebted to them for their very valuable comments on this thesis.

To Dr. Henrik Hillborg and its group at the ABB Corporate Research centers of Västeras and Dr. Roman Kochetov from the ABB Corporate Research center of Dätwill, Switzerland, Sweden, I want to thank them in a special way for providing the materials and samples studied in this work and for its inputs to this project.

I am particularly grateful for the assistance given by Stephanie Balor and Vanessa Soldan of IBCG-biotoul for the ultra-cryomicrotomography.

Additionally, I would like to thank our engineers in LAPLACE, Benoît Schlegel, Jacques Salon and Cedric Trupin, who teach me to use some machines in the lab and help me dealing with some problems during my experiments.

A special thank go to all my colleagues and friends in France:

the office 215 (Louiza, Julien and Menouar) for sharing with me almost every day of these 3 beautiful years. It is all your credit for my impeccable French;

les Siciliens à Toulouse (Peppe, Adriana, Alessandro e Patrick) for the pleasure of spontaneously tell you our stories in Sicilian in front of a laid table;

all the Laplace Ph.D. students, especially in the DFS and MPP groups.

Jacopo, my guide in the lab and in Toulouse as well as best friend

I would like to thank my family for their unconditional and vital support during these years.

Last but not least, my love Marta Agati, thank you to forgiving me for the time spent working subtracted from that for us and for your constant help that every day as a rock never failed.

Résume de la Thèse an Français

Introduction Générale

Le développement de la technologie HVDC se heurte au problème de la conception et de l'optimisation des matériaux dans un contexte où les phénomènes en jeu dans les diélectriques sous contrainte DC sont loin d'être maîtrisés. En principe, le passage de la technologie AC à DC peut apparaître comme une étape facilitant la fiabilité des isolations. Premièrement sous contrainte DC, un problème important est le contrôle du champ électrique. En effet, contrairement à la contrainte AC, la distribution du champ électrique sous DC est essentiellement contrôlée par la résistivité. Contrairement à la permittivité diélectrique, qui varie modérément avec la température et très peu avec le champ électrique, la résistivité dans les diélectriques dépend essentiellement de la température et du champ, de sorte que la distribution réelle du champ est largement déterminée par les conditions de fonctionnement. De plus, des effets de charge d'espace dans les matériaux diélectriques peuvent apparaitre, notamment au niveau de divers types d'interfaces (métal/diélectrique, semi-conducteurs/isolants, diélectriques/diélectriques) et rendre difficile l'estimation de la distribution du champ électrique en régime permanent. La prédiction de l'influence de la distribution de charge sur le champ est toutefois la condition préalable la plus importante pour concevoir des dispositifs d'isolation. Cependant, pour déterminer les processus physiques en jeu aux interfaces, les conditions aux limites doivent être identifiés. De telles conditions englobent par exemple l'échange de charges à l'interface métal/électrode, ou éventuellement des processus électrochimiques résultant de la mobilité ionique dans l'isolant. Dans des matériaux purs (sans additifs ou sous-produit de réticulation) les porteurs majoritaires ne sont généralement pas intrinsèques mais injectés, il est évident que la conductance de l'isolation est fortement gouvernée par les conditions aux limites au niveau des électrodes.

Les travaux de recherche réalisés au cours de cette thèse portent sur les moyens expérimentaux à mettre en œuvre pour consolider nos connaissances actuelles sur ces processus physiques aux interfaces diélectrique/électrodes. Les principaux objectifs sont de mettre au point des méthodologies appropriées pour comprendre la relation entre les propriétés de l'interface et le comportement des propriétés électriques (conductivité macroscopique…). L'intention est de trouver des corrélations entre les propriétés de l'interface à l'échelle microscopique et le comportement électrique macroscopique. Cela permettrait également d'aider au développement de modèles de transports prenant en compte des conditions aux limites plus réaliste. Ceci implique des méthodes de caractérisation d'interface, jusqu'à l'échelle nanométrique, ainsi que des mesures physico-chimiques et électriques sur des matériaux pourvus de différentes conditions d'interface. Le projet repose sur des recherches fondamentales sur un matériau applicable aux câbles, le polyéthylène.

1. L'état de l'art

1.1. Câbles haute tension

Les câbles coaxiaux haute tension AC ou DC présente une structure similaire. Les deux sont schématiquement composés de cinq couches concentriques :

- un conducteur de noyau métallique,
- une couche de semi-conducteur interne,
- une couche d'isolation à base de polymère,
- une couche de semi-conducteur externe
- et une couche de blindage métallique. (Figure 1Figure 1-1).

Malgré cette similitude, les mécanismes qui régissent la distribution du champ électrique sont déterminés par différentes propriétés physiques. Contrairement à la contrainte AC, où la permittivité joue le rôle principal dans la détermination de la distribution du champ électrique, sous DC elle est essentiellement contrôlée par la résistivité [Vu13]. Puisque la résistivité dans les matériaux isolants dépend essentiellement de la température, la distribution du champ dans les câbles CC présente une plus grande sensibilité à la température, donc aux conditions de fonctionnement, par rapport aux câbles CA. [Vu15].

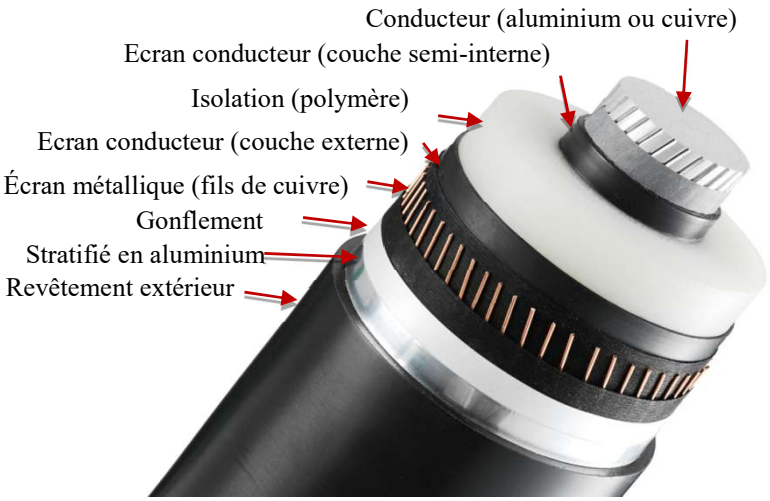

Figure 1 Couche interne dans un câble coaxial haute tension.

La prédiction de la distribution du champ électrique est le paramètre le plus important pour concevoir des dispositifs d'isolation tels que des câbles et des accessoires de câbles (par exemple des joints et des terminaisons) [Chr10]. En outre, les gradients de conductivité électrique, les effets de charge d'espace peuvent avoir un impact substantiel sur la distribution réelle du champ. Ces caractéristiques de charge d'espace sont liées, d'une part, au comportement du matériau isolant en vrac. D'autre part, les processus de génération de charge changent en fonction du comportement de contact et du type d'interface (métal / isolant, semi-conducteur / isolant, diélectrique / isolant). Ces

caractéristiques rendent difficile l'estimation de la distribution du champ électrique à la fois dans des conditions transitoires et stables [Chr15].

1.2. Matériaux isolants et semiconducteurs : présentation rapide

La large utilisation de polymères comme matériaux isolants est due non seulement à ses propriétés électriques et mécaniques, mais aussi à son faible coût de production. Les polymères définissent cette catégorie de matériaux caractérisée par la répétition, dans de longues chaînes moléculaires, d'unités chimiques appelées monomères.

1.2.1. Propriétés des polymères isolants

L'ingénierie de ces matériaux permet de contrôler les propriétés mécaniques et thermiques, par ex. en faisant varier la concentration de certains additifs. Comme l'objectif principal de cette étude est de traiter les phénomènes d'interface, les matériaux isolants étudiés doivent présenter le moins possible les phénomènes parasitaires en masse, comme par ex. transport ionique. Il doit donc être aussi pur que possible, notamment sans additifs ni résidus. Comme matériau d'isolation de référence, pour cette thèse, nous avons utilisé un polyéthylène basse densité non stabilisé d'ExxonMobil ™ sous le nom commercial “LDPE LD 101BA” [LDPE15]. Il est conçu pour l'isolation moyenne / haute tension et peut être réticulé en ajoutant la teneur en peroxyde désirée. Ce matériau est distribué sous forme de granulés et avec une fiche technique associée du fabricant qui contient les propriétés du matériau basées sur des tests standard. Ce LDPE est fourni sous forme de pastilles. Pour cette raison, en exploitant les propriétés thermoplastiques du polyéthylène, à travers les procédés décrits ci-dessous, ceux-ci sont moulés sous la forme de films ayant l'épaisseur désirée.

1.2.2. Rôle et propriétés du matériau semiconducteur

Le matériau semiconducteur (appelé «semicon» dans la suite) n’est pas un matériau semiconducteur au même sens que le silicium mais est un composite formé par du noir de carbone (CB) dispersé dans une matrice polymérique. Les particules CB, plus denses que la matrice renforce la structure du polymère améliorant l'adhérence au métal. La conductivité de ce matériau est dans la gamme de 10-5 S/m - 10 S/m. Afin d'éviter que les propriétés de contact ne soient influencées par la diffusion d'additifs et d'impuretés, un matériau semicon non commercial (SC) de haute pureté a été traité pour les besoins de la thèse. Il a été réalisé avec le même LDPE mentionné ci-dessus que la matrice et les nanoparticules de noir de carbone distribuées avec le nom commercial ”Denka Black 50% CB” a été incorporés. A cet effet, un mélangeur interne Brabender a été utilisé pour mélanger LDPE/CB (50/50 wt.%) at 15 rpm for 15 minutes at 130°C. Ensuite, il a été coupé en flocons de taille similaire à celle des pastilles de LDPE. La préparation du semicon en pastilles a été faite sur le site d'ABB Suède.

- Pour les applications HVDC, le rôle du semicon est double :
- Réduire la contrainte mécanique entre les deux matériaux avec une rigidité différente.

Deuxièmement, homogénéiser le champ électrique en lissant l'espace autour des fils de la tresse de cuivre centrale. En effet, toute saillie sur le conducteur améliore localement le champ électrique et peut déclencher le développement d'arbres électriques dans l'isolation.

1.1. Pourquoi étudier les interfaces?

Le grand progrès des techniques expérimentales utilisées pour sonder la distribution des charges d'espace dans le matériau diélectrique a permis de suivre l'accumulation de charges avec une résolution spatiale de 10 μm et une résolution temporelle de l'ordre de la microseconde [Teys17].

Pour essayer d'estimer l'influence des pièges sur cette accumulation de charge, des modélisations de niveaux électroniques moléculaires dans la structure du polyéthylène ont permis d'estimer les profondeurs des pièges introduits par ces impuretés chimiques et suggèrent comment celles-ci influent sur le dopage des polymères [Meun01] [Huza10] [Teys09] ou l'utilisation de matériaux nanocomposites [Nels14] [Ples16] La technique a été étendue récemment pour aborder le transport ionique dans les polymères [Huan17a]. Il a été observé que l'accumulation de charge [Taleb13] [Chen04] et même les mesures de conductivité [Ghor16a] dépendent, non seulement des propriétés volumiques du matériau mais également des conditions à l'interface entre l'électrode et l'isolant.

Les efforts se sont concentrés sur la possibilité de réduire l'accumulation de charges spatiales en contrôlant la pureté du matériau et la rugosité à l'interface. Une autre adaptation de l'interface a été proposée par des procédés tels que l'oxyfluoration [An09] ou en déposant des nanoparticules métalliques qui peuvent agir comme des pièges profonds à la surface et produire une diminution du champ à l'interface [Mill16].

Ghorbani et al. ont constaté que le moulage d'un échantillon de LDPE avec un film de PET influence la conduction et les pertes diélectriques. Cet effet peut être dû à la diffusion d'espèces chimiques du film de PET dans le LDPE pendant l'étape de mise en forme [Ghor16a].

Cette interface, influençant les propriétés et le comportement macroscopique, doit être caractérisée et étudiée avec précision. Les points ci-dessous sur la réponse du matériel aux propriétés de l'interface, et par conséquent, sur les potentialités ouvertes par un contrôle fin de l'interface pour améliorer encore la fiabilité des isolations. Les intérêts dans l'étude des interfaces électrode / polymère isolant peuvent être plus largement justifiés de trois points de vue:

- les isolants apparaissent comme des matériaux à largeur de bande interdite et, selon la physique des semi-conducteurs, une probabilité théorique extrêmement faible d'avoir une porteuse intrinsèque: la seule possibilité de fournir des porteurs est au moyen de processus d'injection;
- la nécessité d'améliorer nos connaissances sur les mécanismes essentiels contrôlant les processus d'échange de charge à l'interface, en ayant recours à la rugosité, la fonction chimique ou la nature de l'électrode, pour optimiser la conception ou l'adaptation de l'interface;

- trouvé le moyen de justifier les hypothèses à adopter sur les conditions aux limites pour certains cas critiques, par ex. des modèles de transport macroscopique basés sur des données de conductivité et de permittivité ou des processus de dérive-diffusion, prenant en compte la densité des porteurs, la nature du matériau et sa mobilité.

1.2. Objectifs de la thèse

Comme indiqué précédemment, les interfaces semblent avoir un fort impact sur l'injection de charges dans les polymères diélectriques. Cependant, cette influence est, jusqu'à présent, mal connus, même si de nombreuses tentatives ont été faites au cours des trente dernières années pour décrire les interfaces à différentes échelles. L'objectif principal de ce projet de recherche est de caractériser l'interface à l'échelle nanométrique et d'identifier son impact sur l'injection et le transport de charges. Pour atteindre cet objectif, le PE pur a été choisi comme matériau diélectrique pour éviter l'influence des additifs et des impuretés. Une interface semi-conducteur / PE sera étudiée en raison de son utilisation intensive pour les applications dans les câbles HVDC. Cette interface sera étudiée du point de vue macroscopique mais également nanométrique. L'originalité de notre approche réside dans l'utilisation de modes de mesure dérivés de la microscopie à force atomique (AFM) pour sonder la morphologie et les propriétés électriques de l'interface avec une résolution nanométrique. Ces caractérisations seront complétées par des mesures macroscopiques.

Cette thèse de doctorat est divisée en trois chapitres en plus du premier consacré à l'état de l'art. Le deuxième chapitre concerne à la fois le procédé de fabrication des échantillons et les méthodes de caractérisation. Les échantillons de PE et les sandwichs semicon / PE / semicon sont traités en utilisant une technique de moulage à la presse. Différentes couches protectrices (PET, Al ...) ont été utilisées pour modifier les propriétés de surface. Différentes techniques de mesure seront présentées pour caractériser:

- Propriétés chimiques de surface. À cette fin, des mesures de spectroscopie infrarouge à transformée de Fourier (FTIR) et de photoluminescence (PL) seront utilisées.
- Injection et le transport de charges à l'échelle macroscopique. Méthodes électroacoustique pulsée (PEA) et courant de polarisation / dépolarisation à résolution temporelle.
- Propriétés de l'interface à l'échelle nanométrique. Les propriétés morphologiques et électriques sont étudiées à l'aide de la microscopie Peak Force Quantitative NanoMechanical (PF-QNM) et de la microscopie à sonde de Kelvin (KPFM) respectivement.

Chaque technique sera présentée succinctement, et les conditions expérimentales seront détaillées.

Le troisième chapitre est consacré aux résultats expérimentaux, qui mettent en évidence l'influence de la couche de moulage sur les propriétés du matériau et sur le comportement électronique de l'isolant à l'interface. Ces résultats seront discutés plus avant dans le quatrième chapitre, tandis que le cinquième chapitre résumera et conclura la thèse de doctorat avec des considérations finales et des perspectives futures de la recherche sur les interfaces dans les diélectriques.

2. Fabrication des matériaux et caractérisation

2.1. Stratégie expérimentale

L'objectif principal de ce travail est de caractériser les propriétés de l'interface et de déterminer leur impact sur l'accumulation de charges. Pour atteindre cet objectif, les processus de fabrication des matériaux doivent être contrôlés avec précision, en accordant une attention particulière aux caractéristiques de surface en termes de propriétés chimiques et microstructuraux et de leur relation avec les conditions de traitement.

Pour cela les couches de PE seront moulées avec trois différent matériaux : PET, Al et polyimide (PI)

L'étape suivante consiste à proposer des outils de caractérisation complémentaires pour sonder l'interface et les phénomènes associés à une échelle pertinente. Trois types d'outils de caractérisation seront utilisés:

- Caractérisation chimique par spectroscopie photoluminescence (PL) et infrarouge à transformée de Fourier (FTIR);
- caractérisation électrique à l'échelle macroscopique ou microscopique en utilisant des mesures de courant ou des mesures de charge d'espace par la méthode de mesure de la charge d'espace par impulsions électroacoustiques (PEA);
- propriétés morphologiques et électriques à l'échelle nanométrique, en utilisant des techniques dérivées de l'AFM.

Trois types d'échantillons ont été élaborés avec des géométries adaptées aux techniques mises en œuvre pour les caractériser:

- couche diélectrique simple pour l'analyse chimique et morphologique;
- couche isolante avec des électrodes métalliques pour la caractérisation électrique;
- couche isolante avec deux électrodes semi-conductrices pour la caractérisation électrique et la mesure de la section transversale par AFM pour tester les propriétés de l'interface.

En outre, toujours dans l'objectif de garder le contrôle sur les caractéristiques des interfaces, nous avons comparé les propriétés de surface d'échantillons préparés sur différents sites, à savoir ABB Research Center Sweden et le site de Laplace, afin d'identifier toute déviation possible provenir du traitement.

2.2. Fabrication de la structure tri-couches

Les échantillons conçus pour étudier l'interface semi-conducteur / isolant présentent deux surfaces de contact parallèles, réalisées en faisant fondre deux électrodes semi-circulaires de semicon sur un film de LDPE. Pour permettre à l'AFM de sonder les propriétés de l'interface, l'échantillon a été étudié sur la tranche. La méthode de préparation peut être résumée par les quatre étapes suivantes:

- Fabrication d'un film de LDPE et de deux couches de semi-conducteurs. Les couches individuelles sont coupées au même diamètre et empilées.
- Fusion des trois couches ensemble. Autour de chaque couche est installée une bague de support ayant la même épaisseur que la couche unique (50 µm). Le protocole de pressage à chaud pour faire fondre les couches ensemble est similaire à celui pour une seule couche adoptée dans Laplace, mais la température maximale est réduite à 110 ° C. La température inférieure et l'anneau de support empêchent le mélange des trois couches entre elles. Le résultat est un échantillon de type sandwich de 150 µm d'épaisseur avec deux interfaces isolantes semi-isolantes.
- Découper l'échantillon en petits triangles dont la dimension est de quelques millimètres afin d'avoir une surface de contact plus large pour les électrodes et un support pour maintenir l'échantillon verticalement.
- Amincir un angle en utilisant l'ultra-cryo-microtome pour obtenir une surface suffisamment lisse pour permettre les mesures AMF. Cette étape a été réalisée au sein de la plateforme Biotool de IBCG. Cette méthode est couramment utilisée pour produire des échantillons organiques sous forme de film très mince comme nécessaire pour les mesures de microscopie électronique. En congelant l'échantillon dans de l'azote liquide, des tranches d'environ 200 nm d'épaisseur peuvent être produites avec la lame de diamant. Pour notre propre application, nous utilisons la surface lisse laissée sur l'échantillon de base pour effectuer des caractérisations AFM sur des sections transversales.

Cette surface fait environ 150µm de large et quelques centaines de microns de large. Après ce traitement, la surface est suffisamment plane pour mesurer les propriétés de contact en coupe transversale.

3. Caractérisation des couches seules

3.1. Caractérisation physico-chimique

Dans cette section, les résultats sur les films monocouches LDPE fabriqués avec différentes couches de protection seront analysés et leurs propriétés discutées. L'analyse chimique a été réalisée en utilisant l'interaction entre le matériau et le rayonnement électromagnétique dans deux domaines spectraux, l'infrarouge et l'ultraviolet moyen.

3.1.1. FTIR

Les mesures FTIR ont été réalisées dans la gamme 4000 cm^{-1} et 400 cm^{-1} sur un spectromètre Vertex 70 FT-IR en mode de réflexion totale atténuée de Bruker, avec l'accessoire PLATINUM Diamond ATR Ce type de mesure permet de mesurer les modes de vibration au sein des chaines de PE. Mais également de détecter la présence traces résiduelles des sous-produits de fabrication ou des contaminations induites par la couche protectrice.

Selon la littérature [Koen66], les trois composantes à 1369, 1298 et 1353 cm^{-1} peuvent être associées au mode wagging des groupes CH2, tandis que la bande faible à 1080 cm^{-1} est affectée à une fréquence squelettique dans la phase amorphe de la chaîne en polyéthylène. Seuls les composants à 1377 cm^{-1} et 889 cm^{-1} peuvent être corrélés avec le groupe CH3 communément trouvé comme terminaison des chaînes de polyéthylène. La gamme 1750-1580 cm^{-1} indique l'apparition de contaminations d'oxygène, en particulier les groupes C = O en configuration amorphe [Liang59], un pic important dans cette région est présenté en analysant le noyau des pastilles de LDPE avant d'être moulé (Figure 3-2, ligne vert). Après traitement thermique, cette bande disparaît presque totalement dans les échantillons de PEBD traités avec Al et PI (Figure 2), laissant un petit pic autour de 1722 cm^{-1} caractéristique du mode d'élongation du groupe carbonyle.

L'intensité plus élevée de ces pics, trouvés dans le LDPE traité avec PET (Figure 2, ligne rouge), peut suggérer, dans une première analyse, un degré d'oxydation plus élevé de la surface du polyéthylène, qui se produisant dans une moindre mesure à la fois pour le LPDE PI et LDPE Al, comme montré dans Figure 2 par la ligne bleue et noire respectivement. En LDPE PET est également pertinent, par rapport aux autres, la présence d'autres pics à 1263 et 1097 cm^{-1} également possiblement liée à une contamination en oxygène, les deux indiquant une liaison C-O d'étirement, résonnant à 1263 et 1097 cm^{-1}.

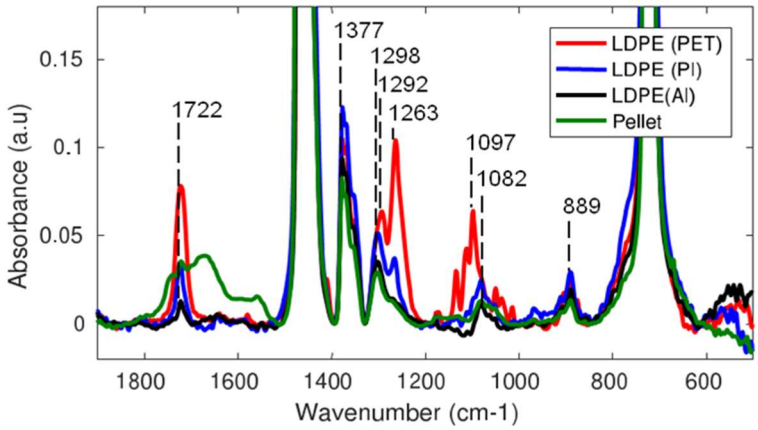

Figure 2 Zoom sur les pics d'intensité mineure des spectres FTIR de LDPE sous forme de pellets et de films traités en utilisant différentes couches protectrices.

3.1.2. Photoluminescence

Le second type de propriétés optiques sondées est la photoluminescence. En principe, deux types de spectres peuvent être enregistrés:

- spectres d'émission de photoluminescence consistant à fournir l'intensité d'émission en fonction de la longueur d'onde d'émission pour une longueur d'onde d'excitation fixe;
- spectres d'excitation de photoluminescence consistant à tracer l'intensité lumineuse contrôlée à une longueur d'onde définie en fonction de la longueur d'onde d'excitation.

Dans le polyéthylène «parfait», aucune émission ne peut être détectée dans la plage de longueur d'onde étudiée (230 nm et au-delà), car seules les liaisons sigma sont présentes. La présence de liaisons insaturées est nécessaire pour fournir une absorption. Ces liaisons peuvent être trouvées dans les défauts, les additifs et les résidus comme expliqué précédemment.

Les spectres obtenus pours des échantillons de LDPE fabriqués avec des couches de protection PET ou PI sont assez différents les uns des autres. Pour la couche de couverture PI, l'émission principale est à 340 nm (Figure 3a), et le spectre d'excitation lors de la surveillance à cette longueur d'onde révèle deux maximas à 230 et 280 nm (Figure 3a). L'émission est trouvée à 390 nm n'est pas facile à identifier où est le maximum d'excitation (Figure 3b). Par conséquent, on considère que le processus avec PI modifie l'émission obtenue à partir de pastilles en réduisant la contribution relative de l'émission à 390 nm. Considérant le cas d'Al; Figure 3b, l'émission à 390 nm est encore plus petite.

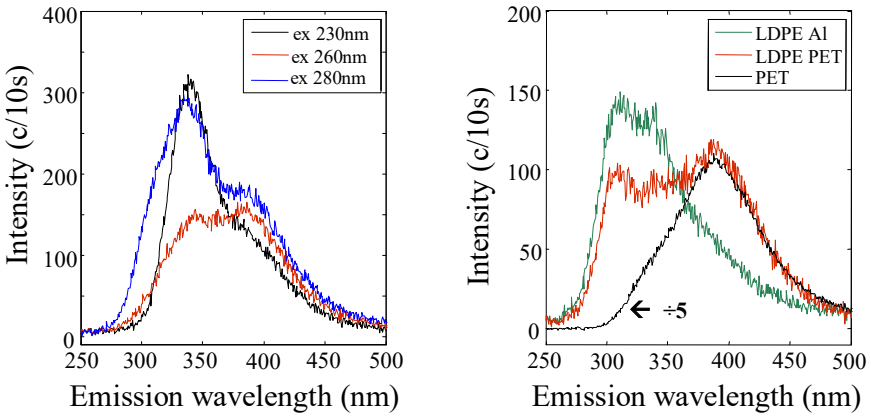

Figure 3 Spectres d'émission PL: (a) en fonction de la longueur d'onde d'excitation pour PE traité avec une couche de protection PI; (b) pour LDPE avec des couches de protection en Al ou PET par rapport au film en PET. Longueur d'onde d'excitation 280nm.

La modification de la configuration carbonyle insaturée est une possibilité. Cependant, la raison de l'efficacité spécifique au contact du PET avec tout autre processus chimique induit au contact du PET est difficile à concevoir. Donc, à ce stade, toutes les modifications chimiques ne sont pas identifiées; cependant, on peut avancer que la couche protectrice de PET induit la diffusion de fragments, qui sont éventuellement des groupes polaires.

3.2. Mesures de charge d'espace

Ces mesures ont été effectuées sur des films LDPE de 200 µm d'épaisseur fabriqués avec du PI, PET et Al comme couche de protection. Afin de réaliser ces mesures, une électrode d'or de 30 nm d'épaisseur a été déposée des deux côtés des films de LDPE. De plus, afin d'étudier si la nature de l'électrode joue un rôle dans le phénomène d'accumulation de charge d'espace, des échantillons ont également été réalisés avec une couche de 50 µm d'épaisseur en semicon (plus représentative de la structure du câble HT). De cette manière, il a été possible non seulement de comprendre l'impact de la couche protectrice utilisée lors de la préparation de l'échantillon, mais aussi l'importance de l'interface film-électrode LDPE. Les mesures ont été effectuées en appliquant une contrainte DC en utilisant des temps de charge et de décharge de 3h / 3h. Pendant les intervalles de temps de chargement, le champ a été réglé sur les valeurs 10, 20, 30 et -30 kV/mm.

Nous remarquons que la charge dominante dans le volume de l'isolateur est positive, injectée depuis l'électrode positive et s'étendant dans l'isolant. Enfin, on peut également noter que, quel que soit le signe du champ électrique, une homocharge persistante est présente à l'interface du bas pendant le temps de décharge. Ce fait est probablement lié à la configuration expérimentale.

On peut donc déduire ici, en comparant la charge d'espace accumulée, que le changement de la couche protectrice n'affecte pas qualitativement le comportement en termes d'accumulation de charge d'espace. La quantité de charges stockées semble augmenter en passant du PET au PI et aux couches de protection Al. L'augmentation plus forte de la densité de charge stockée allant du PET à d'autres

couches protectrices pourrait être liée à l'augmentation de la rugosité de surface mesurée dans l'analyse topologique monocouche. La rugosité augmenterait localement le champ sur les électrodes et favoriserait l'injection [Taleb09].

3.3. Mesures de courant de polarisation

Pour les mesures de conductivité, des électrodes en or de 50 mm de diamètre et de 30 nm d'épaisseur ont été déposées par pulvérisation cathodique. Les mesures ont été réalisées dans l'air, à 25 ou 50 ° C, en utilisant des temps de charge et de décharge de 3 h chacun. Le porte-échantillon est muni d'un fluide circulant dont la température était régulée par un thermo-cryostat, ce qui permet un contrôle rigoureux de la température. Cinq valeurs de champ comprises entre 5 et 30 kV / mm ont été appliquées consécutivement au même échantillon. Les densités de courant j normalisées par rapport au champ électrique E, (i.e. j / E) a été analysées en tant que conductivité transitoire mesurées sur chaque échantillon. La Figure 4 montre que pour les températures de 25 et 50 ° C. À 25 ° C, les courants normalisés se superposent parfaitement au cours des deux premières décades. Au temps long, il tend à augmenter avec le champ à conductivité apparemment non linéaire. En considérant les données à 50 ° C, le courant normalisé apparaît plus élevé pour la valeur de champ la plus basse de 5 kV / mm. Ensuite, il ne change pas avec le champ avant d'augmenter de nouveau pour le pas à 30 kV / mm. La caractéristique reflète peut-être les observations précédentes de Ghorbani et al. sur la diminution à long terme de la conductivité lorsque le polyéthylène était stocké en continu à 50 ° C pendant plusieurs mois [Ghor16b] [Ghor17]. La diminution de la conductivité a été observée, que l'échantillon ait été soumis ou non à un stress DC. Par conséquent, il semble correspondre à un conditionnement thermique du matériau, avec une évolution structurelle éventuellement lente due à la température

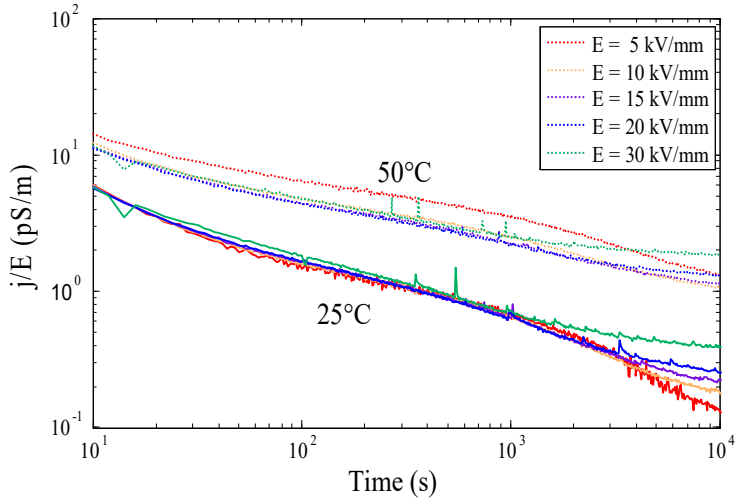

Figure 4 Transitoires de courant normalisés obtenus sur LDPE traité avec des couches de protection PI.

Le courant normalisé relativement plus élevé obtenu ici pendant les 3 premières heures à 50 ° C (plus éventuellement le temps de décharge) peut correspondre à cette forme de conditionnement. Une autre information notable est l'augmentation de la conductivité apparente, d'un facteur d'environ 5 en augmentant la température de 25 à 50° C. La pente du courant transitoire est nettement inférieure à 50° C par rapport à 25° C.

3.4. Synthèse: impact du procédé de moulage par compression sur les propriétés macroscopiques

Dans ce chapitre, nous avons évalué les différences de propriétés chimiques, structurelles et électriques qui peuvent résulter de l'utilisation de différentes couches protectrices lors du moulage par compression du polyéthylène. C'est une étape essentielle avant d'étudier de façon détaillée les propriétés électroniques des interfaces.

En termes de méthodologie nous avons étudié l'évolution de la rugosité de la surface, en analysant la rugosité basée pour des tailles d'image croissante afin de révéler des caractéristiques à des échelles spécifiques.

Les principaux résultats obtenus dans cette étude sont résumés dans le tableau 1, en fonction de la couche protectrice. Une caractéristique claire des résultats rapportés ici est l'observation de la signature spécifique par PL et IR pour l'échantillon traité avec des couches de protection PET. En FTIR, la réponse est caractéristique des groupes oxydés. En PL, une bande de fluorescence à 390 nm, qui n'est pas caractéristique des défauts connus du LDPE, est clairement identifiée. Cette bande a été détectée dans le spectre PL des couches de protection PET. Les extra-signatures ont donc été attribuées à la diffusion de groupes oxydés - des produits de décomposition ou des chaînes oligomères du PET à la surface du LDPE.

En termes de rugosité, un impact direct de la couche protectrice a pu être identifié, avec une surface nettement plus lisse utilisant la couche de protection en PET. La rugosité moyenne des différents échantillons diffère: elle varie d'environ 150 nm en utilisant PI ou Al comme couches de moulage par compression à 33 nm en utilisant des feuilles de PET.

Protecting layer	Rugosité	Fluorescence	FTIR	PEA	I(t)
Al	Rugueux	—	—	More space charge	Similaire
PI	Rugueux	—	—		
PET	Lisse	groupes oxydés/PET	C=O et C-O groupes	Moins charge d'espace	

Tableau 1 Sum-up of the impact of the protecting layer on structural and electrical properties.

Les différentes conditions de moulage par compression n'ont pas révélé de changements substantiels dans la conductivité apparente des matériaux. Selon des travaux antérieurs de Taleb et al. [Taleb09] le courant d'injection devrait être théoriquement sensiblement dépendant du profil de

surface supposant une émission thermo-ionique: ceci est lié à l'intensification du champ et à la dépendance non linéaire du champ du courant d'injection. Ceci a été rapporté pour beaucoup plus de structures grossières, avec une échelle de rugosité de l'ordre d'un µm, et des champs plus élevés que ceux étudiés ici (> 30 kV / mm). Ici, la dispersion des données de conductivité n'a pas permis de faire une comparaison fiable. La tendance pour les résultats de charge d'espace est une augmentation de la quantité de charge d'espace avec grossissement de la structure. La situation est celle des homocharges, abaissant le champ d'électrode. Il est possible que la charge piégée compense l'amélioration du champ due à la rugosité de telle sorte que le courant ne change pas dans une grande mesure. En outre, le processus de pulvérisation cathodique des électrodes en or, bien qu'évitant le chauffage des échantillons, agit éventuellement sur l'état chimique de la surface et lisse d'une certaine manière la différence d'efficacité d'injection qui pourrait apparaître par rapport aux groupes oxydés. Les résultats actuels sur la conductivité ne sont pas cohérents avec ceux de Ghorbani et al. [Ghor16b] [Ghor17] qui a trouvé une différence substantielle dans la conductivité mesurée en fonction de la couche de moulage par compression. La principale différence avec les présentes mesures concerne le type d'électrodes utilisées, c'est-à-dire les électrodes massives en laiton. Il y a éventuellement formation de petits espaces entre l'électrode et la surface du film lorsque des électrodes pulvérisées sont déposées en se conformant à la surface du film.

Enfin, nous avons obtenu des différences significatives dans les caractéristiques de charge d'espace avec interposition d'électrodes semi-conductrices. Les résultats indiquent que, à l'échelle micrométrique des mesures, la nature de l'électrode influe plus sur le comportement diélectrique apparent que les caractéristiques de surface des échantillons.

4. Propriétés de l'interface semicon/LDPE

L'objectif de ce chapitre est de caractériser l'interface entre le semicon et le LDPE d'un point de vue physique et électrique. Pour atteindre cet objectif, des sandwiches semicon/LDPE/semicon ont été réalisés et observé sur la tranche, comme décrit au chapitre 2, pour atteindre l'interface. Cette interface sera caractérisée en utilisant PF-QNM et KPFM pour tenter de déterminer la morphologie et les propriétés électriques. Pour essayer d'interpréter la mesure du potentiel de surface, une méthode est proposée pour extraire la densité de charge totale des mesures de potentiel de surface par KPFM.

4.1. Méthodologie

Les méthodologies décrites dans ce chapitre impliquent, tout d'abord, la caractérisation physique de l'interface SC / LDPE, qui comprend également la caractérisation de la rugosité de l'interface ou la diffusion éventuelle de CB dans le volume LDPE; d'autre part, la caractérisation électrique au moyen des mesures de potentiel de surface ainsi que l'algorithme de calcul du champ électrique et de la densité de charge de surface.

Une approche différente a été proposée afin d'identifier l'interface SC / LDPE basée sur l'utilisation du mode PF-QNM, notamment sur la cartographie des forces d'adhésion. Cette méthodologie représente une technique alternative au microscope optique plus traditionnel couramment utilisé ou au scan microscopique Raman [Bode06]. L'exploitation du PF-QNM permet une meilleure résolution jusqu'à l'échelle nanométrique. De plus, grâce au contraste des forces d'adhésion entre les nanoparticules CB et le LDPE, les nanoparticules diffusant dans le LDPE peuvent être détectées. De plus, une mesure précise de l'interface SC / LDPE a été définie puisque, par reconnaissance des nanoparticules CB incorporées dans le SC, il est possible de distinguer clairement la couche de SC par rapport au LDPE. Enfin, grâce à cette méthode, il est possible de mesurer la rugosité de la jonction SC / LDPE et de confirmer l'absence de diffusion des nanoparticules CB dans la couche de LDPE. La méthodologie pour la caractérisation électrique peut être appliquée sur deux modes KPFM: les modes AM-KPFM et PF-KPFM. Cette technique permet de sonder dans le même temps les propriétés morphologiques et électriques de l'interface. De cette façon, l'interface est caractérisée plus complètement que dans les études précédentes [Tana05].

4.2. Caractérisation de l'interface Semicon/LDPE

La Tableau 2 résume les mesures de rugosité d'interface semicon/LDPE réalisé par AFM en mode PF-QNM. Les résultats mettent en évidence que la température / pression du processus n'a aucune influence sur la rugosité de l'interface, alors que la nature de la couche protectrice influence fortement ce paramètre. Le film de PEBD traité avec des couches de protection en Al et PI présente une rugosité d'interface plus élevée, ce qui est cohérent avec nos conditions initiales de rugosité de surface établies avant le traitement en sandwich.

Couche de protection	LDPE largeur	Rugosité de l'interface	Déviation standard
PI	47.8µm	480nm	2%
Al	42.6µm	525nm	2.5%
PET	57.6µm	265nm	0.9%

Tableau 2 Propriétés physiques de l'interface Semicon/LDPE.

Grâce à la méthodologie d'estimation de la charge de surface développée dans cette thèse, l'influence du processus de fabrication du LDPE est étudiée.

Les profils de champ électrique et de densité de charge sont extraits à l'aide de la méthode SG-filtre 2D. Pour le LDPE traité dans Laplace et ABB, le champ électrique est constant dans chaque couche SC, présente une interface maximum (minimum) à gauche (droite) et diminue linéairement de l'électrode SC de gauche à droite. La carte de densité de charge montre une accumulation de charge proche de l'interface avec une charge négative en LDPE et une charge d'image positive dans le SC.

Contrairement au LDPE traité avec du PET ou du LDPE, l'utilisation de la couche protectrice Al conduit à une charge négative. En outre, le montant de la charge semble être inférieur à celui précédemment.

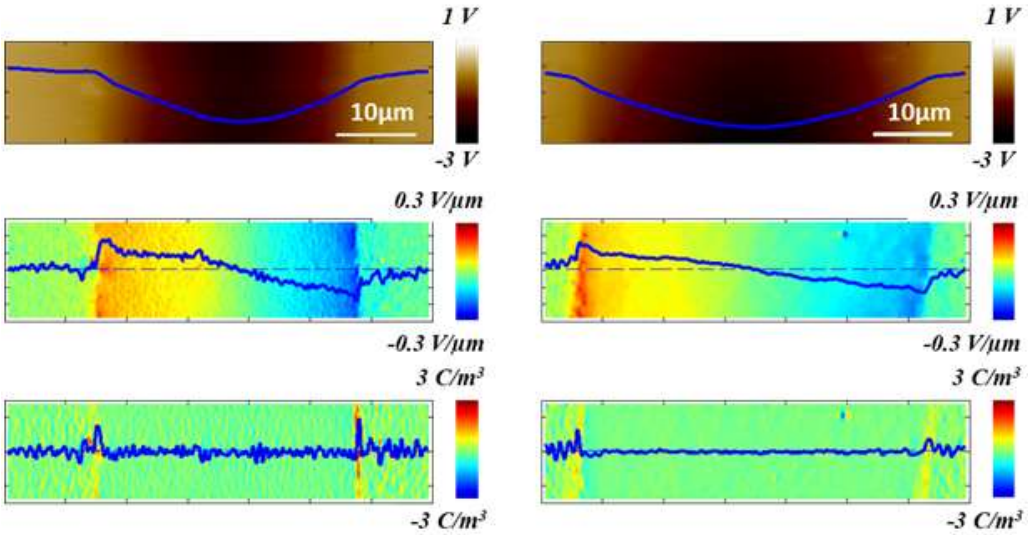

Figure 5 Comparaison du potentiel de surface (a; d), du champ électrique (b; e) et des cartes de densité de charge (c; f) pour un sandwich dont le LDPE a été traité en utilisant Al dans Laplace (rangée de gauche) et ABB (rangée de droite). La densité de charge est calculée en utilisant la méthode SG 2D.

4.3. Récapitulation des informations obtenues par les techniques AFM

En conclusion, dans ce chapitre, les informations obtenues par les techniques AFM peuvent être divisées en deux parties: la première partie concerne les méthodologies qui ont été établies pour analyser les interfaces du point de vue mécanique et électrique; la deuxième partie concerne la connaissance et les questions ouvertes ont augmenté par les résultats obtenus.

Dans ce chapitre, afin d'étudier la physique des interfaces SC / LDPE, des sandwichs préparés en utilisant différentes couches protectrices, à savoir les couches de protection PI, Al et PET, ont été comparés. Dans le cas du PET et de l'Al, nous avons également comparé des sandwiches réalisés par les laboratoires ABB et Laplace. Tous les échantillons présentent le même contraste net de la force d'adhésion entre la matrice LDPE et les nanoparticules CB. Il a également été trouvé que les films de LDPE traités avec des couches de protection Al et PI présentent une rugosité d'interface supérieure à celle traitée avec du PET, conformément à nos conditions initiales de rugosité de surface établies avant le traitement en sandwich. Pour toutes les trois couches protectrices, l'absence de diffusion de CB du SC vers le LDPE est vérifiée.

La comparaison entre les cartes d'adhérence et de potentiel de surface montre que, même si l'interface physique est abrupte, le potentiel de surface décroît lentement de SC en LDPE. La variation de potentiel est de l'ordre de 15µm et présente une forme en cloche pour tous les types de couches protectrices. Cependant, nous pouvons remarquer que la plage de variation est plus importante pour la section réalisée en utilisant la couche de protection en PET. Cela peut être dû à des modifications de la chimie de surface (voir les résultats FTIR et PL dans la section 3.1) qui pourraient être non homogènes à la surface, induisant des différences entre les sections transversales provenant de différentes zones du même sandwich.

La densité de charge située à proximité de l'interface est plus élevée pour le LDPE traité avec PET qu'avec Al. Une densité de charge élevée dans le LDPE proche de l'interface pourrait être liée à la présence d'un groupe carbonyle dû à la couche de couverture en PET. Cependant, il existe une forte variation de la quantité et du signe de la charge dans le cas de la couche de recouvrement en PET selon les conditions du procédé. Il n'est pas clair si ce comportement est une conséquence de l'interaction du flux de matière de LDPE avec la surface de PET pendant le traitement.

Finalement, il a été trouvé que le profil de potentiel de surface est influencé par la polarisation latérale à travers l'électrode SC. Évidemment, de cette manière, le potentiel de surface initial est superposé au potentiel linéaire induit par la polarisation appliquée sur le SC. Ce champ électrique interne induit par l'application de la tension continue apparaît proportionnel à la tension appliquée et il n'y a pas d'évolution apparente de la distribution de charge initiale sous les champs modérés appliqués: cette charge apparaît donc relativement stable. La méthode présentée ici permet l'extraction de la densité de charge totale, c'est-à-dire des charges libres et de polarisation. Ainsi, des charges négatives sont sondées à proximité de l'anode et des charges positives proches de la cathode. Ces charges sont des charges de polarisation, ce qui confirme que notre méthode est sensible aux frais de libre et de polarisation. Comme perspective future de ce travail, l'application d'un champ électrique plus élevé pour injecter des charges dans le LDPE sera cruciale pour étudier à l'échelle locale l'injection de charge et pour comparer la densité de charge injectée déterminée par KPFM et PEA.

Conclusion et perspectives

Dans cette thèse, menée en collaboration avec ABB Corporate Research, les processus physiques se produisant à l'interface isolant/électrode ont été étudiés. L'objectif était de comprendre le les propriétés électriques à l'interface entre polyéthylène basse densité (PEBD) et l'électrode (ici nonmé semicon c'est-à-dire un polymère chargé de noir de carbone). L'accent a donc été mis sur les corrélations entre les propriétés de l'interface microscopique étudiées avec différentes techniques basées sur AFM, et le comportement électrique macroscopique, comme l'accumulation de charges spatiales et les courants de polarisation.

Dans une première étape, différents échantillons de LDPE ont été réalisés, en utilisant différentes couches protectrices lors de la fabrication, tels que PI, PET et Al, afin de déterminer si la couche de couverture a un impact sur les propriétés physiques de la surface finale du film LDPE (rugosité de surface, les propriétés chimiques due à la contamination de surface…). De plus, différents échantillons préparés par les laboratoires LAPLACE et ABB Corporate Research ont été étudiés.

Tout d'abord, pour voir si la couche protectrice utilisée dans le polyéthylène moulage par compression a un effet sur les propriétés chimiques, structurelles et électriques d'un échantillon LDPE, la photoluminescence (PL) et la spectroscopie infrarouge transformée de Fourier (FTIR), les mesures AFM et KPFM ont été utilisées. Les spectres PL et FTIR du LDPE traité avec du PET en tant que couche protectrice indiquaient clairement la contamination par le PET pendant le processus de moulage par compression. Plus précisément, cela peut être attribué à la diffusion de groupes oxydés, probablement des produits de décomposition ou des chaînes oligomères du PET dans la surface du LDPE. De plus, comme l'a révélé l'analyse de rugosité réalisée par AFM, des surfaces lisses sont obtenues en utilisant du PET. Cependant, dans le présent travail, aucune variation notable de la conductivité n'a été trouvée en relation avec les différents procédés de moulage par compression. Cette découverte dépend de l'ordre de grandeur du champ électrique utilisé pour évaluer la conductivité ainsi que des électrodes spécifiques déposées sur la surface du film.

Le chapitre 4 rend compte de la caractérisation physique et électrique de l'interface SC / LDPE. La méthode numérique pour calculer le champ électrique et la carte de densité de charge d'interface à partir des mesures de potentiel de surface est également décrite ici. La technique PF-QNM, exploitée pour réaliser la caractérisation physique, a permis de distinguer les nanoparticules CB encapsulées dans le SC au moyen du contraste de forces d'adhésion entre CB et SC. Ainsi, il a été possible de discerner qu'aucune inter-diffusion des nanoparticules de CB dans la couche de LDPE ne s'est produite pendant le processus de moulage. Pour l'ensemble des trois couches protectrices, l'absence de diffusion de CB du SC vers le LDPE et l'absence de vides ont été vérifiées. La technique PF-QNM représente une nouvelle approche pour l'étude de l'interface, permettant une meilleure résolution jusqu'à l'échelle nanométrique.

Afin de réaliser la caractérisation des propriétés électriques de l'interface SC / LDPE en terme de cartographie quantitative de la densité de charge d'espace, l'équation de Poisson a été appliquée à partir des mesures de potentiel de surface réalisées par la technique AM-KPFM. Fait important, cette

approche numérique permet de distinguer les frais de libre et de polarisation. De plus, après calcul des cartes de charges spatiales, il a été noté que la valeur maximale de la densité de charge à l'interface, évaluée par PF-KPFM, dépend du processus de fabrication, plus élevée dans le cas du PEBD traité au PET et décroissante pour les films LDPE traités à l'Al, qui pourraient être liés à la présence d'un groupe carbonyle dû à la couche de recouvrement en PET. Cependant, il existe une forte variation de la quantité et du signe de la charge dans le cas de la couche de recouvrement en PET selon les conditions du procédé. Il n'est pas clair si ce comportement est une conséquence de l'interaction du flux de matière de LDPE avec la surface de PET pendant le traitement. Ces résultats confirment que la forme en cloche du profil de potentiel de surface est due à des charges s'étendant sur plusieurs µm de l'interface. En appliquant une tension DC latérale à travers la structure SC / LDPE / SC, il a été mis en évidence que le champ électrique interne induit est proportionnel à la tension appliquée et il n'y a pas d'évolution apparente de la distribution initiale des charges sous les champs modérés appliqués.

Enfin, l'utilisation synergique de techniques basées sur AFM, telles que PF-QNM, AM-KPFM et PF-KPFM, a été démontrée ici pour représenter non seulement une nouvelle approche pour la caractérisation la plus complète et la plus complète des interfaces de matériaux isolants, mais, Plus important encore, pour constituer une méthode valable pour l'étude des phénomènes électriques à l'interface, tels que l'accumulation de charge et l'injection de l'espace, permettant la corrélation simultanée des propriétés électriques aux caractéristiques de l'interface physique, comme la rugosité. La dispersion dans les résultats des profils de potentiel de surface obtenus par KPFM dans le cas de LDPE traité avec une couche protectrice de PET sont suspectés d'être liés à la dispersion en quantité de contamination de surface.

Une perspective à ce travail devrait inclure la tâche difficile de mesurer le potentiel microscopique après l'injection de charge à des champs élevés. Cela permettrait de comparer la densité de charge injectée déterminée par la méthode KPFM et PEA de façon à la comparer et identifier les limitations de chacune. La réalisation d'un meilleur contrôle du processus de fabrication devrait également être abordée afin d'améliorer la reproductibilité des mesures de potentiel de surface. Enfin, la réalisation du contrôle d'injection de charge via l'adaptation des propriétés de l'interface LDPE / SC peut être abordée en exploitant la nouvelle approche proposée ici, offrant ainsi un moyen de contrôler l'injection dans les câbles d'alimentation et autres composants électriques.

General Introduction

The development of HVDC technology faces the problem of material design and optimization in a context where phenomena at play in dielectrics under DC stress are far from being under control. In principle, the switch from AC to DC technology may appear as a facilitating step regarding the reliability of insulations. First, it is generally recognized that the field strength under DC is higher than under AC. Hence, one may expect to obtain a better insulation, for a given geometry, under DC than under AC. One of the threats for AC insulations is the occurrence of partial discharges, at any place where the insulation is in contact with a gaseous medium and where the conditions for discharge inception are met. The discharge activity is, in normal service conditions at frequencies of the electrical network, 60 or 50Hz, grossly proportional to the frequency, i.e. a discharge event may be produced in every period of the AC stress. Under DC, this partial discharge (PD) activity is very substantially reduced; the frequency of occurrence being then controlled by the charge dissipation at the walls of the dielectric where the discharge is supposed to occur. So, it is the electrical conductivity of the insulating material that controls the frequency of occurrence. Low repetition rates of discharges are reported, -as slow 1 as per hour or so, except for corona phenomena occurring around a metallic piece. Therefore, damages due to discharges are substantially slowed down. Finally, electrical ageing, i.e. the slow degradation of materials under electrical stress is admittedly more effective under AC stress, owing to fatigue phenomena related to electromechanical stresses, and to the treeing processes that can develop preferentially from protrusions or defects and resulting from the alternative generation of positive and negative charges. Under DC stress some form of screening of the electric field by electrical charges can limit such process.

Though DC technologies may appear favorable for insulations, specific problematics are met. First, in HVDC systems, the power converters produce the intended DC voltage for transmission, but there may also be AC harmonics superimposed. The frequency of the AC harmonic can be in the kHz range. The superimposed harmonics on the HVDC may have synergistic effects on insulations, like the association of space charge build-up under the DC and the initiation of PD under AC, which would be triggered by the stored charges.

Under pure DC stress, an important issue is the control of the electric field. Contrary to AC stress, the electric field distribution under DC is essentially controlled by the electrical resistivity or conductivity. Contrary to dielectric permittivity, that varies moderately with temperature and hardly with electric field, the resistivity in dielectrics is substantially temperature and field dependent, in such a way that the actual field distribution is largely determined by operating conditions. In addition, space charge effects in dielectric materials may form, particularly at various types of interfaces (metal/dielectric, semiconducting screen/insulating materials, dielectric/dielectric) and render difficult to estimate the electric field distribution both in transient and steady state conditions. The prediction of the field distribution is, however, the most important prerequisite for designing insulation devices.

Progress in this field goes with systematic materials characterization through space charge or conductivity measurements as examples. This is expected to provide quantities related to bulk materials behavior in design-oriented models for DC. However, for properly accounting for processes at play at interfaces, boundary conditions must be settled. Such boundary conditions encompass for example charge exchange at metal/electrode interface, or possibly electrochemical processes resulting from ion drift from insulation bulk to the surface. Because in extra clean HVDC insulation the majority carriers are typically not intrinsic but injected, it is obvious that the conductance of insulation is strongly governed by the boundary conditions at electrode contacts.

The research work carried out in this thesis focuses on the experimental means to implement for complementing our current knowledge on these interface processes at electrodes. The main objectives are to settle appropriate methodologies for understanding the relation between electrode contact interface properties and the apparent electric conduction behavior. The intention is to find correlations between macroscopic interface properties and the macroscopic electric behavior. This would also help to make better models for the boundary conditions for the electric transport equations. This involves interface characterization methods, down to nanoscale, as well as physico-chemical and electrical measurements on materials provided with different interface conditions. The project resorts on fundamental research on polyethylene materials relevant to cables and cable accessories for the DC technology, and is readily applicable to other insulating materials and applications as capacitors for example.

This work was developed in the *Diélectriques Solides et Fiabilité* (DSF) research group of *Laboratoire Plasma et Conversion d'Energie* (LAPLACE), University of Toulouse III Paul Sabatier, Toulouse, France. This thesis was part of a collaboration with ABB Corporate Research Switzerland and Sweden and was financed by ABB.

The dissertation is divided into the following 5 parts:

Chapter 1: introduces the context of energy transport under HVDC and reviews the state of the art regarding physical phenomena and the interface of dielectrics as well as space charge processes in insulators. The physics of insulating polymers is reviewed considering the mechanisms of generation of charges insulation and the current description of interfaces based on band diagram and electronic energy levels at the metal/insulation contact. The space charge formation mechanisms, transport processes and charge trapping are described as 'bulk' materials properties. The last section of the chapter deals with the different scales at which interfaces can be viewed and modelled: from macroscale with Maxwell Wagner interface charges between two dielectric layers down to molecular and atomic scale approaches. The objectives of the thesis close the chapter.

Chapter 2: introduces the processing of materials and the experimental approaches. Polyethylene -PE and semicon/PE/semicon sandwiches are processed using press-molding technique using different protective layers (PET, Al…). These different layers were used to modify surface properties in terms of microstructure and roughness. The experimental methods and setups are presented, constituting 3 families of techniques, from chemical and structural characterization (FTIR,

Photoluminescence), macroscopic electrical characterization (space charge measurement by pulsed electroacoustic method, conductivity measurements), and nanoscale characterization, both with topological (AFM taping mode, Peak Force) and electrical modes (Kelvin Probe Force Microscopy).

Chapter 3: focuses on single layer characterization, with developing methodologies for characterizing the interface roughness. Results from photoluminescence and FTIR are compared for different protecting layers used in the processing of films. In the same way, the impact of the processing condition on the electrical response is investigated by transient current measurements and by space charge measurements.

Chapter 4: addresses nanoscale analyses of interfaces with focus on SC/PE/SC structures. Cross-sections of 3-layer structures were realized and analyzed by the different AFM modes available. The interface roughness is analyzed based on nanomechanical images of the cross-sections and the roughness of the interface is related to the process conditions. Potential maps obtained from KPFM are related to the surface potential of the electrode and to the contact charge setting up in the insulation. A methodology was developed to extract the charge distribution from the potential distribution.

General conclusion and perspectives: conclude the achievements of this work about the influence of the protecting layer used during the polyethylene press-molding and the morphological and electrical characterization of SC/LDPE interface. To finish anticipating the future works in this domain.

Chapter 1
State of the Art

1.1 Introduction

In the last century, as long as the worldwide population has been rising from about 1.6 billion at the begin of the century to 7.5 billion, the corresponding increase of the energy demand has pushed the research of renewable energy sources and, in parallel, has solicited the seek for new solutions to improve the efficiency of the electric network [WPP15].

The attempt of envisaging alternative energy sources to traditional fossil fuels, such as coal and oil, led to the development of hydroelectric, solar, wind and wave energy. While the traditional energy sources are transferred or stored as raw products close to consumption centres, the transport and storage methods of the electric energy produced by the renewable energy sources poses serious challenges. Petroleum, fuels or gas are commonly transferred via pipelines and transformed in thermoelectric power plants close to consumption centres, when demand is there. Conversely, renewable sources require energy to be firstly converted into electric power on site, and then transferred over long distances before reaching the point of consumption. Considering that a significant amount of energy is wasted during the transport and that the variability of the demand requests flexibility in the supply, smart grids need to be conceived and developed, by using a mix of technologies that adapt the structure to the demand of energy and lower the losses.

1.1.1 High voltage cables

The use of a high voltage (HV) leads to significantly more efficient transmission of energy. The power losses in a conductor are a product of the square of the current and the resistance of the conductor. This means that when transmitting a fixed power on a given conductor size, if the current is halved (i.e. the voltage is doubled), the power loss will be four times less. The power transmitted is equal to the product of the current and the voltage (assuming no phase difference). For this reason, to increase the power transmitted, maintaining the losses low, the voltage is the parameter to be maximized. The disadvantages to reach high voltages fall on the insulator reliability, and the design of higher voltage systems in general goes with new issues in the electrical insulation of systems. This is true for high voltage energy transport most concerned within this work, and for lower power and working voltages as with service voltage increase in aircrafts energy networks for example [Whee14] [Piet16].

The most common system used to deliver electricity from producers to consumers employs alternating current (AC). This system is widely diffused due to the lower cost of transformation from high to low voltage in the case of AC transmission [McNil11]. In a long AC cable transmission, the reactive power flow due to the large cable capacitance will limit the maximum possible transmission distance. However, nowadays the technological progress in (the integrated circuits) power electronics

is also progressively reducing the cost of the voltage conversion from low to high voltage for HV direct current (HVDC) systems. One of the methods to connect asynchronous AC systems, which operate at different voltage and/or frequency, is to interpose a DC link between them. Contrariwise to HVAC systems, HVDC is asynchronous and can be adapted to any rated voltage and frequency it receives. This permits to connect large AC systems in many parts of the world, otherwise incompatible. HVDC systems can also provide a precise power flow control of adapting the supply to the demand [Joh04]. HVDC systems are not affected by reactive power flow and there are no technical limits for the potential length of the cable. This permits to realize power transmission over very long distances with higher efficiency. In 2017 the longest HVDC cable is the NorNed link from south of Norway to Netherlands, under the North Sea [Sko10].

A large part of HV links is made with overhead lines. However, cable installation is also developing, as within urban areas, and mandatorily for submarine links. AC or DC high voltage coaxial cables usually share a similar structure. Both are schematically composed by five concentric layers: a metallic core conductor, an inner semicon layer, a polymer based insulation layer, an outer semicon layer and a metallic screening layer (Figure 1-1). Despite this similarity, the mechanisms that govern the electric field distribution are determined by different physical properties. Contrary to AC stress, where the permittivity plays the main role in the determination of the electric field distribution, under DC it is essentially controlled by the resistivity [Vu13]. Since the resistivity in insulating materials is substantially dependent on the temperature, the field distribution in DC cables exhibit more sensitivity to the temperature, hence on operating conditions, as compared to the AC cables [Vu15].

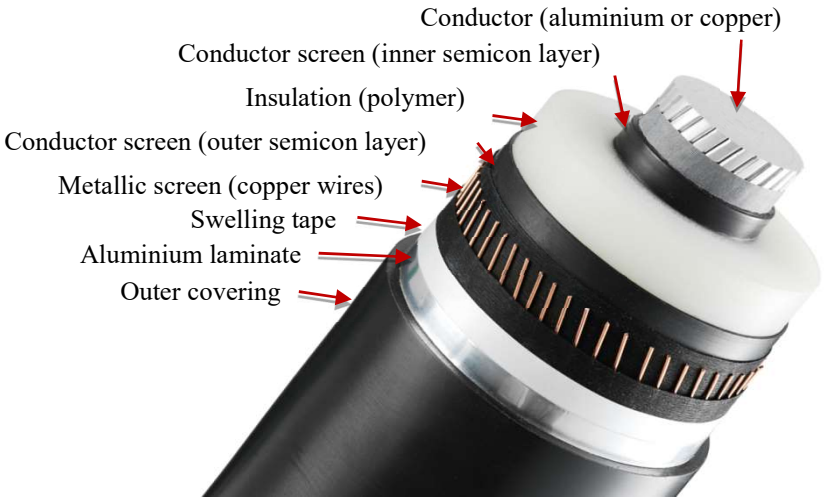

Figure 1-1 Internal layer in a high voltage coaxial cables.

The prediction of electric field distribution is the most important parameter for designing insulation devices like cables and cable accessories (e.g. joints and terminations) [Chr10]. Besides, electrical conductivity gradients, space charge effects may have substantial impact on the actual field distribution. These space charge features are related, on the one hand, to the behaviour of the bulk insulating material. On the other hand, change in charge generation processes occur depending on the contact behaviour and the interface type (metal/insulator, semicon/insulator, dielectric/insulator).

These features make it difficult to estimate the electric field distribution both in transient and steady state conditions [Chr15].

1.1.2 HVDC insulation

In the fabrication of HVDC cables, it is paramount to ensure a good insulation. The challenges to make a good insulation concern not only the reduction of the leakage current, but also the reliability of electric power link for decades. In this regard, cable manufacturing with synthetic insulating materials must satisfy high expectations, in order to provide advantages in terms of cost, operating temperature, the risk of pollution or maintenance in comparison to impregnated paper-based insulation [Han03]. Indeed, in the last decades, the progress in the fabrication of insulating materials for HV cable applications has fostered the evolution from oil-impregnated paper-based insulation towards polymeric insulation. The main reason of such a choice relies in the higher resistance offered by polymers with respect to oil-impregnated paper-based insulation, which improves the final performance of the cable in terms of electric losses. Although polymeric materials have been already employed as dielectric for the fabrication of HVAC cables, the application of polymers as insulating component in the HVDC cables is more recent. So far, polymers like XLPE (Cross-linked Polyethylene) have been successfully employed in highest rated voltage links of 420kV (Modalen-Mongstad, Norway 2017), leading to prospect new links of 640 kV and beyond. The excellent performances of the polymeric insulators have fuelled the race for world record in terms of voltage level, transmission capacity and distance, but the highest potential for HVDC links is still cables with paper-cables due to its lower space charge accumulation and the possibility to change polarity. The actual record for the highest potential, capability and length of HVDC links is held by the Changji-Guquan 1100 kV transmission link, in China, which transport a power of 12 GW across 3000 km.

The main issue in XLPE for insulating HVDC cables is related to cross-linking by-products or impurities which influence strongly the cable reliability [And06]. To improve reliability, physical properties of polymers need to be known. In the following section, polymer insulator properties and related physical phenomena are succinctly described. Thereafter, we will focus our attention on issues related to charge accumulation and transport in PE and on the influence of interfaces on these phenomena. As interfaces seem to have a substantial impact on charges in dielectrics, an overview of interface description is proposed from a macroscopic to an atomic point of view. To finish, my research strategy will be detailed.

1.2 Physical phenomena in polymeric insulators and interfaces

1.2.1 Insulating and semicon materials: a quick presentation

1.2.1.1 Properties of insulating polymers

The wide use of polymers as insulating materials is due not only to its electrical and mechanical properties, but also to its low production cost. Polymers define that category of materials characterized by the repetition, in long molecular chains, of chemical units called monomers. The

Greek origin of the name remarks its structure *poly-*, "many" + *-mer*, "parts". The monomers are linked together by strong covalent bounds, forming macromolecules, which in turn interact with each other via van der Waals forces. The final structure and its properties depend on the chemical compounds that constitute the monomers, its arrangement in the chain and the macromolecular organization in space. The engineering of these materials allows controlling mechanical and thermal properties, e.g. by varying the concentration of some additives. The additives usually incorporated into the insulation of cables to improve the operating properties of the polymers are:

- Crosslinking agents, which impart improved mechanical and thermal performances and connect the polymer chains by means of chemical bonds, forming a giant macromolecular network.
- Antioxidants, which are added during the polymers manufacturing to increase their resistance to oxidation.

During the manufacturing, the polymer forms its physical structure, which can be different depending on the setting conditions of the manufacture process: temperature, pressure, stretching [Yaha80]. The polymer chain arrangement is not uniform in all the materials: as an example, the atactic polystyrene is completely amorphous, while the polyethylene is semi-crystalline. The semi-crystalline arrangement is a mixture of two phases, one crystalline and the other one amorphous. The crystal phase exists in the form of lamellas, featuring intricate patterns inside the amorphous phase, these patterns being called spherulites (an example in Figure 1-2).

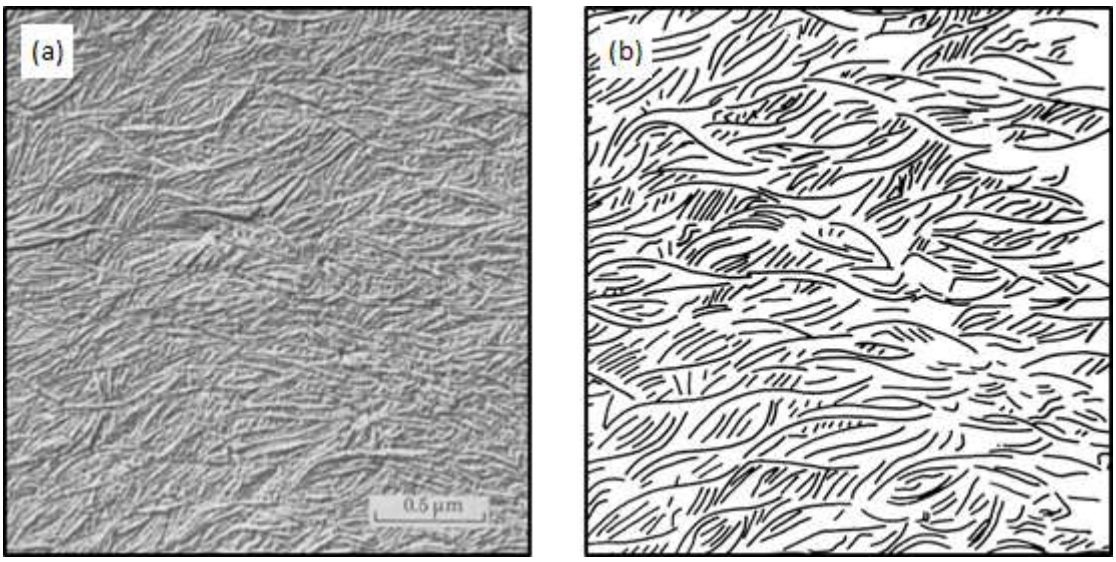

Figure 1-2 Etched cut surface of polyethylene using the electron microscope on the left, showing the lamellar organization of a banded spherulite traced on the right [Bass81]

One well known method to study the thermal transitions of polymers is Differential Scanning Calorimetry (DSC) [Pope76]. This technique permits to quantify the crystallinity degree and to identify the thermally induced phase transitions. The glass transition temperature and the melting temperature represent important parameters to use a polymer in the industrial domain, because these determine the upper temperature limit for many applications. The melting temperature (T_f) corresponds to the collapse of the crystals and the rearrangement of the macromolecules, inducing the loss of the degree of order. The phenomenon of crystallization, observed by cooling a polymer

previously heated above its melting point, occurs in correspondence of a specific temperature, defined as crystallization temperature T_c, at which the molecules rearrange to form crystalline zones. For example, during the rise in temperature the polyethylene shows an endothermic peak (about 110°C), corresponding to the melting temperature, and an exothermic peak (at about 90°C), observed while cooling, corresponding to the recrystallization.

1.2.1.2 Semicon role and properties

In HV cables the transition between the conducting metal and the polymeric insulator is never abrupt, but made of a semiconducting layer between the metal and the insulation, for at least two reasons:

- Firstly to reduce the mechanical stress between the two materials with different stiffness.
- Secondly to homogenize the electric field by smoothing the space around the wires of the central copper braid. Indeed, any protrusion on the conductor enhances locally the electric field and may trigger the development of electric trees into the insulation. So, homogenising the field and avoiding defects in a general way is of great importance for HV cables.

This semicon is usually a composite formed by carbon black (CB) dispersed in a polymeric matrix. The CB particles, denser than matrix reinforce the structure of the polymer improving the adhesion to the metal. The conductivity of this material is in the range of 10^{-5} S/m - 10 S/m. Many studies in the literature try to influence the properties of the semicon by varying the temperature, the electric field, the distribution or the size of nanofillers [Yi98] [Taw05]. Huang *et al.* [Huan17b] simulated the structure of interconnected nanoparticle clusters to determine the macroscopic behaviour thanks to finite element model including geometric information derived from real microscopic images (Figure 1-3).

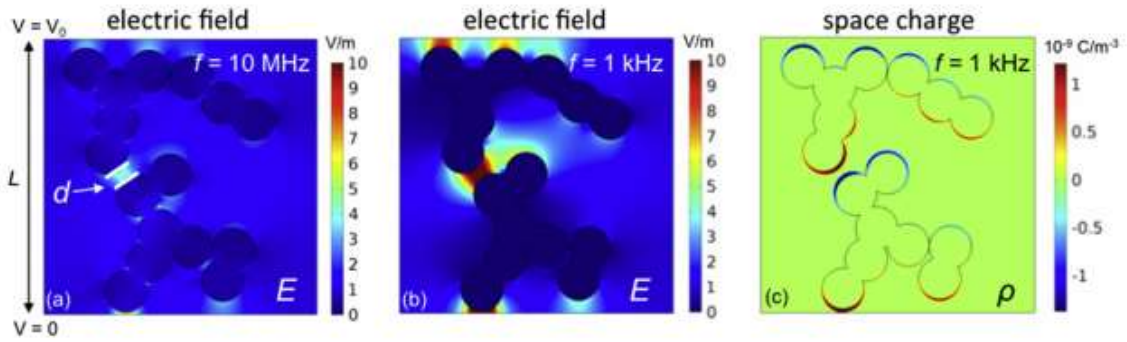

Figure 1-3 Field distribution in a 2D polymer composite containing conductive fillers that form two interconnected clusters, at a) 10MHz and b) 1kHz. In c): Plot of space charge distribution at 1 kHz. The results are obtained by solving the Maxwell's equations at an external field is 1 V/m [Huan17b].

1.2.2 Energy band diagram in polymeric insulators

In isolated atoms, the wave functions of bounded electrons have discrete energy levels. When the atoms join to form molecules or solid materials, their atomic orbitals overlap. Electrons have a fermionic nature and, to respect the Pauli's exclusion principle, they cannot share the same quantum numbers. The overlapped atomic orbital, therefore, splits into discrete molecular orbitals, which are very closely spaced in energy. Depending on the material bond structure and their symmetries, the electron states will be delocalized along multiple atomic sites or even throughout the entire material. As the number of electronic states involved increases, the atomic energy levels widen to form bands [Kitt05]. The electrons in thermodynamic equilibrium fill the bands following the Fermi–Dirac distribution, a probability distribution that considers Pauli's exclusion principle:

$$f(E) = \frac{1}{1 + \exp\left(\frac{E-\mu}{k_b T}\right)} \qquad 1\text{-}1$$

where E is the energy level of one electron in the distribution, μ is the total chemical potential of electrons or Fermi level (frequently denoted as E_F); k_bT, the product of the Boltzmann's constant and the temperature which represents the thermal energy available for the electrons.
The position of the Fermi level with respect to the band structure is decisive for electrical conduction, because only the electrons with energy nearby the Fermi level, using the thermal energy k_bT, are free to change their state with a neighbour unoccupied state.

Certain materials, exhibit forbidden interval between two energy bands, containing no energy levels, called energy band gap with size E_g. If the Fermi level falls within the band gap, there are no available states near the Fermi level to contribute to the electronic conduction. The three categories of materials depending on their electrical conductivity (metal, semiconductor and insulator) therefore depend on the availability of charge carriers:

- Metals, where the Fermi level is at the centre of a continuous band, are characterized by a high value of electrical conductivity (about 10^8 S/m).
- Semiconductors, where the Fermi level is within a small band gap, are characterized by a temperature-dependent electrical conductivity.
- Insulators, where the Fermi level is within a wide band gap larger than 3-4 eV, have very low conductivity (about 10^{-10} S/m).

In bulk materials, the highest occupied electronic energy level indicates the top of the valence band (E_v); the lowest unoccupied energy level, instead, defines the bottom of the conduction band (E_c). For organic molecules, the top of the valence band and the bottom of the conduction band are usually called, respectively, HOMO (Highest Occupied Molecular Orbital) and LUMO (Lowest Unoccupied Molecular Orbital) [Diss92]. When molecules or polymer chains form an organic solid, the electronic structure becomes like in Figure 1-4. The molecules interact each other by the weak Van der Waals forces. The HOMO-LUMO are usually localized in each molecule, reflecting the correspondence with the molecular state [Ishi99]. So, compared to inorganic semiconductors, the energy levels are much less delocalized.

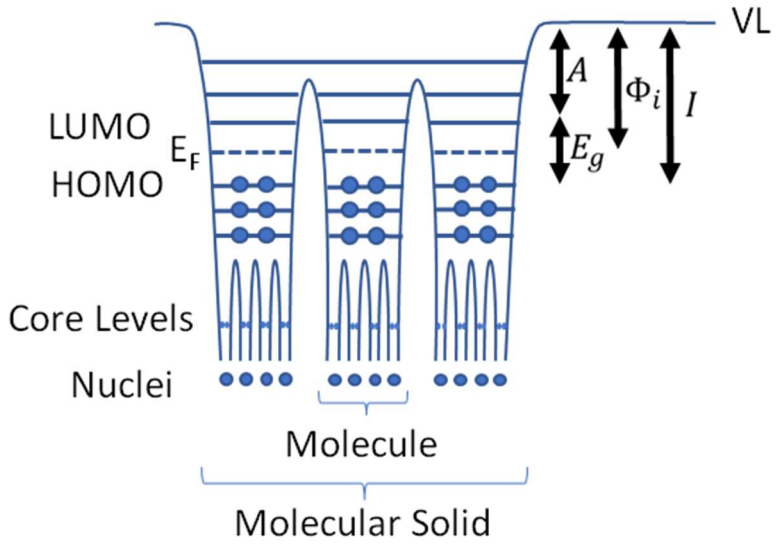

Figure 1-4 Electronic structure of a macromolecular solid. The highest level is the vacuum level to which the electron affinity (A), the working function (ϕ), and the ionization energy (I) are referenced. These correspond respectively to the LUMO, the Fermi energy level (EF) and the HOMO. At the lowest levels the electrons are more bonded to the individual atoms [Ishi99].

When two materials or two molecules are separated, their energy levels are not aligned, sharing only the vacuum energy level, VL. This corresponds to the potential energy of an electron at rest in vacuum or at infinite distance from the system. An electron with enough kinetic energy can reach the same energy which correspond to the VL also inside a material, but this kinetic energy can slightly change because of the presence of net charge. As shown in Figure 1-4, the electronic structure can be characterized by the band gap energy, E_g, described before, and other three parameters:

- A (Electron affinity): energy required to bring an electron from the bottom of the conduction band to the VL.
- ϕ (work function): minimum energy to bring an electron from the Fermi level of a material to the VL.
- I (ionization energy): energy required to bring an electron from the valence band to the VL.

The electronic and the optical properties of a material derive from its band structure. The difference between ionization energy and electron affinity corresponds to the bandgap energy, E_g.
As metals have no bandgap, then the ionization energy coincides with the electron affinity (I=A). Insulators have a wide band gap; therefore, I and A can differ by several eV. For example, the bandgap of polyethylene is estimated at about 8.8 eV [Hoff 91]. Promoting an electron from the valence to the conduction band in this case, using just the thermal energy (257 meV at room temperature) is nearly impossible. In these materials charge transport is in general believed to be due to defect states.

1.2.2.1 Metal/Insulating polymer contacts

When a metal and an insulating polymer, with different Fermi levels, are approached, a dipole layer may be formed right at the interface, due to various origins such as charge transfer across the interface, redistribution of the electron cloud, interfacial chemical reaction or other types of rearrangement of electronic charges. Such a double layer of electric charges forms an electrostatic field and then an electrical potential gradient that influences the VL near the material.

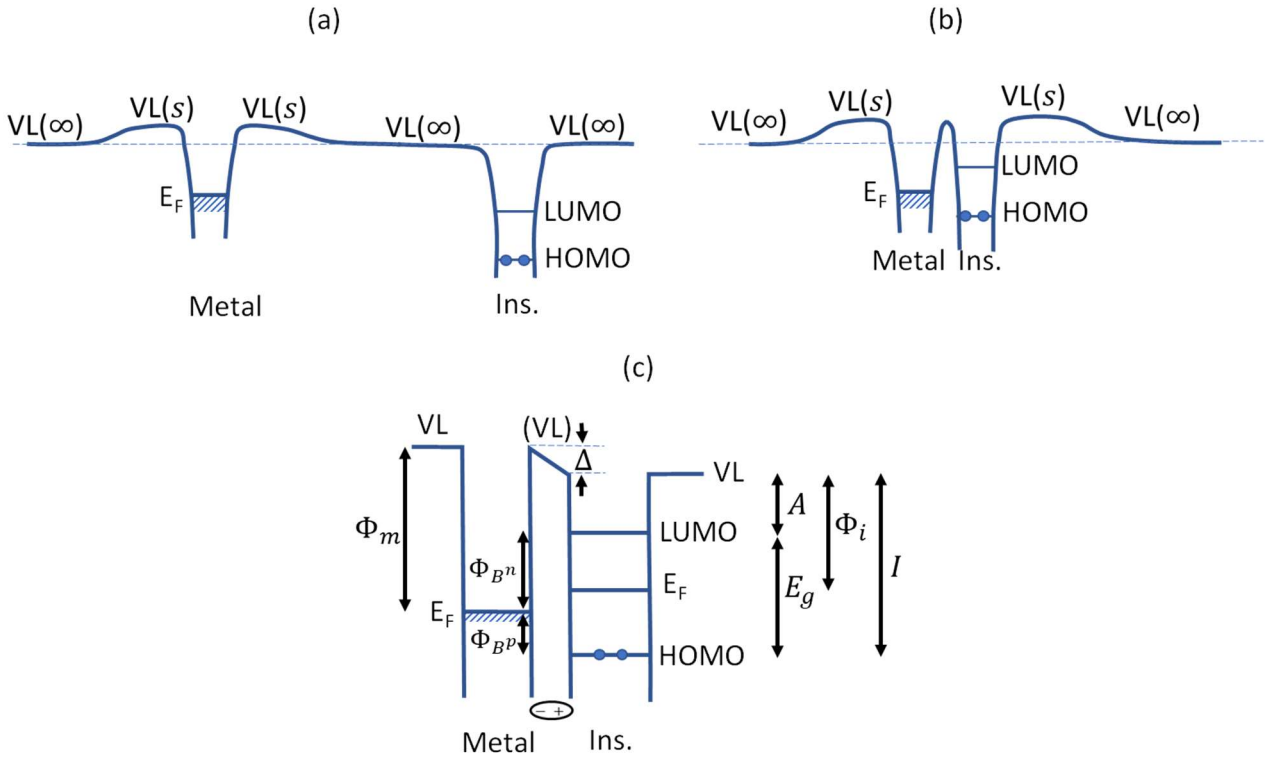

Figure 1-5 Electronic structure of a metal and an organic solid a) at infinite distance, levelled to the vacuum level (VL(∞)), and b) in contact, where the organic solid is within the surface dipole electric field of the metal. c) Interfacial energy diagram with a dipole layer formation. In this figure the organic side is charged positive, reducing the energy barrier for electrons [Ishi99].

As shown in Figure 1-5, when the solids are very close without rearrangement of the electric charge, the insulating layer is affected by the potential of the metal surface dipole. Its energy levels rise to have a common local VL in an extremely narrow interfacial gap. To reach the electrical equilibrium, the Fermi levels must be at the same energy in both materials. When the available mobile carrier density in the insulating layer is sufficiently large, the charges redistribute around the interface in a short time. The potential distribution at the interfacial region is governed by the Poisson's equation, which correlates the charge to the potential. Because of this, a diffusion layer forms a band bending that aligns the Fermi energies of the two solids, with a built-in potential V_{bi} in the insulating layer (Figure 1-6). The thickness of the diffusion layer W is related to the potential V_{bi} of the insulator and the spatial distribution of available trap levels [Sze81].

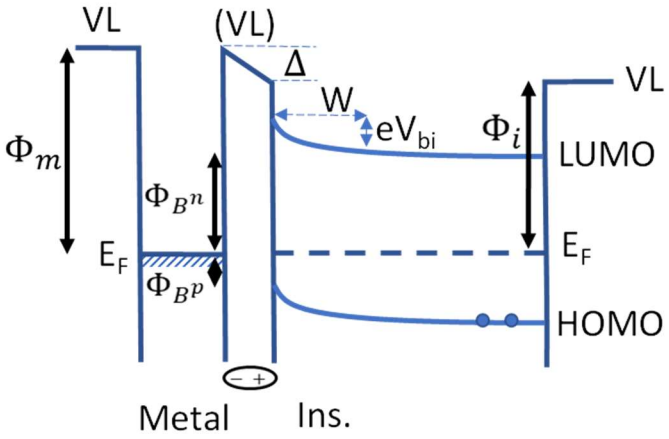

Figure 1-6 Interfacial energy diagram with band bending. The charge distribution in the organic layer achieves the equilibrium bending of the energy levels [Ishi99].

1.2.2.2 Electronic traps in the insulator

In the forbidden band, in theory, no state of energy is available. There are structural defects in polymers due, for example, to the presence of impurities: additives, crosslinking agents or antioxidants. These structural defects introduce intermediate energy states in the forbidden band, which can trap charges in the polymer. These energy states are considered as hole traps when they are above the valence band, and electron traps when they are just below the conduction band. Measurements of thermostimulated currents (TSC) or of thermostimulated luminescence (TL) make it possible to approximate the nature and depth of traps in polymer insulator as polyethylene [Ieda84].

Traps can be deep or shallow depending on their origin. Deep traps are generally due to chemical defects (crosslinking agents, antioxidants, additives, etc.) and the shallow traps are due to physical disorder. The traps are distributed in the band gap according to the morphology of the insulator. For example, Chowdry et al. considered a discrete trap distribution for crystalline materials and a continuous distribution for amorphous materials [Chow74].

1.2.2.3 Electronic surface states in organic polymers

The concept of surface states was introduced theoretically in 1933 [Tamm33] and proved experimentally in 1947 [Bard47] showing that the potential barrier between a silicon or germanium crystal and a metal, is weakly dependent from the metal work function and the conductivity of the semiconductor. Shockley et al [Shock48] experimentally observed the existence of surface states on semiconductor thin films measuring the conductance between the two gold electrodes evaporated on both ends of the semiconductor, permitted to determine the capacitance of the surface region of P-type germanium and N-type silicon.

As discussed before, the barrier height for a metal/insulating contact without surface states is $\Phi_m - A$ (see Figure 1-5). In presence of surface states, the barrier height is no longer dependent from the work function of the metal. The electrons of the metal acquire low energy and can move by jumping through the energy levels located in the insulator band gap. Before the contact, the surface states are

filled up to a level Φ_s from the conduction band. Upon the contact, if the work function of the metal (ϕ_m) electrode is lower than that of the insulator (ϕ_i), the electrons from the metal will fill the empty surface states. The electrons transferred from the metal to the surface states modify the value of the potential energy at Φ_{s1}.

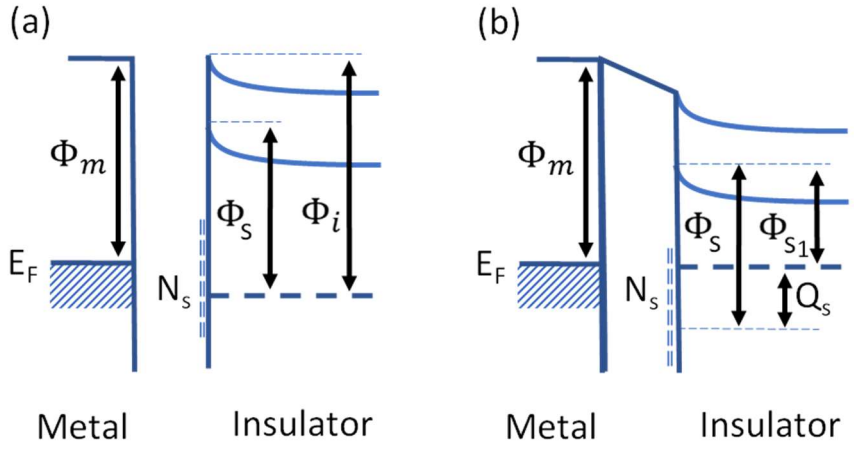

Figure 1-7 Energy levels of a metal and an insulator with surface states (a) before and (b) after the contact.

The charge transferred per unit area is thus written as follows [Mizu76], [Shock48]:

$$Q_s = eN_s(\phi_{s1} - \phi_s) \qquad 1\text{-}2$$

where e is the elementary charge and $N_s[m^{-2}eV^{-1}]$ is the density of surface states.
The presence of surface states changes the potential across the contact which in this case becomes:

$$\Delta V = \frac{1}{e}(\phi_i - \phi_m) - \frac{1}{e}(\phi_s - \phi_{s1}) \qquad 1\text{-}3$$

The capacitance created by the charges to the surface states is written in the form:

$$C_s = \frac{Q_s}{\Delta V} = \frac{eN_s(\phi_{s1} - \phi_s)}{(\phi_i - \phi_m) - (\phi_s - \phi_{s1})} = \frac{\varepsilon_0 \varepsilon_r}{d} \qquad 1\text{-}4$$

Where Cs is the capacity per unit area, d is the thickness of the region containing the surface states and ε_0 and ε_r are, respectively, the vacuum and the relative insulator permittivity.

From equation *1-4*, the surface states density N_s in the forbidden band can be estimated by the formula [Mizu76]:

$$N_s = \frac{\varepsilon_0 \varepsilon_r}{ed}\left[\frac{|\phi_m - \phi_i|}{(\varphi_{s1} - \varphi_s)} - 1\right] \qquad 1\text{-}5$$

In equation 1-5, the estimation of d is the most challenging. It can range from few nanometres to a few micrometres depending on the material. Currently, we cannot determine this distance with

experimental measurements due to lack of resolution. Similarly, finding the levels of surface state filling before and after the contact is not straightforward.

The identification of electronic surface states in organic polymers is complex as many candidate defects are present; hence the full understanding of the mechanisms that govern their behaviour is not at reach. A possible source of surface states is from physical and chemical defects. These create deep or shallow traps in the forbidden band of the dielectric. The interfaces are preferential regions for the accumulation of these defects. An example of the chemical compound usually present in cable insulation is the antioxidant or, in absence of this, functional groups bounded on the polymer chain, characteristic of oxidation.

On the other hand, for metal/organic (dielectric or semiconductor) interfaces, it has been shown that a reaction between the metal and the polymer can take place and lead to the formation of metal oxide in contact with the organic material. The potential difference is therefore no longer that of the pure metal, but that of a metal oxide, that can differ by more than 1 eV as a function of the metal considered [Grob07].

However, few data are available about the impact of these interface states on the charge generation in the material. Some authors consider that the surface states act as a springboard to assist the charge injection from metal to the organic material [Thie96], [Mizu86], [Hoan10]. Others, contrariwise, consider these states close to the metal contact to behave as charge deep traps [Kao 81].

1.2.3 Conduction in insulation material

As in any other material, the conduction in insulation material corresponds to the motion of electrical charges. Understanding conduction processes resorts to the identification of the nature of carriers present or generated in the materials under the effect of an external field and of the processes whereby they move.
Electric charges present in the insulator, can be formed by different mechanisms as depicted in Figure 1-8. The processes are distinguished here according to the position of their source:

- Volume charge generation: polarization (dipole creation) (a), intrinsic or extrinsic ionic carriers (b), electro-dissociation of neutral species (donor, acceptors) (c).
- Interfaces charges generation: injection of holes at the anode (d) and of electrons at the cathode (e), surface states (f), chemical reactions (ion production) (g).

The carriers differentiate depending on their origin: intrinsic if they are generated inside the material or extrinsic if they come from outside. All charges can move in the insulator. The displacement of the charges may result in their accumulation in some parts of the material, breaking charge neutrality and leading, in virtue of the Poisson's equation, to local change of electric field. Damages in materials or equipment can appear as a consequence of such charge accumulation if the local field exceeds some limits.

The physical mechanisms that apply to the transport of charges are widely studied and used to interpret experimental results. But the detailed physical phenomenon at play in a particular situation is often not easy unravelling. In an insulating material, two types of charge carriers are involved in

the establishment of a current: electronic charges, which include electrons and holes, and ions. These two types of carriers are differentiated according to their origin.

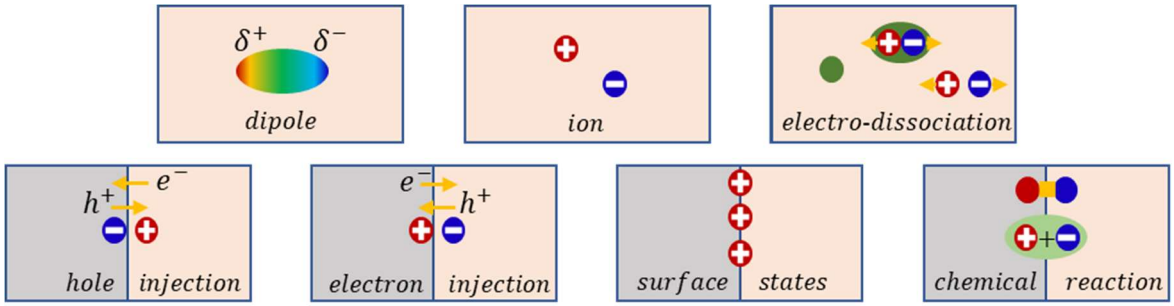

Figure 1-8 Summary diagram of the different mechanism of charge generation: a) polarization, b) ionic carriers, c) electro-dissociation of neutral species, d) holes injection, e) electron injection, f) charge generation in surface states, g) chemical reaction.

1.2.3.1 **Transport**

It is difficult to list all the ions contained in a polymer matrix or to know their origin. However, several tracks seem to converge towards the same ion generation mechanisms.

Ions, chemical residual by-products of the polymerization, exist in an insulator since its synthesis. They may come from chemical reactions, such as sulfuric group present in antioxidants or organic ions (oxalate) resulting from the oxidation of the polymer [Gilb89]. The moisture also seems to be an important factor, since the water molecules contained in the insulation influence charges transport and appear to interfere in the ionization of impurities [Aida97].

On the other hand, the application of a voltage disturbs the electronic arrangement of molecules such as salts or neutral molecules. A lesser known generation mechanism occurs by diffusion of certain ions from the electrodes to the insulator. These ions can have a metallic or organic origin. This is of specific relevance for the present work since ions generation was reported for semicon/insulator interface [Take99, Ho01].

When an electric field is applied, the neutrality of the matrix is disturbed, and the ions move in the direction of the electrodes. It is essential for describing ion transport to take account of the mass and size of these ions in comparison with that of electrons and holes. The mobility of these ions is thus much lower than the electronic mobility. It is difficult to know exactly the nature of the ions involved in conduction, especially when the material of study is complex. These ions can be trapped into potential wells created by the polymer chain conformation. If they acquire sufficient energy to leave a well, they can move along the carbon skeleton to be displaced in another potential well. The chain architecture is therefore at the origin of these potential wells. The current density resulting from the ionic conduction is [Diss92] [Mott48]:

$$j_{ion} \approx \frac{e^2 E a^2 \nu_0 N}{k_b T} exp\left(-\frac{E_a + \Delta G}{k_b T}\right) \qquad 1\text{-}6$$

where e is the electron charge, E the electric field, a is the average distance between two ionic sites of concentration N and activation energy E_a, ΔG is the Gibbs free energy and ν_0 is known as the attempt to escape frequency. The activation energy is a barrier energy that an ion thermally must overcome be displaced to the next site. The Gibbs free energy corresponds to a quantitative measure of the favourability for the ion to bind in a site using the thermal energy after passing the barrier. This energy can be either positive or negative, in case this process is thermodynamically favoured or not.

1.2.3.2 Electronic charge generation

The intrinsic generation of electronic charges is poorly known, however, some generation mechanisms seem to be favoured, such as:

- the dissociation due to natural radiation (cosmic [Coel93], radioactivity, UV) or thermal activation.
- charge injection from interfaces. Numerous studies [Fowl28] [O'Dw73] [Lamp70] carried out on this subject made it possible to understand in part these processes controlled by the interfaces, and in particular for interfaces of metal-insulator contacts.

In the following, we will discuss only the charge generation mechanisms which involve interfaces.

The barrier height ϕ_b separating the Fermi level of the metal and the conduction band of the insulator is a function of the limit conditions at the metal-insulator interfaces. It differs from the metal work function by the electronic affinity of the insulator. This energy is the minimum energy that a charge must acquire to escape from the Femi energy of the metal and cross the barrier.

The two most discussed mechanisms in the literature are the Schottky and the Fowler-Nordheim mechanism.

a. Schottky mechanism

The generation of charges in the insulator by the Schottky effect is also called thermionic effect. It takes into account the electrostatic attraction of an electron with a metal. When a charge is at a distance x from the interface of an insulator with permittivity $\varepsilon = \varepsilon_0 \varepsilon_r$, is attracted by its image charge on the metal. The application of an electric field decreases the potential energy U, whose expression becomes (Figure 1-9):

$$U = -exE - \frac{e^2}{4\pi\varepsilon x} \qquad \textit{1-7}$$

This leads to a reduction in the barrier height, as shown in Figure 1-9c, equal to:

$$\Delta\phi_b = \left(\frac{e^3 E}{4\pi\varepsilon}\right)^{\frac{1}{2}} \qquad \textit{1-8}$$

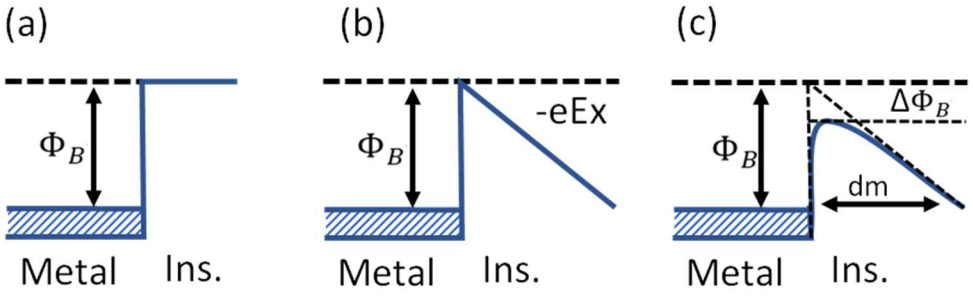

Figure 1-9 Potential energy diagram for a metal-insulating interface: a) in the absence of an electric field; B) when applying an electric field; (C) considering to the influence of the charge.

The injection current density $j_{Schottky}$, which considers of the potential barrier reduction is described by [Diss92] [O'Dw73]:

$$j_{Schottky} = AT^2 exp\left(-\frac{\phi_b}{k_B T}\right) exp\left(\frac{e}{k_B T}\sqrt{\frac{eE}{4\pi\varepsilon}}\right) \qquad 1\text{-}9$$

where A is a constant, T the temperature and E the electric field. The first exponential product represents the thermal emission, while the second determines the dependence of the electric field. It should be noted that when the electric field is zero, the current density is not zero, but simply results from the thermal effect. This current represents the injection saturation current. In equilibrium it is compensated by a backward current which forms due to charge accumulation into the insulator [Chr15].

b. Fowler-Nordheim

The injection by the influence of the electric field enhanced tunneling, also called Fowler-Nordheim effect [Fowl28] is related to the quantum theory. An electron from the electronic layer of the metal has a non-zero probability to being at a given moment on the other side of the potential barrier. This non-zero probability allows some electrons with energy lower than the barrier height to pass through. The phenomenon is intimately related to the particle wave function, which decreases rapidly with increasing distance. Fowler-Nordheim type injection becomes significant only for very high fields (1GV/m) and the band distortion makes the thickness of the potential barrier (dm) very thin.

$$j_{F-N} = \frac{e^3 E^2}{8\pi h \phi_b} exp\left[-\frac{4}{3}\left(\frac{2m}{\hbar^2}\right)^{\frac{1}{2}} \frac{\phi_b^{\frac{3}{2}}}{eE}\right] \qquad 1\text{-}10$$

with e and m respectively the electron charge and mass, E the electric field, ϕ_b the barrier height

The Fowler-Nordheim current is dependent mainly on the electric field. However, further studies have shown [Diss92] that the tunnel effect was also enhanced by temperature. Thus, by increasing the temperature, electrons in an excited state in the metal have a greater probability of passing through the barrier by tunnelling and to reach the conduction band of the insulator.

1.2.3.3 Transport mechanisms for electronic carriers

Different mechanisms are proposed to describe charge transport in insulating materials for example the Ohmic regime, Space Charge Limited Current (SCLC), hopping current, and the Poole-Frenkel mechanism.

a. Ohmic current

The conduction mechanisms result from charge carrier movement under an applied electric field. An ohmic current is characterized by a linear behaviour with the applied voltage and the intrinsic carrier density n_0. Considering a material of size L with charges mobility μ, the current density result from the movement of these free charges at the velocity ν, is governed by the Ohm's law:

$$j_{Ohm} = \nu e n_0 = e n_0 \mu \frac{V}{L} \qquad 1\text{-}11$$

In the ideal case of a trap-free insulator the number of intrinsic carriers that contribute to the conduction is negligible. The transport of injected carriers from an electrode can also be described as a linear (ohmic) contact when the injected charges do not modify the internal field and the diffusion is neglected [Lamp70]. The equation 1-11 remains valid at low voltages as shown in the first step current density graph in Figure 1-10.

b. Space Charge Limited Current

When the injection current increases with applied voltage, the injected charge density increases and controls the local field. By solving the system of equations consisting of the Poisson's equation, the equation of continuity and the relation that links the field to the voltage, the Space Charge Limited Current (SCLC) density is determined [Diss92]:

$$j_{SCLC} = \frac{9}{8} \frac{\varepsilon \mu V^2}{L^3} \qquad 1\text{-}12$$

For an ideal insulator without traps, the current density results from the combination of conduction and SCLC mechanism. Moreover, the threshold voltage V_{tr} between the phase dominated by the ohmic current and the SCLC is expressed by:

$$V_{tr} = \frac{8}{9} \frac{e n_0 L^2}{\varepsilon} \qquad 1\text{-}13$$

This value can be extrapolated from the current-voltage graph, known the intrinsic carrier density n_0, the sample size L and its permittivity ε, it is possible to estimate the density of charge in the insulator.

Consider now an imperfect insulator, in which a level of traps is present. The traps imply the creation of new species of charges, trapped charges with density n_t. It is therefore necessary to introduce a

coefficient which represents the proportion between the free charges and the trapped charges: $\theta = \frac{n_c}{n_t}$. The Equations (1-12) and (1-13) then become:

$$j_{SCLC} = \theta \frac{9}{8} \frac{\varepsilon \mu V^2}{L^3} \quad 1\text{-}14$$

$$V_{tr} = \frac{1}{\theta} \frac{8}{9} \frac{n_0 \mu L^2}{\varepsilon} \quad 1\text{-}15$$

This corresponds to the second slope in Figure 1-10. The coefficient θ may be very low (i.e. there are a large number of traps), and the number of charges available for transport is very low. Then the transition voltage from the ohmic behaviour to the space-limited behaviour would be very large.

A regime change occurs for a voltage V_{TFL} corresponding to the Trap Filled Limit (TFL). The conduction increases abruptly when the θ value increases to unity. Afterwards, all the injected charges can move because there are no free traps available. This mechanism corresponds to the fourth slope in Figure 1-10.

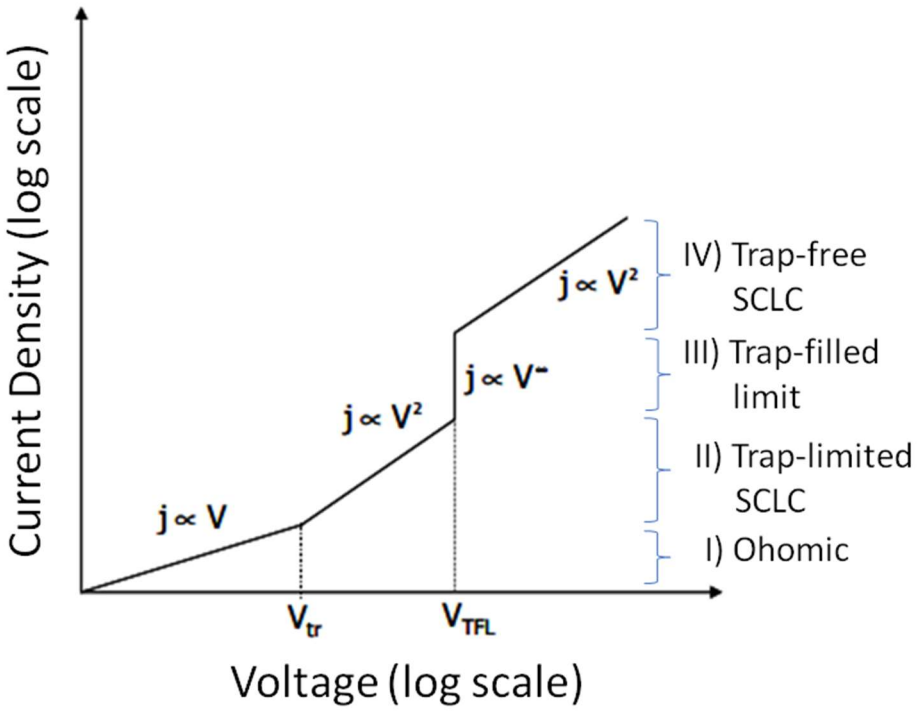

Figure 1-10 Characteristic space charge limited current density depending on the voltage, assuming a single trap level.

c. Hopping current

Insulating polymers show a distribution of traps between the valence and conduction bands, giving rise respectively to hole and electron traps. The charge carriers, injected into the dielectric by the Schottky or the Fowler-Nordheim mechanisms, have energy close to the Fermi level. The transport of these charges cannot be easily done unless their energy level is close to the conduction or the valence band, however when the distance is small enough, the charge can jump from site to site assisted by the thermal energy and the electric field. The deeper traps behave like potential wells, in

which the charges are attracted and remain for a time, dependent on the trap energy level. The factors which contribute to the probability that the hopping process occur are:

- the contribution of the phonon spectrum ν_{ph};
- the Boltzmann factor $exp(-w/k_bT)$ between the two states with energy difference w;
- the overlap factor $exp(-2\alpha R)$ of the wavefunction considering a jumping distance R and α^{-1} the attenuation length.

The last two terms represent the mechanism of variable range hopping. Moreover, considering the trap density $n(E_f)$ within a range of k_bT of the Fermi energy, the expression of the current density for the hopping must then take into account the difference of hopping probabilities in the two directions (thermal hopping) expressed by the exponential term

$$exp\left(\pm\frac{eRE}{k_bT}\right). \qquad 1\text{-}16$$

These quantities represent the probability of movement in the direction of the electric field E or in the opposite direction, related to different values of the potential barriers. The general expression of the hopping current takes the following form [Mott71]:

$$j_{hop} = 2ek_bTn(E_f)\, R\, \nu_{ph} exp\left(-2\alpha R - \frac{w}{k_bT}\right) sinh\left(\frac{eRE}{2k_bT}\right) \qquad 1\text{-}17$$

The mobility for hopping conduction is usually lower than that obtained for a space charge limited current, since the charges spend the majority of time on traps rather than participate to the transport.

d. Poole-Frenkel mechanism

The Poole-Frenkel mechanism in the volume is the analogue of the Schottky injection at the metal-insulating interface. This mechanism takes into account the possible trapping and detrapping of the charge carriers by thermal activation. Unlike the Schottky phenomenon, where the injection barrier is decreased by the charge present in the insulator, the Poole-Frenkel mechanism is based on the potential barrier height reduction due to the application of an electric field. The expression of the current density resulting from this phenomenon can be written according to [O'dw73]:

$$j_{P-F} = j_0 exp\left(-\frac{\phi}{2k_BT}\right) exp\left(\frac{e}{k_BT}\sqrt{\frac{eE}{4\pi\varepsilon}}\right) \qquad 1\text{-}18$$

where ϕ is the height of the barrier and j_0 is an empirical proportionality factor.

1.3 Space charge in polymer insulation: from bulk to interface

1.3.1 Main issue in bulk insulator

The accumulation of space charge is a phenomenon to which insulating materials are subjected under electrical, mechanical (friction) or irradiation stresses for example. It is a consequence of combining charge sources and the low mobility of carriers in the material. This phenomenon is a critical factor for the behaviour of insulators, impacting among other things the high field withstanding of insulators, and being at the origin of hazardous phenomena as flashover processes and electrostatic discharges. The role of space charges in aging of insulators has been the subject of studies for more than seventy years [Von37] [Diss92] [Diss95].

Charges can be generated in insulations through a variety of processes as depicted in Figure 1-11. The term "space charge" in general stands for the presence of an excess of charges within the dielectric, breaking the neutrality rule. The localisation of the excess charge into the dielectric depends on its origin. The SCLC conduction process for example results from an unbalance between the generation of charges and their transport. When the injection of charges at the electrode cannot be equilibrated by their drift in the dielectric, homocharge, i.e. charge of the same sign as the polarity of the electrode is formed. Consequently, the field at the electrode is lowered and in the bulk ahead of the space charge region it is enhanced. Heterocharges, i.e. charges of opposite sign compared to the polarity of electrodes are formed for example in presence of ion motions or for electronic carriers with partially blocking electrodes. Then the field at the electrode is enhanced and in the bulk it is lowered. Figure 1-11 depicts some cases of charge and field distribution.

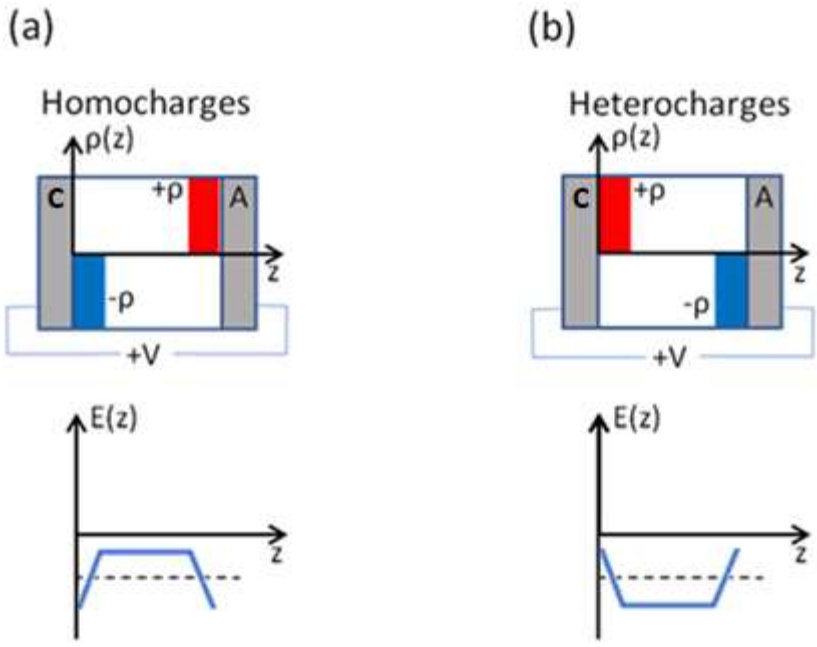

Figure 1-11 Schematics of homocharge build up (a) and heterocharge build-up (b) inducing distortion in the electric field.

Besides these cases of unbalance between charge source and their transport, deep trapping, i.e. stabilization of charges for long times on specific centres is a further process that leads to charge accumulation in the bulk of materials.

Charge accumulation in polymeric insulators still represents the main issue and is due to uncontrolled processes, like ionic phenomena with large field enhancement. The presence of cross-linking by-products leads to space charge formed by internal dissociation. In high quality electrical insulation, the presence of these contaminants is refrained by improving physical and chemical cleanliness of materials. For application to HVDC, space charge formation has to be avoided and current grade of crosslinked polyethylene materials dedicated to HVDC impart substantial space charge reduction compared to grades for HVAC. The understanding of electrical conduction mechanisms in polymer insulation is crucial for this application, particularly for the prediction and control of the field distribution.

In this work we focus on space charge due to injection from contact interfaces.

1.3.2 Why to study interfaces?

The great progress in the techniques used to probe space charge distribution in the bulk of dielectric materials has led to the possibility of following the charge build-up with a spatial resolution of 10 µm and time resolution of the order of microsecond [Teys17]. Investigation aimed to tailor bulk properties in order to reduce the space charge accumulation.

Simulations of molecular electronic levels in the polyethylene structure allow to estimate the trap depths introduced by chemical impurities and suggest how these influence with a proper doping the polymers [Meun01] [Huza10] [Teys09] or the use of nanocomposite materials [Nels14] [Ples16]. The technique has been extended recently to approach ionic transport in polymers [Huan17a]. It has been observed that charge build up [Taleb13] [Chen04] and even conductivity measurements [Ghor16a] depend on the interface electrode/insulator conditions and not only on bulk properties. Efforts focused on the possibility to reduce space charge accumulation by controlling the purity of the material and the roughness at the interface. Further tailoring the interface was proposed through processes as oxyfluorination [An09] or by depositing metallic nanoparticles that can act as deep traps at the surface and produce a decrease of the field at the interface [Mill16].

Ghorbani et al. found that pressing an LDPE sample with PET film influenced the conduction and dielectric losses. This effect may be due to diffusion of chemical species from the PET film into the samples during the press moulding or the heat treatment of the film [Ghor16a]. The interface which impacts strongly bulk properties and macroscopic behaviour need to be characterized and investigated accurately.

The above points on the sensibility of material response to the interface properties, an as a consequence, to potentialities open by a fine control of interface for further improving the reliability of insulations. The interests in investigating electrode/insulating polymer interfaces can be more broadly justified from three standpoints:

- insulations appear as wide bandgap materials and, according to semiconductor physics, an extremely small theoretical probability of having intrinsic carrier provision: the only possibility to provide carriers is by means of injection processes;
- the need to improve our knowledge on essential mechanisms controlling charge exchange processes at interface, resorting to the roughness, the chemical functionalization, or the nature of electrode, for optimising the design or tailoring of the interface toward charge injection mitigation for example;
- found the way to justify the hypotheses to be adopted on the boundary conditions for some critical cases e.g. macroscopic transport models based on conductivity and permittivity data or drift-diffusion processes, taking into account the density of carriers, the nature of the material and its mobility.

1.4 Properties of interfaces

1.4.1 Interface description

The interface represents the boundary between two spatial regions occupied by different materials, or by matter in different physical states. A characteristic of heterogeneous two-phase systems is that to reach the equilibrium usually involve charges. The properties of bulk materials around the interface are always affected by the transition from one phase to the other. As shown in Figure 1-12, the contrast between representative properties, ρ_1 and ρ_2, allows defining the interface limits [Lewi94].

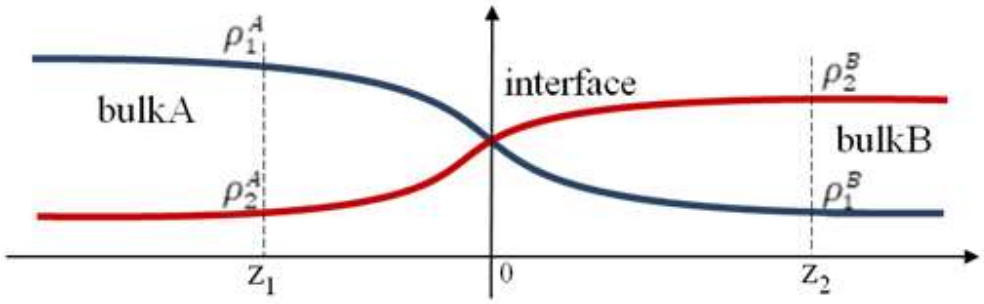

Figure 1-12: Example of interface (z2-z1) between the phases A and B, defined by the properties ρ1 and ρ2 [Lewi94].

According to the scale in which the phenomena occur, the interface can be reasonably modelled as a two or three-dimensional boundary condition, depending on the volume involved. If the volume of the transition region becomes important with respect to the bulk phase and the properties of this area differ greatly from the bulk properties, it is called “interphase” [Rät10].

Accurate description of interface behaviour is complex because many phenomena can take place simultaneously and at different scales. For example the scales may be extend from sub-atomic distances, for the electron cloud displacement in a metal, to several nanometres, for ions in an electrolyte, or tens of micrometres, for the space charge accumulation into an insulator. The following sub-section will show some characteristic phenomena that involve the volume around the semicon/insulator interface at different scales, and will describe interfaces at different scales to highlight known properties and phenomena which remain unclear.

1.4.1.1 Macroscale

HV cables present many layers of different materials and the first challenge is that the interfaces in between two layers extended along the entire length of the cable. This means that uniform conditions must be guaranteed over hundreds of metres to avoid the formation of weak points. The stress distributed across long distances may become difficult to be sustained by a weak point which compromises the entire system. Another interface that extends over long distances is that formed in joints terminations or accessory interface. Although the exploitation of these latter may greatly improve both reliability and performance of the HV cables, they can also induce problems related to unwanted interfaces due to manufacturing or aging, hence worsening the breakdown strength.

At macroscopic scale a model that describes reasonably well the charge accumulation across the interface is the Maxwell-Wagner-Sillars (MWS) model. It defines the interface charge density that settles at the interface between two dielectric layers of different permittivities and/or conductivities. Given the values of the permittivity (ε_1,ε_2) and conductivity (σ_1,σ_2) at both sides of the interface, the interfacial charge $\Sigma_s$can be estimated for an applied potential V as [Mors13]:

$$\Sigma_s(t) = \frac{\varepsilon_1\sigma_2(t) - \varepsilon_2\sigma_1(t)}{d_1\sigma_2(t) + d_2\sigma_1(t)} V\left(1 - e^{-t/\tau_{MW}(t)}\right) \qquad 1\text{-}19$$

with:

$$\tau_{MW}(t) = \frac{\varepsilon_1 d_2 + \varepsilon_1 d_2}{d_1\sigma_2(t) + d_2\sigma_1(t)} \qquad 1\text{-}20$$

with t corresponding to the time, d_1 and d_2 the thickness of the two layers.

The evaluation of this formula can become more complicate for the non-linear field dependence of the conductivity or for its dependence with the temperature. The situation changes when we consider an applied electric field above the threshold for space charge injection [Chr15]. According to simple MWS calculations, the amount of interfacial charge should scale with the applied voltage (or field) [Wag14]. Increasing the electric field above the threshold for space charge accumulation, the charge begins to be injected from the electrodes and accumulate at the interface affecting the net charge measured at the interface. This asks for a model which can take into account charge injection processes at the electrode-dielectric interfaces.

1.4.1.2 Microscopic scale

Charge injection and extraction at the interface between electrode and dielectric has been described at the macroscopic scale considering phenomena characteristic at lower scales, like the charge energy depth or the roughness of the interface.

A first attempt was made be modelling the charge dynamics at fields above the threshold for space charge accumulation [LeRo05]. In this dynamic model, electronic charge injection, an exponential

distribution of charge traps and hopping charge transport were introduced. Recently, this approach has been further improved in a bipolar model [Taleb13]. This model assumes that the interfacial region a higher density of exponentially distributed trapping sites is present. Although this model can predict some of the space charge profiles measured at higher fields there is still work to be done to obtain the thickness of the interfacial region because the parameters of the model are directly linked to it.

For smaller size, of the order of micrometers to several tens of µm scale, other kinds of –unwanted– interfaces related to defects in the dielectric, such as air-filled cavities, inclusions and asperities on electrodes. One interface that deserves particular attention is between an air-filled cavity and a dielectric. Gas PD in the cavity lead to the formation of chemical species and to high energy (hot) electrons. Both may attack the dielectric at the interface. These irregularities alter the border conditions of macroscopic models and are important in the progressive material aging [Mors13].

Two materials that compose an interface can be physically or chemically bonded, depending on the type of accessory. A purely physical bond is where pre-moulded joints are bonded using an elastic compressive force. A chemical bonding is realized where both sides of the interface share the same type of insulation and in addition to be extruded, these are subjected to a process of crosslinking. It is observing the influence of defect and impurities that scientist begins to study and characterize the properties of nanocomposites [Lewi94].

1.4.1.3 Nanometric scale

Interface description at nanoscale was pushed by nanocomposite development. Two approaches co-exist to treat interface at microscopic scale: modification of electrical properties due to charges or structural/morphology modification [Lewi94]. The main approach is proposed by T. Tanaka et al. who combine morphological and electrical properties changes in the interphase layer. This model explains that around nanoscale size fillers, the matrix properties are modified due to differences in polymer chain organization (morphology) and a three-core model for electrical properties based on Gouy-Chapman model was proposed [Tana05]. Based on this approach, for nanocomposite applications, one attempt was done to prove the influence of interface on macroscopic properties [Tana11].

1.4.1.4 Molecular and atomic scale

The models of high field conduction [LeRoy05] [Taleb13] are based on trap densities and depths for which a full explanation has not been found in spite of extensive efforts [Teys01]. “Traps” are, in fact, an abstraction of impurity states in the band gap which are caused by a range of morphological and chemical phenomena in the material [Huza10]. In the framework of Density Functional Theory (DFT), the calculation of the electronic structure for crystalline [Huza10] or amorphous [Unge13] polyethylene structure includes defects and impurities. In particular, the most studied are trap levels for defects like carbonyl groups at different chain locations, various double and triple bonds, hydroxyl and vinyl groups, and for impurities relevant for insulation applications, like acetophenone,

alphamethylstyrene, cumene, cumyl-alcohol, and water. It turns out that conjugated double-bonds and carbonyl groups yield generally the deepest traps. Shallow traps are seen for single double bonds in the PE chain, hydroxyl groups, and water. Traps originating from water, vinyl or hydroxyl groups have depths similar to the band gap of the amorphous-crystalline interface of PE; thus, these later defects could at high enough concentration bridge the interface phases yielding a sub-band in the band gap of PE [Unge13].

1.4.1.5 Limits of the different approaches

A lot of studies highlight that interfaces are the key feature to control charge injection [Nea09] [Che16] [LeRo05] mainly because classical models as Schottky law failed to explain injection. So, some attempts were done to introduce additional parameter as interface charge density [LeRo05] to fit with experimental results. Unfortunately, this approach failed to explain entirely all phenomena, mainly because models at local scale are built with macroscale measurements.

Moreover, even if interfaces are described at different scales, physical phenomena occurring close to it remain poorly understood. This is mainly due to the lack of interface properties characterization at local scale.

Some attempts are identified in the literature to probe interface between semiconductors for photovoltaic or MOS applications [Kali00] [Kryv16]. These studies probe the metal diffusion at Al/In_2O_3 interface thanks to an electrical mode derived to Atomic Force Microscopy (AFM) named Kelvin Probe Force Microscopy (KPFM). S.V. Kalinin et al. [Kali00] demonstrated that the interface junction in $SrTiO_3$ is larger in surface potential mapping than in topography. These results are promising, and the approach seems to be adaptable to study accurately interfaces in dielectric polymers.

To conclude, there is a wealth of processes likely to be at play at interfaces, and a wealth of functions, being topological, electrical, or chemical, likely to be influential in these processes. The very need, with all these ideas in hand, is relevant characterization of these interfaces by state of the art techniques. The ambition of this thesis is to contribute to the experimental characterization of interfaces.

1.5 Objectives of the thesis

As shown previously, interfaces seem to have a strong impact on charge injection in dielectric polymers. However, this influence is, up to now, mainly an assumption, even if a lot of attempts have been done during the last thirty years to describe interfaces at different scales. The main objective of this research project is to characterize interfaces at the nanoscale and to identify its impact on charge injection and transport. To reach this goal, pure PE was chosen as dielectric material to avoid additive and impurity influence. A semicon/PE interface will be investigated due to its extensive use in HVDC cable applications. This interface will be investigated from micro to nanoscale point of view. The originality of our approach consists in the use of modes derived from Atomic Force Microscopy (AFM) to probe the morphology and electrical properties of interfaces with nanoscale resolution. These characterizations will be completed by macroscale measurements.

This PhD thesis is divided in three chapters in addition to the first one dedicated to the state of the art. The second chapter concerns both samples processing and characterization methods. PE and semicon/PE/semicon sandwiches are processed using press-moulding technique. Different protective layers (PET, Al…) were used to modify surface properties. Different measurement techniques will be presented to probe:

- Surface chemical properties. To that purpose, Fourier Transform InfraRed (FTIR) Spectroscopy and PhotoLuminescence (PL) measurements will be used.
- Charges injection and transport at macroscale. Pulsed ElectroAcoustic (PEA) method and time-resolved polarization/depolarization current will be used.
- Interfaces properties at nanoscale. Morphological and electrical properties are probed using Peak Force Quantitative NanoMechanical (PF-QNM) and Kelvin Probe Force Microscopy (KPFM) respectively.

Each technique will be presented succinctly, and experimental conditions will be detailed.

The third chapter is dedicated to the experimental results, which shed light on the influence of the moulding layer on the material properties and on the electronic behaviour of the insulator at the interface. These results will be further discussed in the fourth chapter, while the fifth chapter will summarize and conclude the PhD thesis with final considerations and future perspectives of research on interfaces in dielectrics.

Chapter 2
Experimental materials and techniques

2.1 Experimental strategy

The main objective of this work is to characterize interface properties and to determine their impact on charge build-up. To reach this goal the material manufacturing processes needs to be accurately controlled with particular care to surface characteristics in terms of chemical and microstructural aspects and their relation to processing conditions.

The next step is to propose complementary characterization tools to probe interface and related phenomena at relevant scale. Three kinds of characterization tools will be used:

- chemical characterization using photoluminescence (PL) and Fourier Transformed InfraRed (FTIR) spectroscopy;
- electrical characterization at macro or micro-scale using current measurements or space charge measurements by the Pulse Electro Acoustic (PEA) space charge measurement method;
- morphological and electrical properties at nanoscale, using techniques derived from Atomic Force Microscopy (AFM).

Three kinds of samples were processed with geometries suited to the techniques implemented to characterize it:

- single dielectric layer for chemical and morphological analysis;
- insulator layer with metal electrode for electrical characterization;
- insulator layer with two semiconductor electrodes for electrical characterization and cross-section measurement by AFM to probe interface properties.

In addition, still in the objective to keep control on the features of the interfaces, we have compared surface properties of samples prepared at different sites, namely ABB Research Centre Sweden and Laplace Laboratory site, in order to identify any deviation in the response that could arise from processing.

This chapter is divided in two parts. The first one will be dedicated to materials and sample processing. Two kinds of constraints guide the definition of samples and their form: the phenomena to be investigated and the characterization tools to probe it. The second part is dedicated to characterization tools description. Each technique will be quickly described before presenting experimental conditions used in this study.

2.2 Materials and samples manufacturing

The different kinds of samples were selected depending on the manufacturing labs (ABB or Laplace) and characterization tools used (constraints in term of thickness, metalized electrodes…).

2.2.1 Materials choice and properties

a) Insulation

As the main objective of this study is to address interface phenomena, the investigated insulating materials should present as less as possible bulk parasitic phenomena, as e.g. ionic transport. So, it should be as pure as possible, notably without additives or residues. As a reference insulation material, for this thesis, we used a non-stabilized low-density polyethylene from ExxonMobil™ under the commercial name "LDPE LD 101BA" [LDPE15]. It is designed for Medium/High Voltage insulation and can be crosslinked by adding the desired peroxide content. This material is distributed in the form of pellets and with an associated technical datasheet from the manufacturer which contains the material properties based on standard tests. Some of these properties are reported in Table 2-1.

This LDPE is provided in the form of pellets. For this reason, by exploiting the thermoplastic properties of polyethylene, through the processes described below, these are moulded into films form of the desired thickness as described in the following part.

Resin properties	Typical value	Test based on
Density	0.923 g/cm^3	ExxonMobil method
Melt index (at 190°C/2.16kg)	2.1g/10min	ASTM D1238
Peak melting temperature	110°C	ExxonMobil method
Electrical properties	Typical value	Test based on
Volume resistivity	$7.6 \cdot 10^{16}$ Ω·cm	ASTM D257
Dielectric strength	55 kV/mm	ASTM D149
Dielectric constant	2.2	ASTM D150
Dissipation factor	$4 \cdot 10^{-4}$	ASTM D150

Table 2-1 Material properties published by the manufacturer in the technical datasheet [LDPE15].

b) Semicon

In order to avoid that the contact properties are influenced by the diffusion of additives and impurities, a non-commercial semicon (SC) material with high purity has been processed for the needs of the thesis. It was realized with the same afore-mentioned LDPE as matrix and carbon black nanoparticles

distributed with the commercial name “Denka Black 50% CB” incorporated in it. To this purpose, a Brabender internal mixer has been used to mix LDPE/CB (50/50 wt.%) at 15 rpm for 15 minutes at 130°C. Afterwards, it has been cut in flakes with similar size as LDPE pellets. The preparation of the semicon into pellets was made at ABB Sweden site.

2.2.2 Single-layer manufacturing

The preparation of samples was achieved with processing single-layers of materials of 50µm or 200µm in thickness, followed eventually by assembling the layers. The complete set of samples is given in section 2.3.5, after description of the techniques.

The moulding process of a single layer basically uses the thermoplastic properties of the polymer beyond their melting temperature to convert the pellets in a film, by using a mould to control the shape. Commonly in the literature a protecting film is placed at the interface between the metallic mould and the polymer in order to provide smooth surface and to avoid adhesion of the polymer to the mould. The influence of the protecting film on the insulator contact properties is one of the issues under investigation in this work.

Three different protection film materials have been selected from the most common in literature and current practise at lab scale:

- Aluminium (Al),
- Polyethylene Terephthalate (PET)
- Polyimide (PI).

The impact of the nature of the protecting film on the surface roughness, the chemical contamination and the film electrical properties will be studied in depth in the following chapters.

Since this thesis arises from a collaboration between ABB and Laplace laboratories, samples produced in both facilities are compared to establish a benchmark for the sample manufacturing process.

The press in the Laplace laboratory has two metallic press plates of 10 cm in diameter. As shown in Figure 2-1a, in order to realize the 200 µm thick sample, the mask has both top and bottom protecting films and an intercalated ring to maintain the polymer under compression once reached the desired thickness. The number of pellets (40, representing 1.20 g) was chosen in such a way that the sample volume was slightly lower than the inner space of the ring. The realization of a 50 µm thick film mask required further considerations as a small variation in pellets weight corresponds to a major variation in the film diameter. For a film thickness of 50 µm and 6 cm in diameter, 0.21 g of LDPE are needed, corresponding to about 6-7 pellets. In Figure 2-1b we can notice that an extra disk was added to the centre of the mask leaving a gap between the disk and the ring to collect the excess resin volume. The ring thickness was adjusted so that the difference between the disk and the ring was 50 µm.

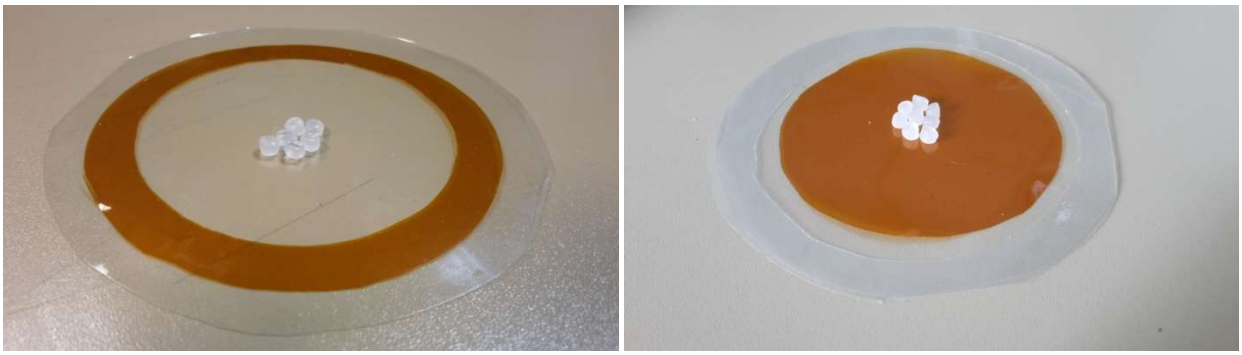

Figure 2-1 Example of mask used in Laplace to mould the films with thickness of 200 µm (a) and 50 µm (b). In the latter case an additional disk is present in the middle as well as a gap to collect the excess resin volume.

In the ABB Laboratory the metallic press plate has a square shape of about 40 x 40 cm² surface area. Thick films of 200 µm thickness were produced in disk shape with a diameter of about 20 cm. Also in this case, there are two protecting films in contact with the upper and lower surfaces of the film and a ring that delimits the sample size, but the latter has a different function compared to its analogue used in Laplace. Its thickness is lower than the desired one (two layers of 75 µm each) and part of the resin flows under it (Figure 2-2a). The resin flow is limited by exploiting its thermoplastic properties. The thickness is dependent on the temperature, the pressure and the flow rate of the resin. It can be experimentally controlled by varying the time during which the sample is subjected to temperatures higher than the melting point. The mask shown in Figure 2-2b allows the correct the amount of LDPE to have a resin flow sufficient to cover the part above the disk with the desired thickness of 50 µm. The weight of the pellets used for the two samples was 8g and 3g respectively for 200µm and 50µm.

The hot-presses of both laboratories can control the time evolution of external parameters such as temperature and pressure. The pressurization and temperature cycle for the implementation of the samples is given in Figure 2-3. In a first phase, the pellets are subjected to the maximum temperature in order to melt it. The pressure is then gradually increased to force the resin flow into the mould and avoid the formation of bubbles. Finally, the sample is cooled down.

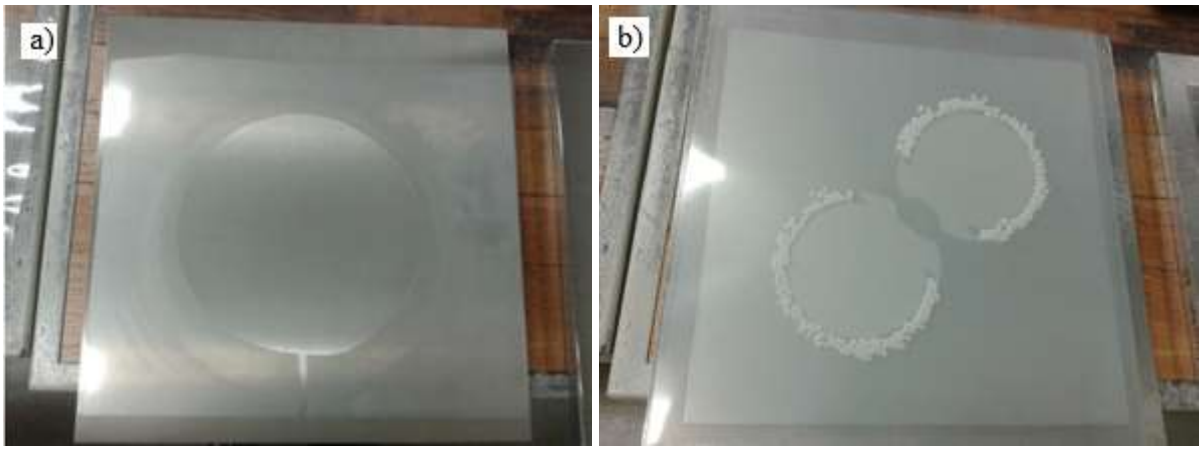

Figure 2-2 Two examples of masks used in ABB to realize samples of thickness 200 µm a) and 50 µm b).

The major differences between the two protocols concern

- the maximum temperature: 140°C in Laplace and 150°C in ABB
- the cooling rate: respectively 2.3°C/min and 7.7°C/min. Unfortunately, limited by the thermal inertia of the cooling system, it was not possible to reach the same cooling rate in Laplace as in ABB.
- The extraction temperature which depends on the cooling rate. In the ABB protocol the sample is extracted from the press directly at 80 °C, as opposed to the Laplace protocol where extraction takes place at room temperature.
- As to the pressures, they cannot be compared in a straightforward way as it can apply on the intercalated film or on the melted resin itself under flow.

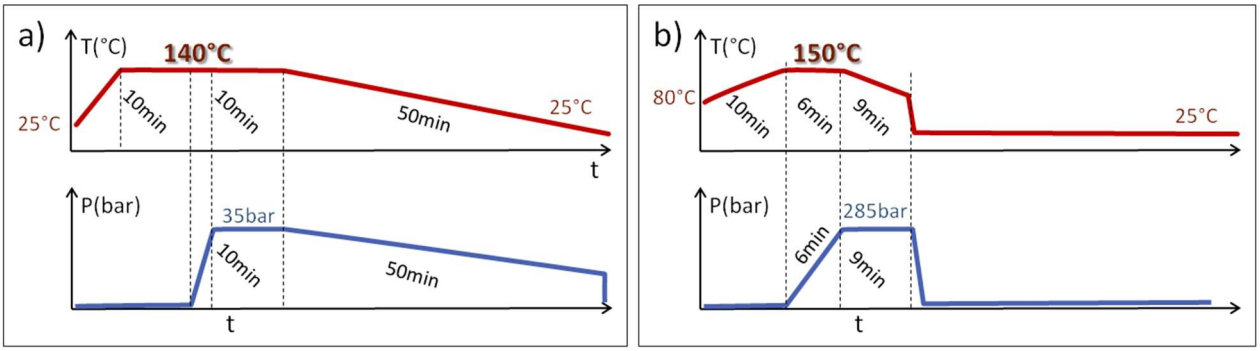

Figure 2-3 Comparison between the LDPE single layer hot-press protocols realized in a) Laplace and b) ABB

These protocols have also been used to mould semicon films. In the manufacture of semicon films, the increased viscosity made it difficult to produce thin film of large diameter. The sample provided by ABB, with a diameter of about 22 cm, could not be processed into a film thinner than 170 µm due to the higher viscosity of resin. The use of this film proved to be difficult. After several attempts it has been possible to note that, by reducing the amount of material, it is possible to produce thin films with a smaller diameter. The films realized in Laplace with a thickness of 50 µm have a diameter of 4 cm with about 0.9 g of bare semicon. Each single layer thickness has been measured using a palmer with a precision of 5µm.

2.2.3 LDPE films with gold electrodes for electrical measurements

For samples exposed to HV stress, gold electrodes are deposited for good contact and control of the applied electric field. Figure 2-4 illustrates the system Scancoat 6 SEM sputter coater from Edwards used for the gold metallization. It is a compact bench-top sputter coater designed to high quality deposition of a wide variety of specimens, conductive metal (such as gold) film.

The electrode area is delimited by a metal mask covering the portion of the sample that will not be metalized. The parameters of the sputtering process are listed in Table 2-2. The sputtering pressure is about 0.15 mbar of Argon gas. The voltage and current are 1 kV and 10 mA, respectively [Qiao15].

Sputtering properties	Value
Rate	0.1 nm/s
Gas	Argon
Pressure	0.15 mbar
Voltage	1 kV
Current	10 mA
Time	300 s

Table 2-2 Parameters of the gold sputtering process.

The insulating polymer films are provided with gold electrodes having a thickness of 30 nm (the centre area is about 30 nm, while the edge area is about 26 nm). The diameter can be 40 mm or 10 mm depending on the use.

Figure 2-4 Gold metallization setup, Scancoat 6 from Edwards.

2.2.4 Three layers Sandwich manufacturing

The samples designed to study the semicon/insulator interface present two parallel contact surfaces, realized by melting two semicon electrodes on a LDPE film. A surface suitable for the AFM analysis of this sample was conceived by cross-cutting the sample.

The preparation method can be schematized in the following four different steps:

- Manufacturing one LDPE and two semicon layers as described in Figure 2-5a. The individual layers are cut to the desired diameter and aligned.

- Melting the three layers together (Figure 2-5b). Around each layer a support ring is installed, having the same thickness as the single layer (50 µm). The hot-press protocol to melt the layers together is similar to that for single layer adopted in Laplace, but the maximum temperature is reduced to 110°C (Figure 2-6). The lower temperature and the support ring prevent the mixing of the three layers with each other. The result of this is a sandwich-like sample of 150 µm thickness with two parallel semicon insulator interfaces.
- Cutting off the sample into small triangles (Figure 2-7a) whose dimension is few millimetres large in order to have a wider contact surface for the electrodes and a support to hold the sample vertically.
- Thinning an angle using the ultra-cryo-microtome to obtain a sufficiently smooth surface (Figure 2-7b). At the same time, the tip of the triangle has a size that can be plated with the ultra-cryo-microtome. The cutting with ultra-cryo-microtome has been achieved at Biotool platform of IBCG. This setup is commonly used to produce organic samples in very thin film form as necessary for electron microscopy measurements. By freezing the sample in liquid nitrogen, slices about 200 nm in thickness can be produced with the diamond blade. For our own application, we use the smooth surface left on the base sample to make AFM characterizations on cross-sections.

This surface is about 150µm wide and few hundred microns large (Figure 2-7c). After this treatment the surface is flat enough to measure the contact properties in cross-section.

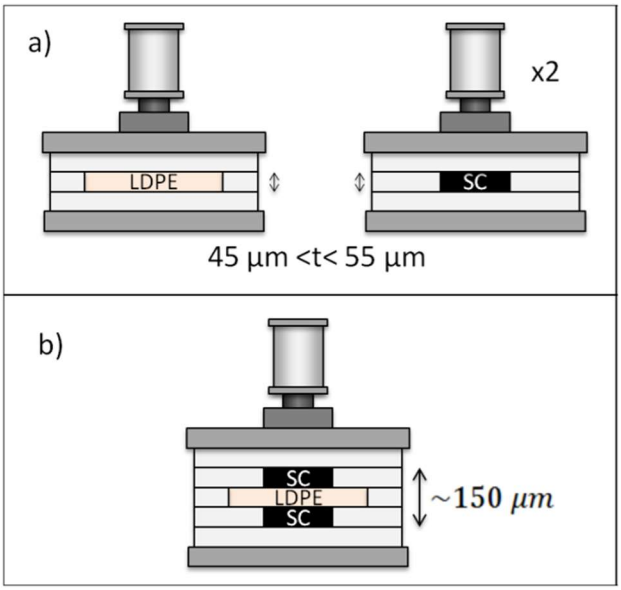

Figure 2-5 Graphic representation of the steps necessary to make a SC-LDPE-SC sandwich: Fig. (a) shows the realization of the required single layers, while (b) shows how these are assembled together.

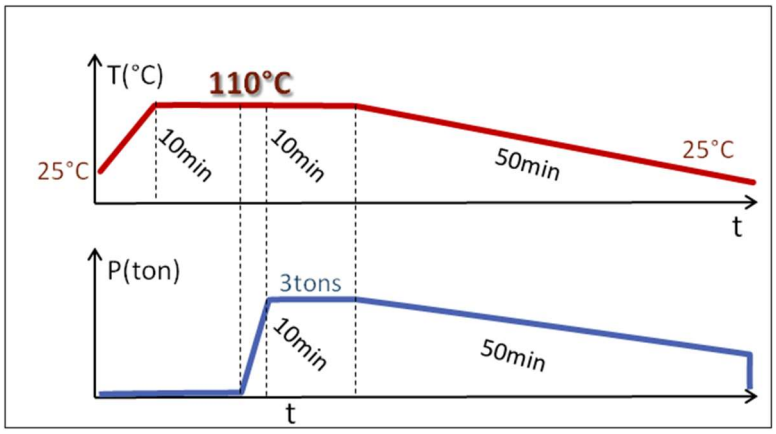

Figure 2-6 Hot-press protocol to melt together the three layers of the SC-LDPE-SC sandwiches.

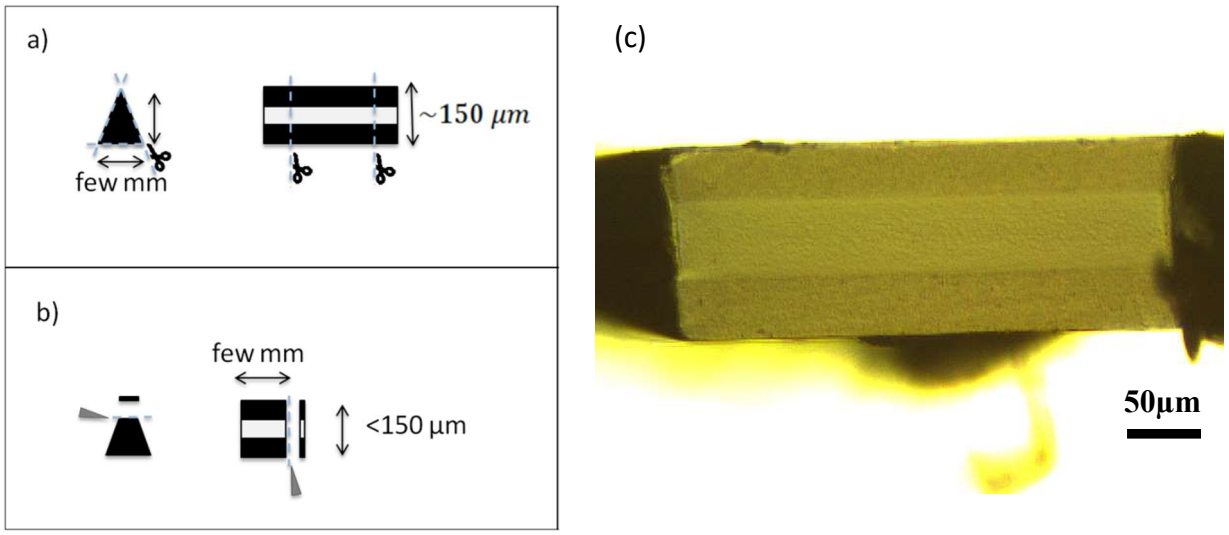

Figure 2-7 Graphic representation of the procedure to cut a SC-LDPE-SC sandwich and prepare a cross-section surface for the AFM. In a) the sample is coarsely cut into triangular shape to fit in the sample holder; in b) the sharper angle is precisely shaved with an ultra-cryo-microtome that offers a flat cross-section surface as requested for the AFM; c) Cross-section surface observed with the optical microscope integrated in the AFM setup.

2.3 Experimental setups

2.3.1 Chemical characterization

2.3.1.1 Photoluminescence setup

The Photoluminescence (PL) technique consists in collecting light emitted by a sample during irradiation at fixed wavelength. The resulting spectrum exhibits emitted light intensity as function of emitted wavelength, which could be analysed in terms of chemical groups contribution [Takai78] [Alle79]. Alternatively, it is possible to analyse the excitation spectrum of PL, representing the intensity of light emitted at a given wavelength, as a function of the excitation wavelength.

The Lab-made PL experimental set up used for the present work is presented on figure 2-9 [Tiem99] [Teys01]. The illumination source consists of a 150W Xenon lamp from Jobin-Yvon with bandwidth between 0.2 nm-4 nm (thanks to a coupled monochromator). In our measurements the bandwidth is fixed to 4nm. The excitation wavelength range is from 200 nm to 700 nm.

The emitted light is collected by a CCD camera (Charge Coupled Device) from Princeton Instruments (LN /CCD-1100-PB) working at a controlled temperature of -110 °C, which requests a constant supply of liquid nitrogen. This camera is associated with an imaging spectrograph (type: Jobin-Yvon CP200) which ranges at 200 lines/mm. It covers a spectral range between 190 nm and 820 nm. The sensitive part of the camera has resolution of 1100 × 330 pixels, each pixel covers an area of 24 × 24 µm, but the information is summed over the 330 rows. The spectral resolution is 4.5 nanometres. The optical coupling between the sample and CCD camera is achieved by the path through the quartz lenses window of the chamber. A high pass filter at 300 nm protects the CCD camera from the source UV light cutting off the excitation wavelength shorter than 300 nm. The emission spectrum is integrated by the CCD camera over a time window to be adapted to the intensity of the signal to be measured. For photoluminescence it is typically of a few seconds. In electroluminescence where collected light is of much lower intensity, the integration time can be of several minutes [Qiao15]. All measurements were realized in air at room temperature.

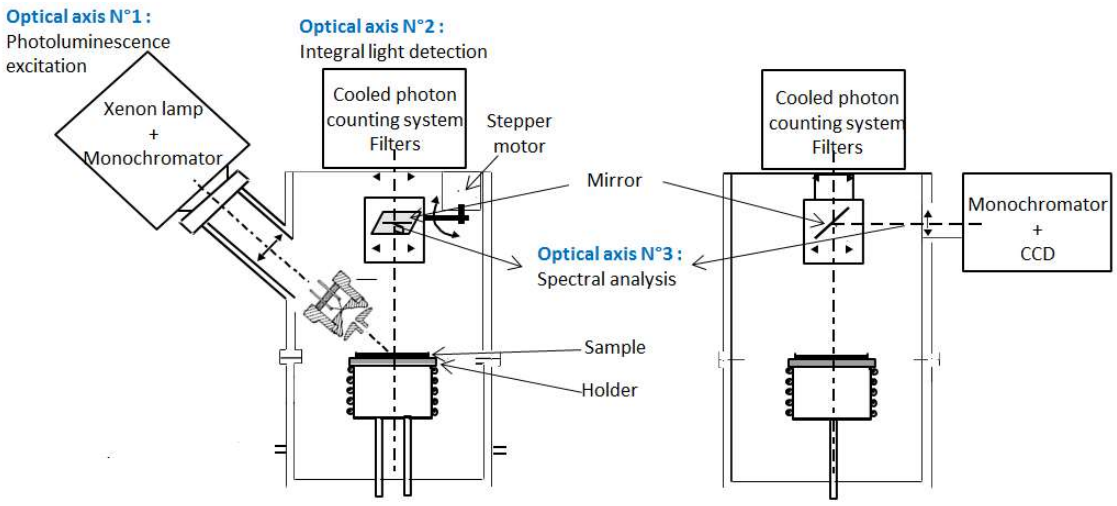

Figure 2-8 Photoluminescence experimental setup. Here optical axis N° 1 (for photoluminescence excitation) and N° 3 (for emitted light collection with the CCD) are used.

2.3.1.2 Fourier Transform Infrared Spectroscopy setup

Fourier Transform Infrared (FTIR) spectroscopy consists in probing chemical functions in the film by analysing vibronic modes of the optical absorption. Therefore, the energy levels considered are of lower magnitude than in photoluminescence. A Vertex 70 FT-IR spectrometer in ATR (Attenuated Total Reflexion) mode from Bruker was used, with PLATINUM Diamond ATR accessory. All spectra are acquired by averaging 20 scans with a spectral resolution of about 4 cm^{-1}. In ATR mode the sample is in direct contact with the diamond crystal. The evanescent wave extends beyond the crystal trough the sample for a penetration depth (d_p) defined by the following formula:

$$d_p = \frac{\lambda}{2\pi\sqrt{n_2^2 \sin^2\theta - n_1^2}} \qquad 2\text{-}1$$

where λ is the wavelength of the light and θ is the IR beam angle of incidence which in our case is fixed to 45°. The two refraction indexes n_1 and n_2 correspond respectively to diamond (2.4) and LDPE (1.5). In our case the penetration depth is between 0.5 µm - 5 µm, depending on the wave number (Figure 2-8).

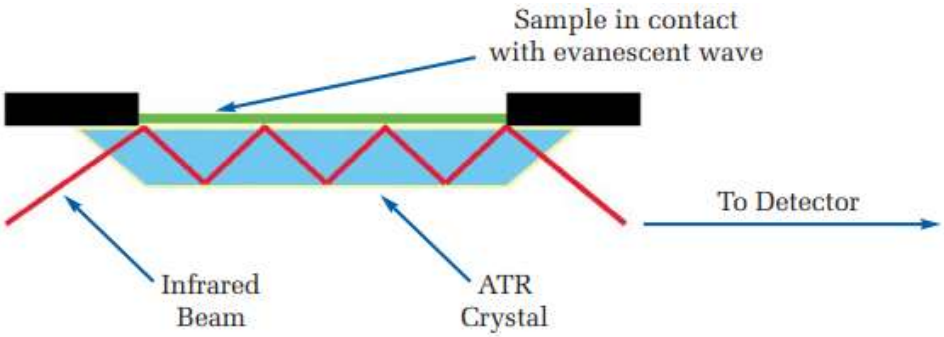

Figure 2-9 A multiple reflection ATR system [Elme15].

2.3.2 Electrical characterizations

2.3.2.1 Current measurement setup

The current measurements were done using 200µm-250µm thick LDPE samples which were previously metalized with gold electrodes (electrode diameter 40 mm, with area of about 12.6 cm^2).

The scheme of sample arrangement for current measurement is presented on figure 2-11 [Vu14]. A silicon ribbon is deposited at the periphery of the electrode to avoid edge phenomena. The HV applied by means of a 35kV / 0.5mA DC supply, model FUG HCP35-35000. A Keithley 6512 electrometer is used to measure the current.

The arrangement shown on Figure 2-10 is deposited on a thermostatic sample holder, with a fluid circulating in it whose temperature is regulated by a cryo-thermostat. Measurements were carried out at room temperature (22° C) and at 50° C.

For each temperature, polarization/depolarization current measurements were performed applying electric fields from 5 kV/mm to 30 kV/mm with a step of 5 kV/mm. Each polarization/depolarization

step has a duration of 3h. The current values are recorded every 5 seconds during the entire polarization/depolarization phase.

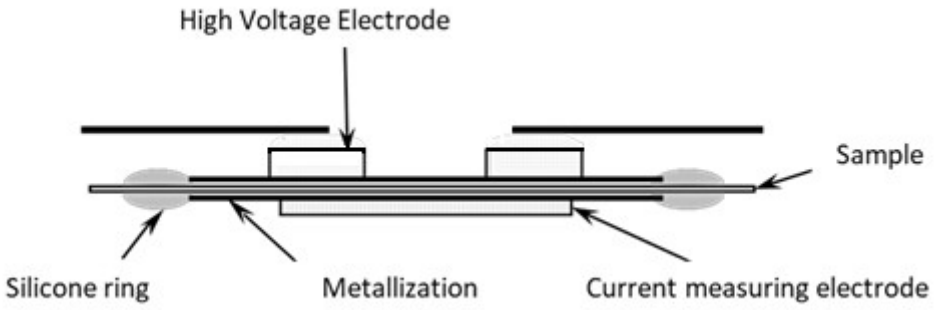

Figure 2-10 Experimental setup for measuring the conduction current of plane samples [Vu14].

2.3.3 Space charge probing by Pulsed Electro-Acoustic method

In this work, the Pulsed Electro Acoustic method (PEA) [Mizu94] is used to compare the volume charge build-up in samples manufactured using different protecting layers (Al, PET and PI) or contacted with different electrodes (Gold and semicon).

The principle of this method consists in applying electrical pulses by means of a pulse generator to a sample placed under direct or alternating voltage. Under the effect of the pulses, the space charges present in the dielectric move around their initial position. The acoustic waves generated by the charge displacement are detected by means of a piezoelectric sensor. In this method, the sample is placed between two electrodes (Figure 2-11). The upper electrode consists of a semiconductor material to minimize wave reflections at the interface with the sample. This electrode is connected to the high voltage supply and to the pulse generator. The aluminium bottom electrode is connected to ground. A PVDF piezoelectric sensor is placed under the lower electrode and converts the acoustic waves into an electrical signal. Finally, under the PVDF an absorber is placed in poly(methyl methacrylate) (PMMA).

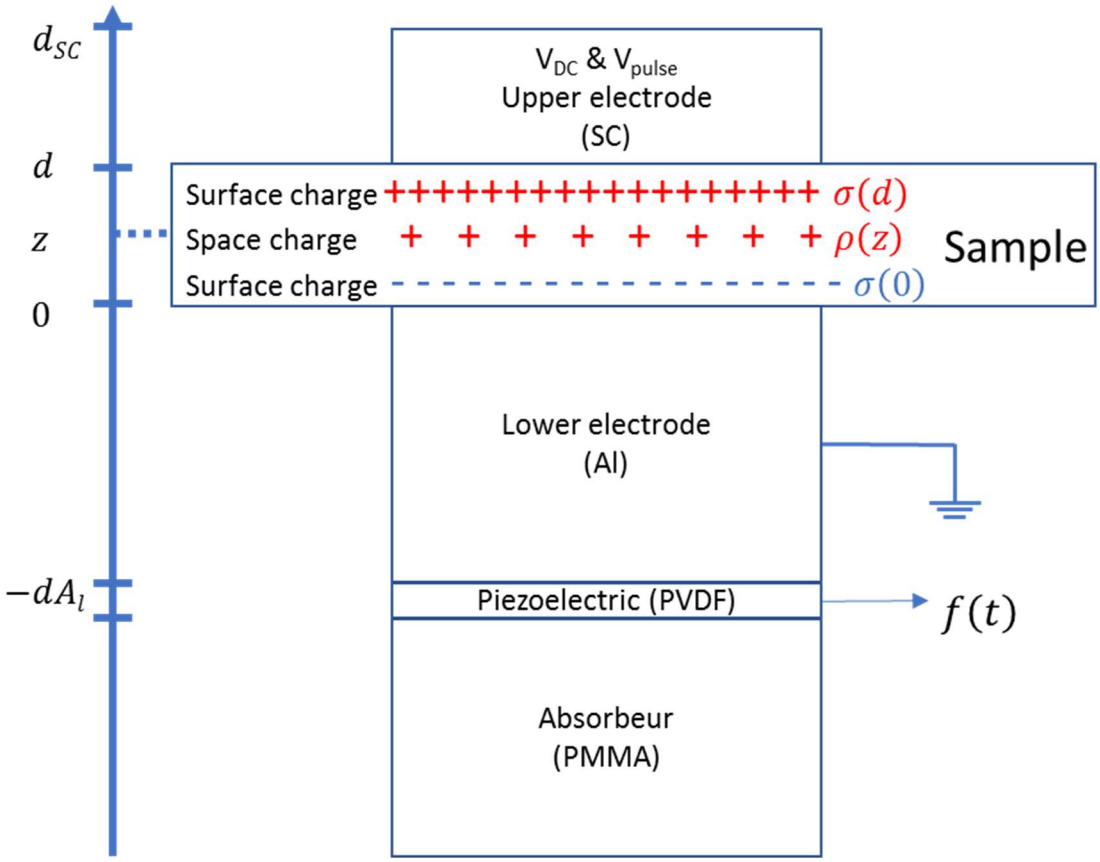

Figure 2-11 Principle and main elements of a PEA cell [Viss11]

The PEA cell is placed in a thermalized chamber, which makes possible to set the temperature in the range between 0°C and 70°C. This PEA test bench is well suited for the space charge measurement in flat samples with a thickness between 200 and 500 µm. A pulse generator stimulates the sample to generate the sound wave and produce a trigger signal to synchronize the data capture. The maximum amplitude of the pulses is 2 kV and the maximum repetition frequency is 50 kHz. For 200 µm films, 0.6kV amplitude pulses offer good compromise between signal quality and non-intrusive character for the measurement. The pulse width at half height is of the order of 5 ns. The high voltage is supplied by a DC voltage generator (model FUG HCP35-35000) which allows to perform polarity reversals with voltages between -35 and +35 kV. In addition, the DC high-voltage generator can be controlled from a PC via a GPIB bus with the possibility of programming long-term protocols. A Lecroy 204Xi digital oscilloscope, with 2 GHz bandwidth, is dedicated to trigger and acquire the acoustic signals from the device, which allows capturing short signals with a good time resolution. The oscilloscope also has a very high processing speed, which makes possible to average a large number of raw signals in a relatively short time, improving the signal-to-noise ratio. It is controlled via an Ethernet link and the data are recorded and processed by a computer to calculate the space charge profiles by deconvolution method [Viss11].

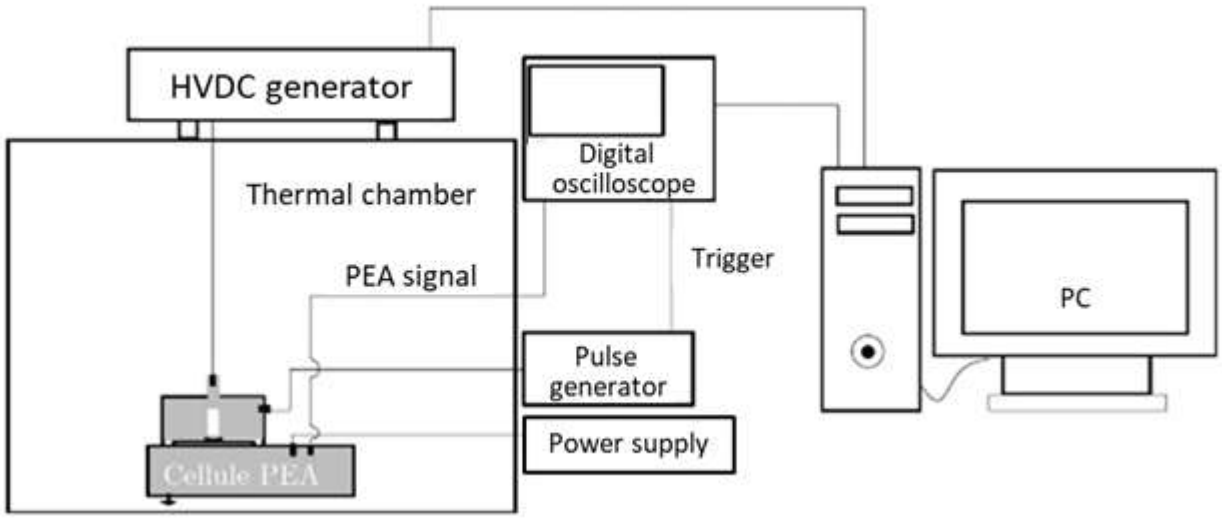

Figure 2-12 Schematic of the PEA setup [Viss11].

The measurements were carried out for applied fields varying between 10 and 30 kV/mm, followed by a polarity reversal to -30 kV/mm. (10, 20, 30, -30 kV/mm) under isothermal conditions. Polarization/depolarization phases last 3 hours and the space charge profiles are recorded every 60 seconds throughout the cycle.

2.3.4 Morphology and electrical characterization at nanoscale

Atomic force microscopy (AFM) is a powerful tool to analyse not only the sample surface topography but also to probe its mechanical and electric properties at nanoscale. This is realized by exploiting the AFM probe-sample surface interaction whose forces vary in nature and in interaction length. As example, interactions through Van der Waals forces are exploited to probe surface topography whereas electrostatic forces are used to probe electrical properties as surface potential.

In this work, a Multimode 8 set up from Bruker was used. Two modes derived from AFM were exploited:

- Peak-Force Quantitative NanoMechanical (PF-QNM) to analyse surface topography and mechanical properties;
- Kelvin Probe Force Microscopy (KPFM) to probe surface potential which is related to material intrinsic properties and electrical charges.

Table 2-3 summarizes some AFM applicative modes which are classically used for material characterization. As far as dielectric materials are concerned electrical modes are extensively exploited to probe local dielectric constant (EFM) [Ried09], injected charges (EFM or KPFM) or conduction properties (C-AFM/TUNA) [Ishi10] [Reze09].

<table>
<tr><th>Topography modes</th><th>Mechanical modes</th><th>Electrical modes</th><th>Thermal modes</th><th>Magnetic modes</th></tr>
<tr><td>Contact [Capp99]</td><td>Force Distance Curve (FDC) [Capp99]</td><td>Conductive AFM (C-AFM/TUNA) [Lanz17]</td><td rowspan="4">Scanning ThermoMicroscopy (SThM) [Gome99]</td><td rowspan="4">Magnetic Force Microscopy (MFM) [Hart99]</td></tr>
<tr><td>Tapping [Capp99]</td><td>Force Volume (FV) [Radm94]</td><td>Scanning Spreading Resistance Microscopy (SSRM) [Vand94]</td></tr>
<tr><td>Non-contact [Capp99]</td><td>Peak-Force (PF) [Youn11]</td><td>Electrostatic Force Microscopy (EFM) [Reze09]</td></tr>
<tr><td rowspan="2">Peak-Force (PF) [Youn11]</td><td>Lateral Force Microscopy (LFM) [Pele13]</td><td rowspan="2">Kelvin Probe Force Microscopy (KPFM) [Nonn91]</td></tr>
<tr><td>Friction Force Microscopy (FFM) [Benne15]</td></tr>
</table>

Table 2-3 The various derivatives of AFM.

2.3.4.1 Morphology characterization by PF-QNM

PF-QNM is an AFM mode that at every point of the scanned area can measure a force curve. A force curve is defined here as the recording of force-distance curve in a two steps process of approach and retract of the tip from the sample surface, see Figure 2-13. The peak interaction force is then used as the imaging feedback signal. Analysis of force curve data is done in real time, providing a map of multiple mechanical properties with the same spatial resolution as the height image. All AFM techniques are based on an accurate measurement of the cantilever deflection signal by means of the laser reflection on the back side of the cantilever. In PF-QNM mode, this time-dependent signal is called “heartbeat” because of its similarity to an electrocardiogram. The signal periodicity is dictated by the oscillation of the piezoelectric Z motor. In Figure 2-13a, the dashed line represents a single time period of the piezoelectric Z position oscillation, synchronized to the solid line of the heartbeat signal. The period is characterized by five states: approach, contact point, peak force, adhesion and withdrawal [Pitt10].

To quantify the forces as well as other mechanical properties, it is important to perform a calibration procedure in three main steps:

- The deflection sensitivity S (units nm/V) measurement is performed by using a clean and hard surface (as silicon). As no deformation is induced on sample surface the slope of the force distance curve in contact area (Figure 2-14b) corresponds to the link between electrical signal delivered by AFM detector and displacement (piezoelectric displacement) [Ohler07];

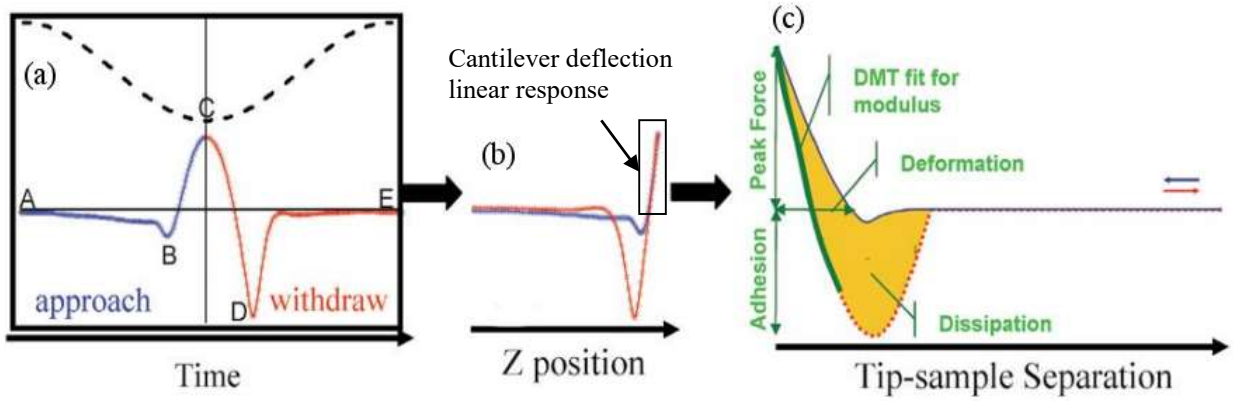

Figure 2-13 Characteristic peak force signals in function of time (a), piezoelectric Z position (b) and force vs. tip-sample separation (c). In Figure (a) the dashed line represents a single time period of the piezoelectric Z position oscillation synchronized to the solid line of the heartbeat signal. In (b) the cantilever deflection signal is correlated to the piezoelectric Z position. In (c), after the calibration process, the force vs. tip-sample separation shows how parameters as DMT modulus, deformation, dissipation, adhesion and peak forces can be determined [Pitt10].

- The cantilever spring constant k is determined using thermal tune mode [Hutt93]. Thanks to these parameters, the electrical signal v delivered by AFM detector is converted in force F with the following relation (Figure 2-13c):

$$F = k S v \qquad 2\text{-}2$$

- The Peak Force setpoint represents the maximum repulsive force of the tip-sample interaction and sets the beginning of the withdraw (retract) phase.

For the PF-QNM measurements of single layer samples in plan-view, the Bruker's probe model SNL-A has been used. This probe includes four cantilevers with varying degrees of force constants and resonant frequencies. Among these, the most suitable was found to be the one with the nominal resonant frequency of about 65 Hz and the nominal cantilever spring constant of about 0.35 N/m. Peak Force Tapping mode modulates the AFM probe oscillation at ~2 kHz, with a default Peak Force Amplitude of 150 nm. The PeakForce setpoint is fixed to 1.4 nN.

To obtain quantitative measurement of Young's modulus an additional calibration step is needed. Performing this calibration requires:

- A reference sample whose Young's modulus is in the same range as that of the investigated sample

- A model for Young's modulus: Derjaguin-Muller-Toporov (DMT), or Hertz, Sneddon, Johnson-Kendall-Roberts (JKR) [Maug00]

The calibration step consists in measuring Young's modulus on a reference sample and adjusting the effective tip radius to reproduce the theoretical value. This effective value is used in the following to characterize our sample.

To investigate LDPE, the reference sample consists in a thin layer of PMMA and the Young's modulus is determined using DMT model.

2.3.4.2 Electrical characterization by KPFM

The KPFM technique provides a map of the Contact Potential Difference (CPD) which corresponds to the surface potential difference between AFM tip and sample. This mode is based on the electrostatic force induced on the tip by electrostatic potential difference. It exploits one the AFM's capability to detect small forces.

a. KPFM theory

KPFM measurement in Amplitude Modulation mode (AM-KPFM) is performed in lift mode. So, two measurement steps are required to measure topography and surface potential difference CDP.

- First step: topography measurement in tapping mode. This step could be done as well in PF-KPFM mode.
- Second step: AFM probe mechanical oscillation is stopped; the tip is lift from the surface with a height h and an external bias V_e is applied so as to cancel the electrostatic force:

$$V_e = V_{\mathrm{DC}} + V_{\mathrm{AC}} \sin(\omega t) \qquad 2\text{-}3$$

where V_{DC} is a direct current bias and VAC is alternative current bias with the same pulsation as mechanical resonance frequency.

Since the sample-probe system forms a capacitor (with capacitance C), if a potential difference ΔV is present between them, the corresponding electric force F_{el} will be equal to:

$$F_{el} = -\frac{1}{2}\frac{\partial C}{\partial z}(\Delta V)^2 \qquad 2\text{-}4$$

where ΔV is the sum of the intrinsic CPD and the externally applied potential V_e:

$$\Delta V = V_{\mathrm{DC}} - V_{\mathrm{CPD}} + V_{\mathrm{AC}} \sin(\omega t) \qquad 2\text{-}5$$

Combining the equations 2-4 and 2-5, the following expression for the F_{el} is obtained:

$$F_{el} = -\frac{\partial C}{\partial z}\left((V_{\mathrm{DC}} - V_{\mathrm{CPD}})^2 + \frac{1}{2}{V_{\mathrm{AC}}}^2\right) + \quad \text{DC term}$$
$$-\frac{\partial C}{\partial z}(V_{DC} - V_{CPD})V_{AC}\sin(\omega t) + \quad \omega \text{ term} \qquad 2\text{-}6$$
$$+\frac{1}{4}\frac{\partial C}{\partial z}{V_{\mathrm{AC}}}^2\cos(2\omega t) \quad 2\omega \text{ term}$$

In Amplitude Modulation mode (AM-KPFM), the surface potential difference between the tip and the surface is now determined by tuning the DC voltage VDC to cancel the electrostatic force F (ω term). As the force depends on the first derivative of capacitance, the potential measurement is sensitive to parasitic capacitances which limit the lateral spatial resolution [Jaco98] [Meli11]. So, the lift distance should be as short as possible to limit parasitic capacitance and improve lateral resolution [Zagh10]. Moreover, in case of high surface potential difference, a large electrostatic force is induced, which introduces topography error (apparent height) and might screen potential measurement [Zieg08]. This introduces a limitation for space charge probing in case of large charge density. To improve the lateral resolution other variants of the KFM method based on Frequency Modulation (FM) instead of Amplitude Modulation (AM) can be used, minimizing the sensitivity to parasitic capacitance [Zieg11].

b. KPFM condition measurement

KPFM measurements are done using SCM-PIT probe. The nominal resonant frequency is about 75 Hz and the nominal cantilever spring constant about 2.8 N/m. A lift of 40 nm was used for all KPFM measurements.

2.3.4.3 PF-QNM and KPFM measurement on cross-section

KPFM measurements were performed on sandwich SC/LDPE/SC samples in cross section. The PF-KPFM analysis of the mechanical and electrical properties relative to the three layers allowed clearly distinguishing the two interfaces separating each layer. Furthermore, AM-KPFM measurements were realized in order to measure the surface potential difference and thus evaluate the electric field distribution as well as the spatial charge distribution across the insulator. This was done firstly by grounding the two lateral electrodes and then by applying a transversal bias across the cross-sectional area. A home-made electrode system has been designed, providing a modified AFM sample holder. Indeed, to keep the sample upright, a steel vise clamp sample holder from Leica has been used with an aperture range between 0 and 2mm. In a first phase of the measurements, the two semicon electrodes are connected to ground through the metal sample holder. Afterwards, two external electrodes were added to the sides of the sample, blocked by the vise. As shown in *Figure 2-14*, each electrode consists of a rigid metal plate in contact with the sample, a thin strip of copper welded to a wire and an insulating film to avoid short circuit with the vise and between them.

This improvement allows the sample to be laterally biased on both the work bench and inside the microscope chamber. A 4V potential difference can be applied during measurement.

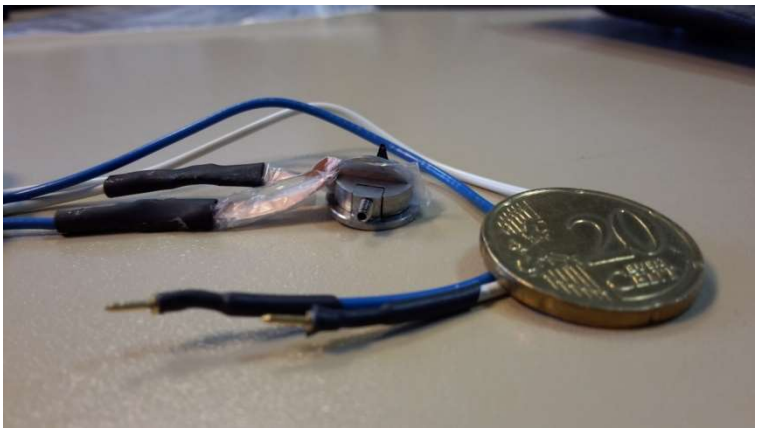

Figure 2-14 AFM sample holder and external electrodes designed to apply an external lateral bias to the sandwich during the cross-section measurement.

2.3.5 Wrap up of samples characteristics as function of characterization constraints

The sample characteristics have been adapted to the type of measurement. The choice of film thickness has been influenced by many aspects and has required some compromises depending on the specifications of the different instruments. The advantages of reducing the sample thickness rely on the possibility to have a greater average electric field in the sample with the same external potential applied and to increase the importance of interface as compared to bulk phenomena. On the other hand, the difficulties of sample thinning are inevitably related to the limited thickness control during sample preparation. Moreover, PEA measurements require samples with minimum thickness of the order of ~200 µm, while AFM does not allow for measurements on too thick samples. For these reasons, samples with different thickness have been selected, i.e. 200 µm and 50 µm for PEA and AFM, respectively. Hence, the samples will be further differentiated by the diverse protecting films used during the hot-press moulding process.

Measurement as the PL, the FTIR and the AFM can be performed directly on the bare materials. These are preliminary measurements on the contact surface that will form the interface with the electrode. In order to perform the electrical measurements, both gold and semicon electrodes have been exploited. In the first case a thin gold layer of about 30nm has been deposited by sputtering process in both sides of the LDPE film. While in the second case, two semicon layers, with thickness of about 50 µm, processed by means described in the paragraph 2.2.4, have been melted with the LDPE film to form a sandwich-like sample. The electrodes have a circular shape and a diameter of 1 or 4 cm depending on the contact surface required by the measuring instrument. Table 2-4 shows a schematic summary of the samples described above and their characteristics.

N°	Kind of sample	Laboratory	Target thickness	Protecting film	Electrode diameter	Characterization tools
1	LDPE single layer	Laplace	200 µm	Al, PET, PI	/	PL
2		ABB		Al, PET		
3		Laplace	50 µm	Al, PET, PI		FTIR and AFM (contact surface)
4		ABB		Al, PET		
5	LDPE + Gold electrodes	Laplace	200 µm	Al, PET, PI	1 cm	PEA
6		Laplace		Al, PET, PI	4 cm	Conductivity
7		ABB	250 µm	PET		
8	LDPE + semicon electrodes	Laplace	200 µm	PI	1 cm	PEA
9		Laplace	50 µm	Al, PET, PI	4 cm*	AFM (cross-section)
10		ABB		Al, PET		

*Table 2-4 Scheme of the samples that summarizes their characteristics and the measure for which they were intended. *4 cm refers to the diameter of the electrode before being cut, as described in paragraph 2.2.4.*

Chapter 3
Single layer characterization

3.1 Physico-chemical Characterization

In this section, the results on LDPE single layer films processed with different protection layers will be discussed. The chemical analysis has been performed by using the interaction between the material and the electromagnetic radiation in two spectral ranges, the infrared and the middle ultraviolet. The first range, between 4000 cm^{-1} and 400 cm^{-1}, has been analyzed by means of the FTIR setup described in the section 2.3.1.2, allowing for the detection of the vibrational modes of PE chains. Moreover, residual traces of the manufacturing byproducts or contaminations induced by the protecting layer can be revealed as well.

3.1.1 FTIR

Polyethylene has a relatively simple molecular structure, which is why it lends itself well to an analysis of its vibrational modes in the infrared. In Figure 3-1 the typical absorption peaks of the polyethylene chain are represented. Results for the LDPE pellets and for films processed with different protective layers are showed. The most important vibrational modes in this spectrum are correlated to the symmetries of the two hydrogen atoms which oscillate around the carbon atom of the PE monomer. The two peaks at 2916 cm^{-1} and 2849 cm^{-1} correspond respectively to asymmetric and symmetric stretching of the C-H bonds from their equilibrium length of about $r_{CH} = 1$ Å [Tear59]. The bending mode is also clearly visible, being represented by the pair of peaks at 1472-1464 cm^{-1}, which correspond to the scissoring motion of the two hydrogen atoms centered around an equilibrium angle $\angle HCH$ of about 107°. Finally, the rocking mode, i.e. the simultaneous oscillation of the two hydrogen bonds around the same angle of 107°, induces the pairs of peaks located at 730-719 cm^{-1}. Here, both the bending and the rocking mode appear to be splitted into two pairs of peaks because of the effect of the dipole-dipole interactions which is still measurable at room temperature [Krim56].

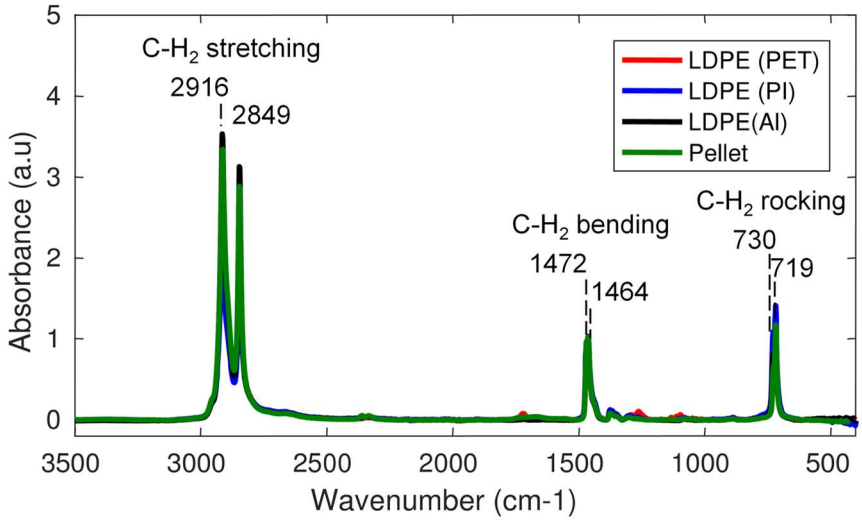

Figure 3-1 Broad range FTIR spectra of LDPE in form of pellets and films processed using different protecting layers. ATR mode with internal reflection angle of 45°.

According to the literature [Koen66], the three components at 1369, 1298 and 1353 cm^{-1} can be associated with CH_2 groups wagging mode, while the weak band at 1080 cm^{-1} is assigned to a skeletal frequency in the amorphous phase of the polyethylene chain. Only the components at 1377 cm^{-1} and 889 cm^{-1} can be correlated with the CH_3 group commonly found as termination of polyethylene chains. The range 1750-1580 cm^{-1} indicates the occurrence of oxygen contaminations, especially C=O groups in amorphous content [Liang59], a large peak in this region is presented by analysing the core of the LDPE pellets before being moulded (Figure 3-2, green line). After heat treatment this band disappears almost totally in the LDPE samples processed with Al and PI (Figure 3-2), leaving a small peak around 1722 cm^{-1} characteristic of the carbonyl group stretching. The higher intensity of these peaks, found in the LDPE processed with PET (Figure 3-2, red line), may suggest at a first analysis a higher oxidation degree of the surface of polyethylene, while occurring in lesser extent for both LPDE PI and LDPE Al, as shown in Figure 3-2 by the blue and black line respectively. In LDPE PET is also relevant, compared to the others, the presence of other peaks at 1263 and 1097 cm^{-1} also possibly linked to an oxygen contamination, both indicating a stretching C-O bond, resonant at 1263 and 1097 cm^{-1}.

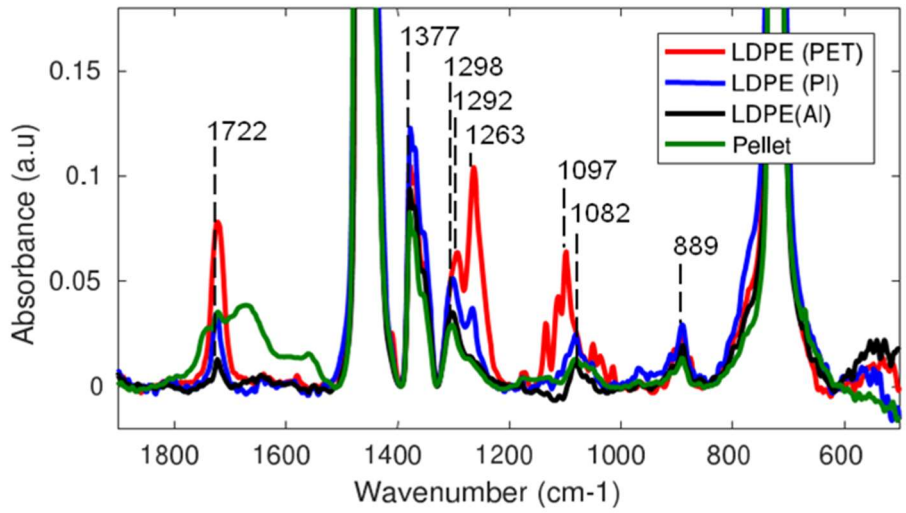

Figure 3-2 Zoom on the peaks of minor intensity of FTIR spectra of LDPE in form of pellets and films processed using different protecting layers.

According to the above results, the PET protecting layers produce specific changes in the FTIR spectra compared to the other protecting layers. It appeared interesting to check if the protecting layer itself can transfer moieties to the LDPE likely to explain these changes. The structure of the PET molecule, which contains CO bonds, is shown in Figure 3-3.

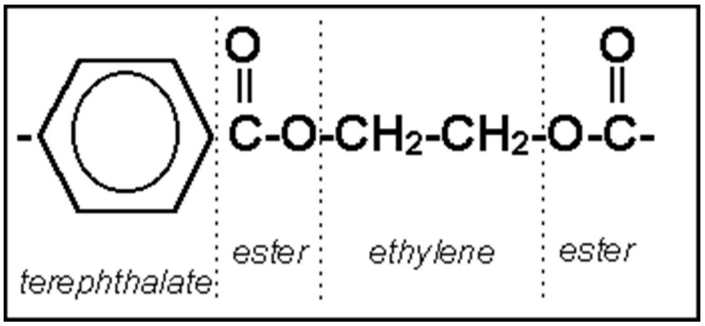

Figure 3-3 Repeat unit of the PET molecule

In Figure 3-4, the spectra of LDPE Al, LDPE PET and the PET protective film alone, are compared. Ester groups are known to give rise to two strong π absorption bands associated to O=C-O and O-C bond, assigned to the bands at 1263 and 1120 cm^{-1} respectively [Liang59]. The presence of two π bands in the 1100 cm^{-1} region may be indicative of the dependence of the stretching O-C mode from the neighboring CH_2 groups belonging to cyclic ethers or Alkyl-substituted ether. This led us to infer that the peaks related to the C and O bonding may be a sign of contamination of PET coming from the protective film, rather than an oxidation effect. Table 3-1 summarizes the assignment of the main bands detected in PE processed with different protecting layers.

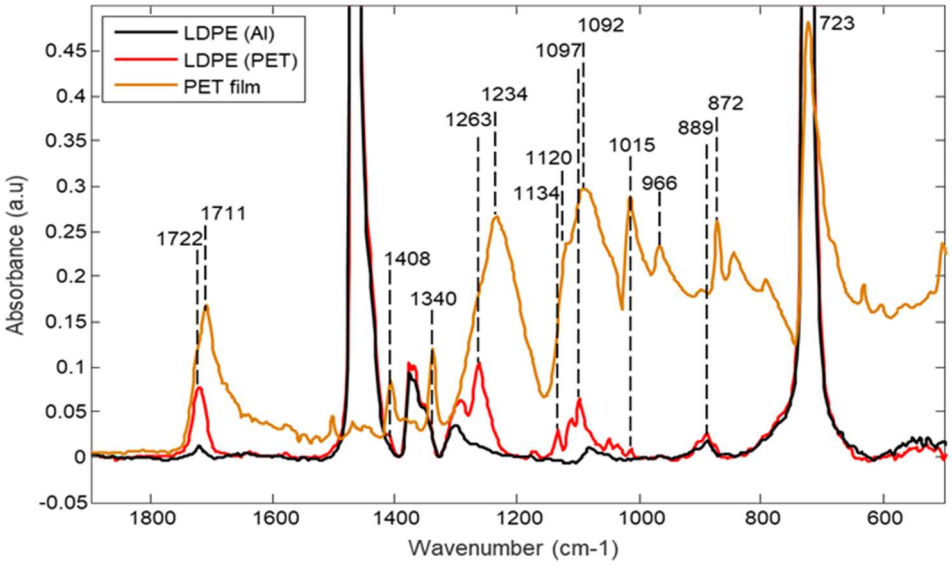

Figure 3-4 Comparison between the FTIR spectrum of the LDPE film prepared using a PET protecting film in red and the aforementioned film in orange. The spectrum of an LDPE film prepared with an Al film has been added to underline the peaks correlated to a possible contamination.

Origin	Wavenumber cm^{-1}	Functional group / assignment
CH_2	729-716	Methylene rocking
C-O-O-C	890-820	Peroxides, C-O-O stretching
CH_3	890	CH_3 rocking, out-of-plane
C-O-C	1150-1050	Alkyl-substituted ether, C-O stretching
C-O-C	**1140-1070**	**Cyclic ethers, C-O stretching**
CH_3	1133	CH_3 wagging, in-plane
CH_2	1172	CH_2 wagging
C-O	**1263**	**C-O stretching**
CH_2	1376-1352	CH_2 wagging
CH_2	1472-1462	CH_2 bending
C=O	**1730-1725**	**C=O stretching, carbonyl**

Table 3-1 Origin of absorption bands found in PE films

3.1.2 Photoluminescence

The second kind of optical properties probed is photoluminescence. In principle, two kinds of spectra can be recorded:

- photoluminescence emission spectra consisting in providing the emission intensity as a function of the emission wavelength for a fixed excitation wavelength;
- photoluminescence excitation spectra consisting in plotting the light intensity monitored at a defined wavelength as a function of the excitation wavelength.

In 'perfect' polyethylene, normally no emission can be detected in the normal wavelength range (230 nm and beyond) analysis as only sigma bonds are present. The presence of unsaturated bonds is necessary to provide absorption, and this can be found in defects, additives and residues as explained before. Each luminescence moiety has characteristic excitation and emission wavelengths. However, these are not tabulated as can be IR bands, especially when working in solid solutions where the environment can change the energetic levels. Because of the presence of different defects, absorption and emission spectra can be constituted of different bands. Figure 3-5 shows different representations of the data obtained on LDPE pellets, and LDPE processed with either PET or PI protecting layers. The maps represent emission intensity vs excitation wavelength and position. The excitation wavelength was changed in 5nm steps from 220 to 300 nm to record the spectra and then images were processed. For the longest excitation wavelengths, part of the exciting beam is diffused and collected by the sensor. This is due to the fact that the long wavelength pass filter with onset at 300 nm does not completely block the long-wavelength tail of the incident light – therefore part of the images was censored - cf. bottom-right of images.

For pellets, Figure 3-5a and 3-5b, the excitation beam could be reflected in all directions including the analysis solid angle. Also, the amount of sample was not the same. Therefore, intensity cannot be compared to that obtained on films. The excitation peak in case of pellets is at about 225 to 230 nm with emission maximum at 335nm. The same emission is found by exciting at 280nm. An emission is found at about 390nm with excitation at 225nm / 240nm.

In the past a large amount of work has been dedicated to the identification of luminescence species in polyolefins, and more especially in LDPE. In their pioneering work, Charlesby and Partridge [Char65] established the relationship between luminescence and the intrinsic unsaturation, especially carbonyl groups, but they also pointed out that various aromatic impurities can play the role of luminescent centers. In the same period of time, Boustead and Charlesby [Bous67] showed that in LDPE prepared with benzoyl-based initiator, the emission originated from benzoic acid residues. Later on, the work by Allen et al. [Alle77a] [Alle77b] [Alle79] clearly established the implication of enone and di-enone unsaturated carbonyl groups in the luminescence of LDPE prepared using oxygen as an initiator and concluded that the source of the photoluminescence from commercial polyolefins was the same [Alle78]. Previous results on the photoluminescence of polyolefins achieved by the group strengthened this conclusion [Teys98] [Qiao16]. It was confirmed that the fluorescence emission of additive-free LDPE is a function of the state of oxidation of the polymer [Laur95]. The fluorescence peaking at 330-340nm in emission and phosphorescence spectra (at 450 nm) reported in [Teys98] for LDPE and PP are different from those associated with extrinsic unsaturations [Bou67],

but identical, with the same maximum and shoulders, to those associated with enone and di-enone intrinsic unsaturation [Alle77a] [Alle77b]. Finally, the similarity between photoluminescence of LDPE and PP underlines the common origin of the luminescent centers in both materials.

Allen and McKellar [Alle79] associated the fluorescence emission with the presence of unsaturated carbonyls of the enone type and the phosphorescence emission to the presence of unsaturated carbonyls of the di-enone type. They have the following general structures:

$$-CH = CH - CO - R$$

for the enone case, and

$$-CH = CH - CO - CH = CH - R$$

or

$$-CH = CH - CH = CH - CO - R$$

for the di-enone case,

which are the specific cases of the poly-enone series:

$$-(CH = CH)_n - CO -$$

with n=1 and n=2.

Fluorescence and phosphorescence emissions have been associated with different chromophores, mainly on the basis of the excitation spectra which are different for the singlet and the triplet emissions as reported for example by Boustead and Charlesby [Bous67].

The impact of ageing, in particular thermal oxidation, was addressed by Jacques and Poller [Jacq93a] [Jacq93b]. They also showed using model compounds that the fluorescence of conjugated moieties shifts to longer wavelength with the increase of the conjugation degree. After substantial oxidation, fluorescence of polyolefins can be found at about 380 nm or even beyond 400 nm. This appears related to the fluorescence of poly-ene or poly-enone sequences.

Given this background, it can be inferred that the fluorescence of LDPE from pellets exhibits the features of slightly oxidized LDPE, where the main emission at 330nm would reflect the presence of unsaturated carbonyl of the enone type and the small emission at about 380nm to fluorescence from polyenone sequences. The fact that sample is from pellets may have two consequences: the out-diffusion of residues (like antioxidant if some amount is incorporated) and the oxidation of the surface, which would result in more evident traces of related emission than when the sample is pre-melted (see below).

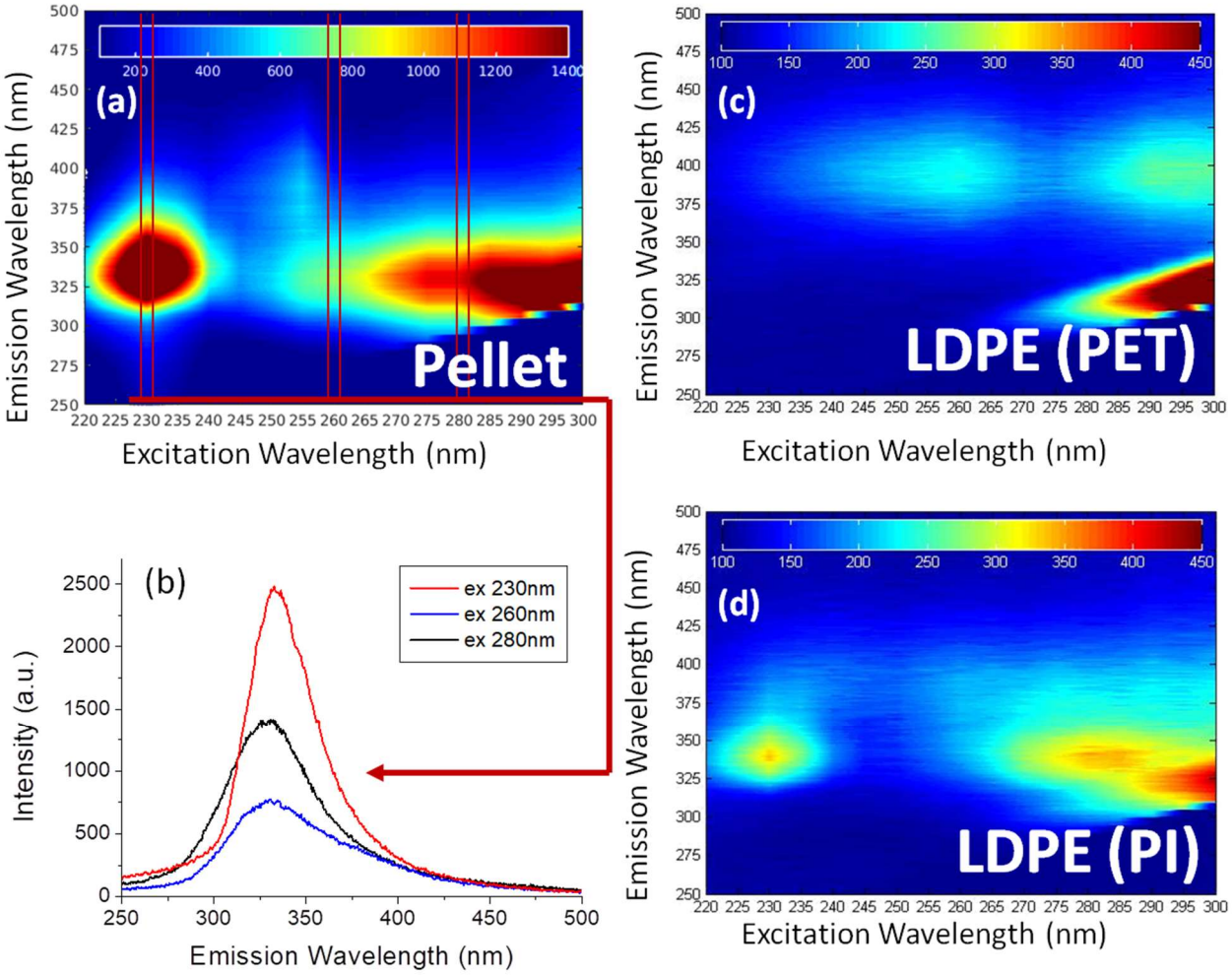

Figure 3-5 Maps of photoluminescence intensity vs excitation and emission wavelength obtained on LDPE as pellet (a), processed with PET (c). (b) Emission spectrum of LDPE pellets at 230 nm, 260 nm and 280nm.

The patterns for LDPE processed with PET or PI protective layers are quite different from those of the pellets. For PI cover layer (Figure 3-5d), the main emission is at 340nm (Figure 3-6a), and the excitation spectrum when monitoring at this wavelength reveals two maxima at 230 and 280nm (Figure 3-6a). Emission is found at 390nm too; however, it is not easy to identify where is the excitation maximum (Figure 3-6b). Therefore, it is considered that the process with PI modifies the emission obtained from pellets by reducing the relative contribution of the emission at 390nm. Considering the case of Al; Figure 3-6b, the emission at 390nm is even smaller.

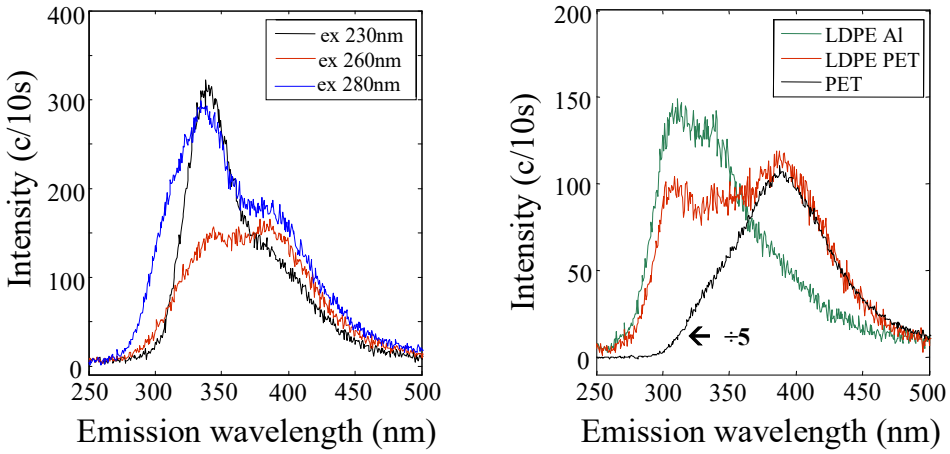

Figure 3-6 PL emission spectra: (a) as a function of excitation wavelength for PE processed with PI protecting layer; (b) for LDPE with Al or PET protecting layers compared to PET film. Excitation wavelength 280nm.

The PL features of samples processed with PET are substantially different from the others. First, surprisingly the band at 340nm is strongly reduced and even the peak at 230nm in the absorption spectrum is difficult to detect. Second, the main emission is at 395nm with excitation maxima at 255 and 295nm. In Figure 3-5c, the spectrum obtained on the PET protecting layer is presented. It shows the same features as those in LDPE processed with this protecting layer. The spectrum shown here is in line with that reported earlier using the same set-up, with a main band at 386nm and a shoulder at 335nm [Teys01b]. The structured emission of fluorescence has already been extensively studied. The generally admitted interpretation is that the emission at 336nm corresponds to the monomeric emission of PET. The one in the region 365-390 nm, has been interpreted as an excimeric emission [Takai78] [Cao88] or a ground-state dimer [Henn86] [Clau92] [Hash93]. Unlike excimers which result from interaction of nearby excited states, and dissociate once relaxed to their ground state, ground-state dimers are stable states formed by interacting aromatic groups. It means that the excitation spectra of monomeric and excimeric emission are the same, whereas it is in principle different in case of ground state dimers [Henn86].

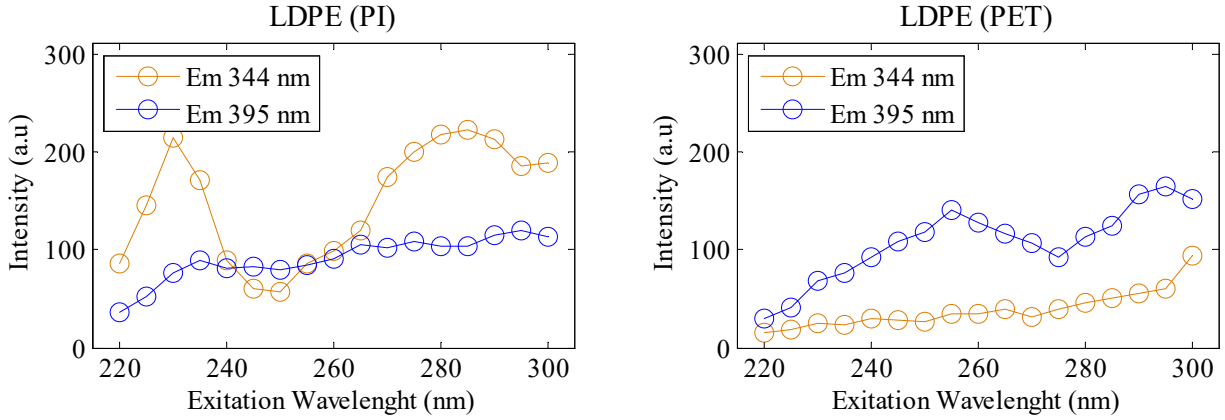

Figure 3-7 Comparison of photoluminescence emission at 344nm and 395nm of LDPE prepared using PI and PET.

Besides, the formation of ground state dimers requires that nearby aromatic rings belonging to different polymeric chains are close enough to produce interactions. Hemker et al. [Hemk88] observed an enhancement of this emission by uniaxial or biaxial orientation of the films and proposed to use it as a probe of orientation changes in the material. Orientation is expected to increase interaction between nearby aromatic rings thereby favouring ground-state dimers formation.

Considering now the place where the samples were processed, it can be observed in Figure 3-10 that grossly, that the shape of the spectra does not depend on the production site considering either Al or PET protecting layer. Regarding intensities, they are about the same for films produced at ABB or Laplace with Al protecting layers. The intensity is less by about a factor 2 for PET produced at ABB compared to that produced at Laplace. One of the differences in the process is that the flow of matter is more important in case of ABB process then at Laplace. So possibly the flow leads to a dilution of the changes occurring at the contact with PET.

PL results can be summarized as follows:

- the PL features of LDPE pellets and of LDPE processed with PI or with Al lead reveal the presence of alpha-beta unsaturated carbonyl of the enone type and of more conjugated groups like polyenones due do slight oxidation, Figure 3-8;

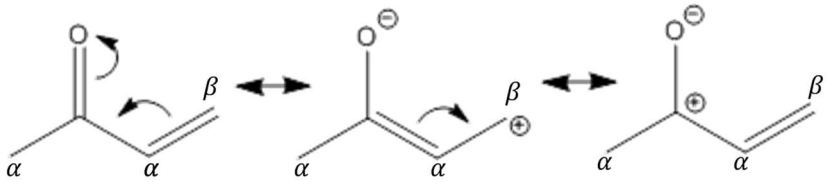

Figure 3-8 Resonant structures of alpha-beta unsaturated carbonyl.

- the signature of unsaturated carbonyl decreases after melting the pellets;
- with a PET protecting layer the emission at 340nm is strongly reduced and a main peak at nearly 400nm appears.

At least three processes can be put forward to explain the changes:

- oxidation at the contact with the protecting layer with different yield depending on the nature of the layer; for example, unsaturated carbonyl could be converted to enone sequences;
- reversible changes in the alpha-beta configuration of the groups at the surface, with a change to non-luminescent configuration, Figure 3-9;

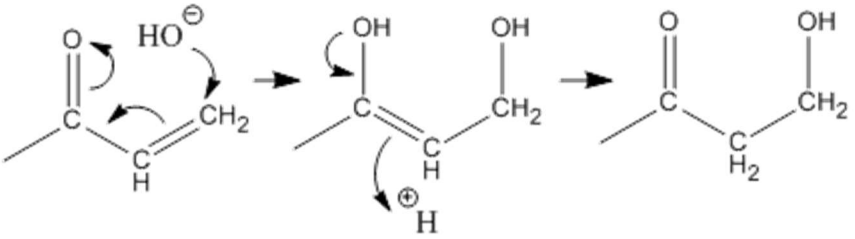

Figure 3-9 Nucleophilic attack on beta unsaturated carbonyl.

- diffusion of moieties like oligomer chains of PET from the protecting layer to the LDPE under the thermal treatment. Extrinsic chromophores so introduced can on one hand produce their own emission; on the other hand, they can also quench luminescence from the matrix.

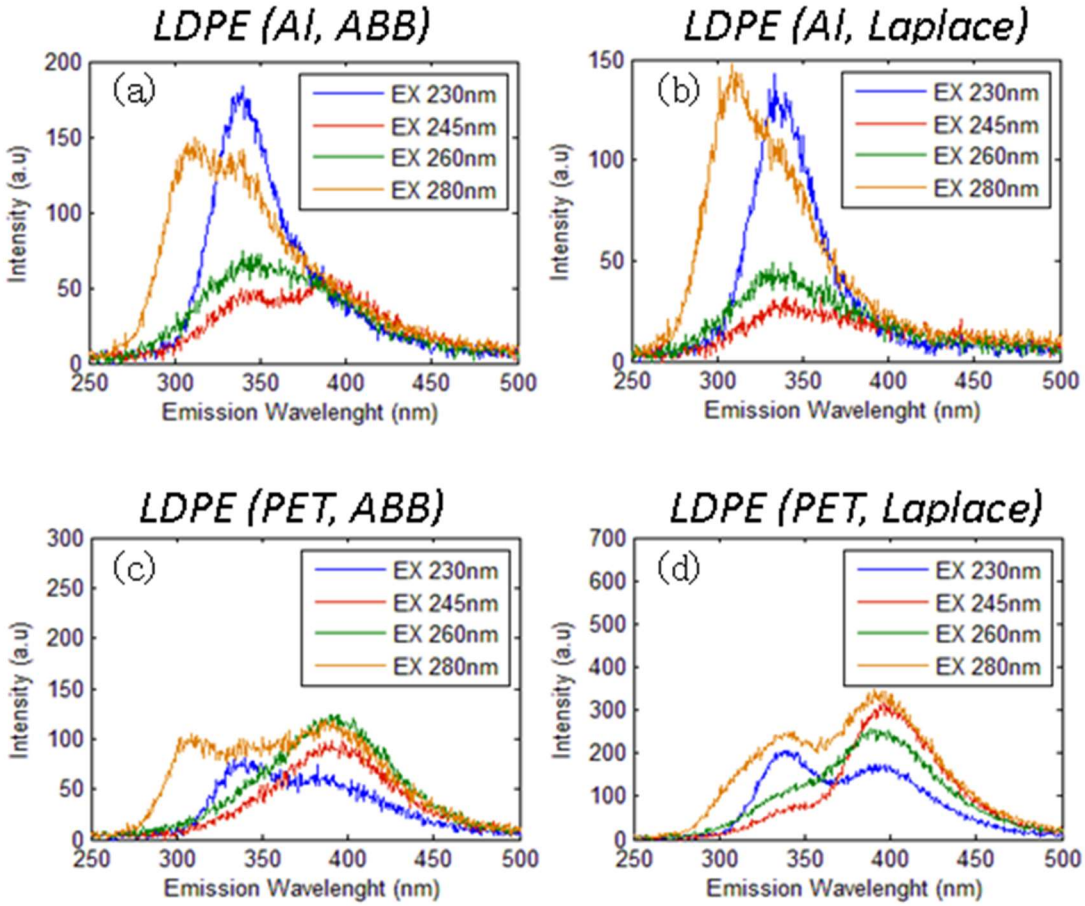

Figure 3-10 Comparison of photoluminescence at different excitation wavelengths of LDPE prepared using Al and PET, realized in ABB and Laplace.

The diffusion of PET moieties is most probably the main reason for the changes in PL features. This is confirmed by the presence of characteristic absorption bands in FTIR. Additional measurements like phosphorescence characterization could further confirm the process by revealing the presence of aromatic moieties. Also, the change in intensity of the emission when changing process can be linked to more dilution of the diffusing dies.

However, other features are appealing, notably the decrease of the initial emission at 340nm. PL itself does not probe specifically the surface of the film as far as the absorption of the material is not too strong: LDPE does not absorb substantially at wavelength larger than 230nm. So, we should consider the response as average from the bulk, except if the density of diffusing dies is important. The change in unsaturated carbonyl configuration is one possibility; however, the reason for specific efficiency in contact with PET along with any other chemical process induced at the contact with PET is difficult to conceive. So, at this stage not all the chemical modifications are identified; however, it can be put forward that PET protecting layer induces diffusion of moieties, which are possibly polar groups.

3.2 Topological Analysis

First of all, to investigate the impact of the manifacturing process on LDPE morphology, surface morphology was measured at different scales using PF-QNM mode.

Figure 3-11 shows the surface morphology of LDPE processed in Laplace using a PI protecting layer. The surface exhibits different patterns as function of probe scale. Indeed, at large scale (Figure 3-11a) a smooth and homogeneous surface is exhibited whereas at small scale (Figure 3-11c) fibrils with branching structures appear.

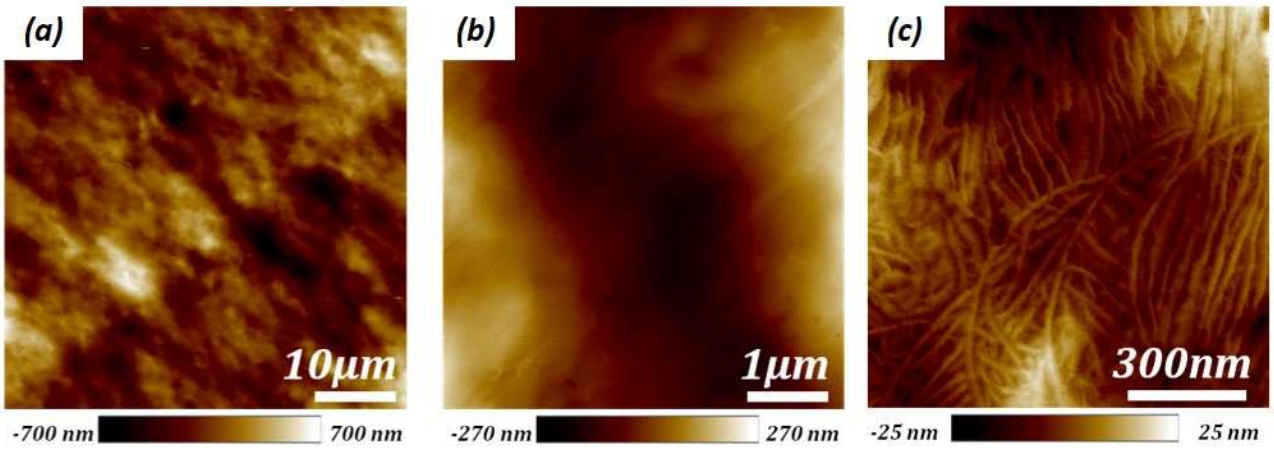

Figure 3-11 Surface topography measured in PF-QNM of sample processed in Laplace using PI protecting layer at different scales: (a) 50µm x 50µm, (b) 5µm x 5µm and (c) 1µm x 1µm.

Figure 3-12 compares the surface morphology of LDPE processed in Laplace using different protecting layers. As previously the surface exhibits different patterns as function of probe scale.

At large (Figure 3-12a and d) and intermediate (Figure 3-12b and e) scales, the protecting layer influences strongly the surface morphology. Indeed, the surface processed with an Al protecting layer exhibits large parallel groves, presumably due to foil machining whereas the surface processed with PET appears smoother. At lower scale (Figure 3-12 c and f) the surface is composed by a fibrils-like structure which seems to be less defined for the sample processed with PI. For Al protecting layer, fibrils appear only at some places which should be linked to large peak-valley height.

Figure 3-13 compares the surface morphology of LDPE processed in ABB using Al and PI protecting layers. Results are similar to the ones obtained at Laplace site at large scale, confirming the protecting layer influence on morphology. At lower scale no fibrils-like structure is observed for Al protecting layer whereas it is well defined for PET layer.

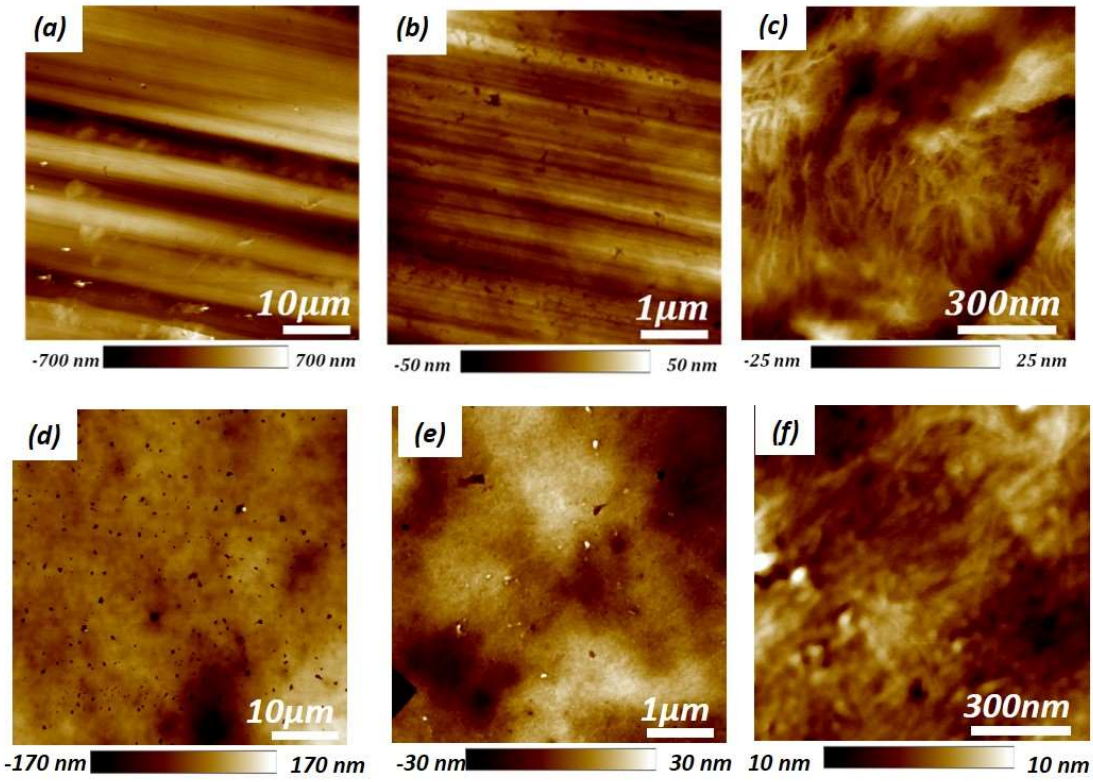

Figure 3-12 Comparison of surface topography measured in PF-QNM of sample processed at Laplace using Al (a-c) or PET (d-f) protecting layers at different scales: (a, d) 50µm x 50µm, (b, e) 5µm x 5µm and (c, f) 1µm x 1µm.

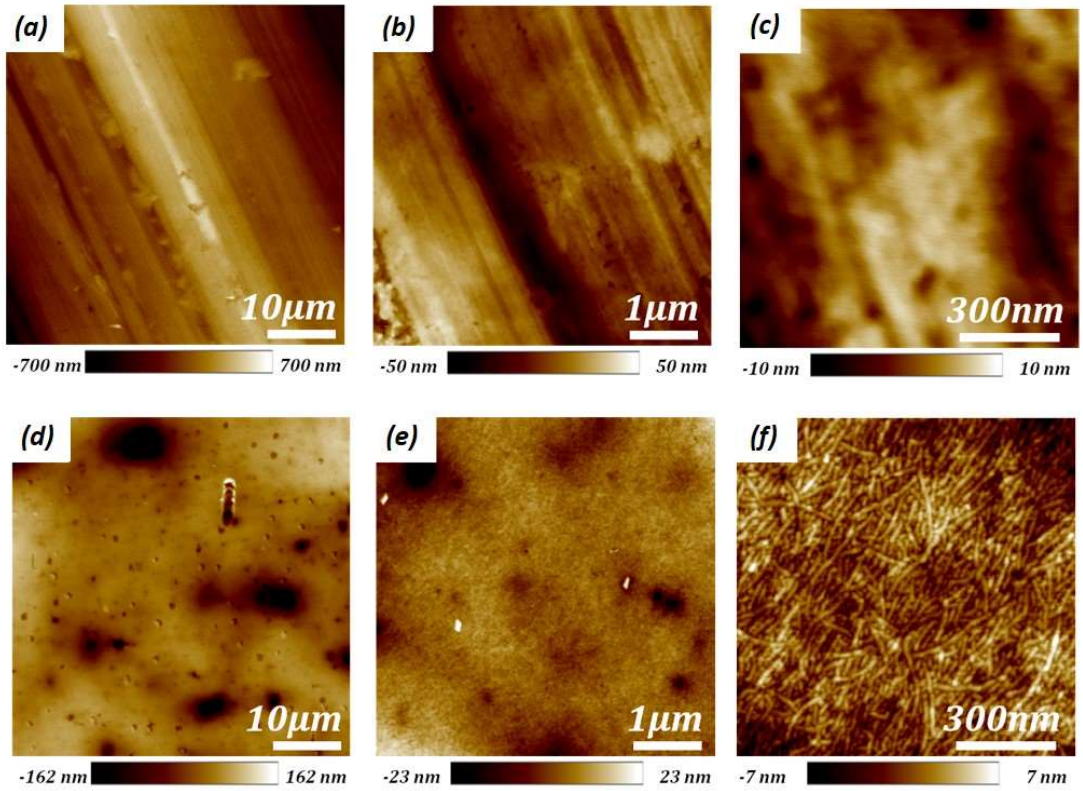

Figure 3-13 Comparison of surface topography measured in PF-QNM of samples processed at ABB site using Al (a-c) or PET (d-f) protecting layers at different scales: (a, d) 50µm x 50µm, (b, e) 5µm x 5µm and (c, f) 1µm x 1µm.

The comparison of the results depicted in figures from Figure 3-11 to Figure 3-13 highlights that very different patterns are obtained as function of the probed scale and the protecting layer used. To complete this study the roughness of the surface is investigated mainly because high roughness may induce local field intensification, hence possibly producing higher average current compared to that expected from a flat surface. In order to provide quantitative figures of roughness, images have been analysed resorting to the average value of roughness defined as:

$$R_a = \frac{1}{n}\sum_{i=1}^{n}|z_i| \qquad 3\text{-}1$$

Where n is pixel number and z_i represents the difference in height of the single pixel from the average plan of the surface.

Figure 3-14 shows the roughness estimated in function of the analysed squared image size. With increasing the size of the analysed area more coarse structures can be revealed. It appears that the sample processed with PET film is the smoothest one. With PI, grain-like structures of a few µm in size control the morphology. The groves in Al are at a larger scale. Possibly the roughness of PI appears with smaller size images owing to the change in dimensionality of the surface features (2D for PI, 1D for Al).

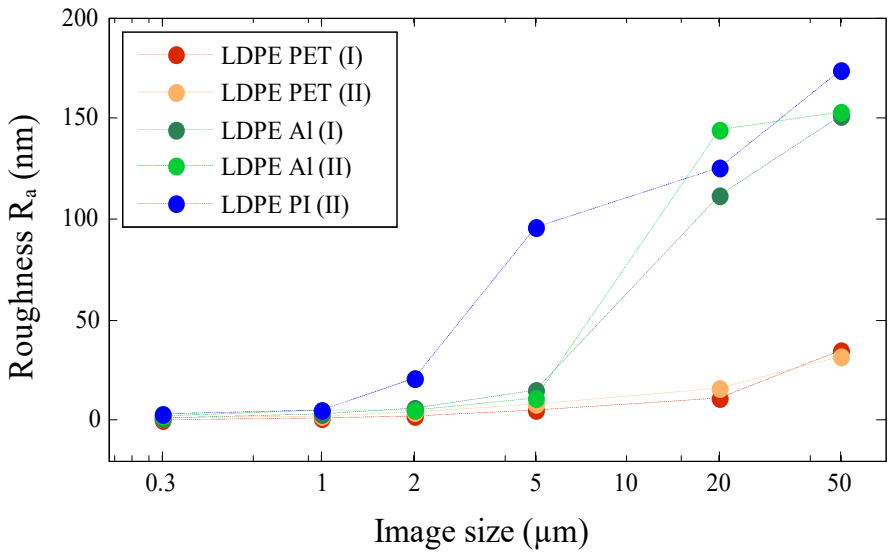

Figure 3-14 Evolution of LDPE surface roughness as function of probed surface size for different process and protecting layer. I and II refer to ABB and Laplace processes respectively.

To complete this study Young's modulus maps were recorded using PF-QNM mode. Young's modulus cartography measured over LDPE processed in Laplace using PI cover layer is presented on Figure 3-15. Even if surface morphology is homogenous (Figure 3-15a), spherulites extending over 2-3 microns in diameter are visible on the map (Figure 3-15b). Zoom on Young's modulus map shows that the lamella thickness is around 18nm (Figure 3-15b). So, the fibril-like structure observed previously at small scale should be linked to lamella imbedded in spherulites.

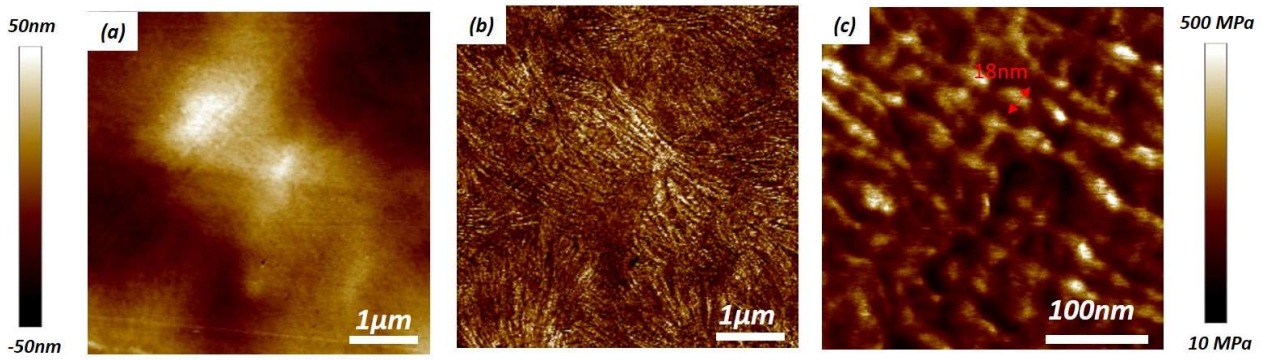

Figure 3-15 (a) topography and (b) Young modulus cartography over LDPE processed at Laplace using PI protecting layer on 5µm x 5µm surface. (c) 350nm x 350nm zoom over Young modulus cartography.

To conclude about the influence of the manufacturing process on LDPE morphology, the main characteristics are summarized in Table 3-2. Large scale morphology is only linked to protecting layer nature whereas film morphology at nanometre scale is influenced mainly by the process and in a lesser extent by the protecting layer. Lamellae are visible only for LDPE samples processed in Laplace. They appear organized in spherulites only for PI and Al protecting layers.

This difference between Laplace and ABB sample seem to be linked to the process. Indeed, one difference between the two processes is related to the cooling step. In the Laplace process the cooling is slow (around ten minutes) which probably permits material to organize. In case of the ABB process, the cooling is very quick, and this leads to a freezing of the structure.

Process	Protecting layer	Roughness (50µm x 50µm)	Morphology (1µm x 1µm)	Spherulites
Laplace	PI	170nm	Branching fibrils	Yes (2-3µm range)
	Al	150nm	Heterogeneous with fibrils	Yes (2-3µm range)
	PET	25nm	Heterogeneous with fibrils	Disorder lamella
ABB	Al	150nm	No fibrils	No
	PET	25nm	Fibrils	No

Table 3-2 Influence of LPDE process on surface roughness and morphology.

3.3 Space charge measurements

This section reports on and explains the measurements of space charge distributions obtained by the PEA method as described in the paragraph 2.3.3. These measurements have been performed on 200 µm-thick LDPE films realized with PI, PET and Al as protecting layer. In order to realize these measurements, first a 30nm thick electrode of gold was deposited on both sides of the LDPE films, as mentioned in section 2.2.3. Moreover, in order to investigate whether the nature of the electrode plays a role in the space charge accumulation phenomenon, samples have also been realized with 50 µm-thick semicon as electrode layer, as mentioned in 2.2.4, to emulate the HV cable structure. In this way, it has been possible not only to understand the impact of the protecting layer used during sample preparation, but also the importance of the electrode-LDPE film interface. The measurements have been performed by applying a DC stress using charging and discharging times of 3h/3h. During the charging time intervals, the field has been set to the values of 10, 20, 30 and -30 kV/mm.

3.3.1 Space charge patterns with different protecting layers

Figure 3-16 shows the evolution of the space charge distribution profiles over the time for LDPE processed with PET protective layer.

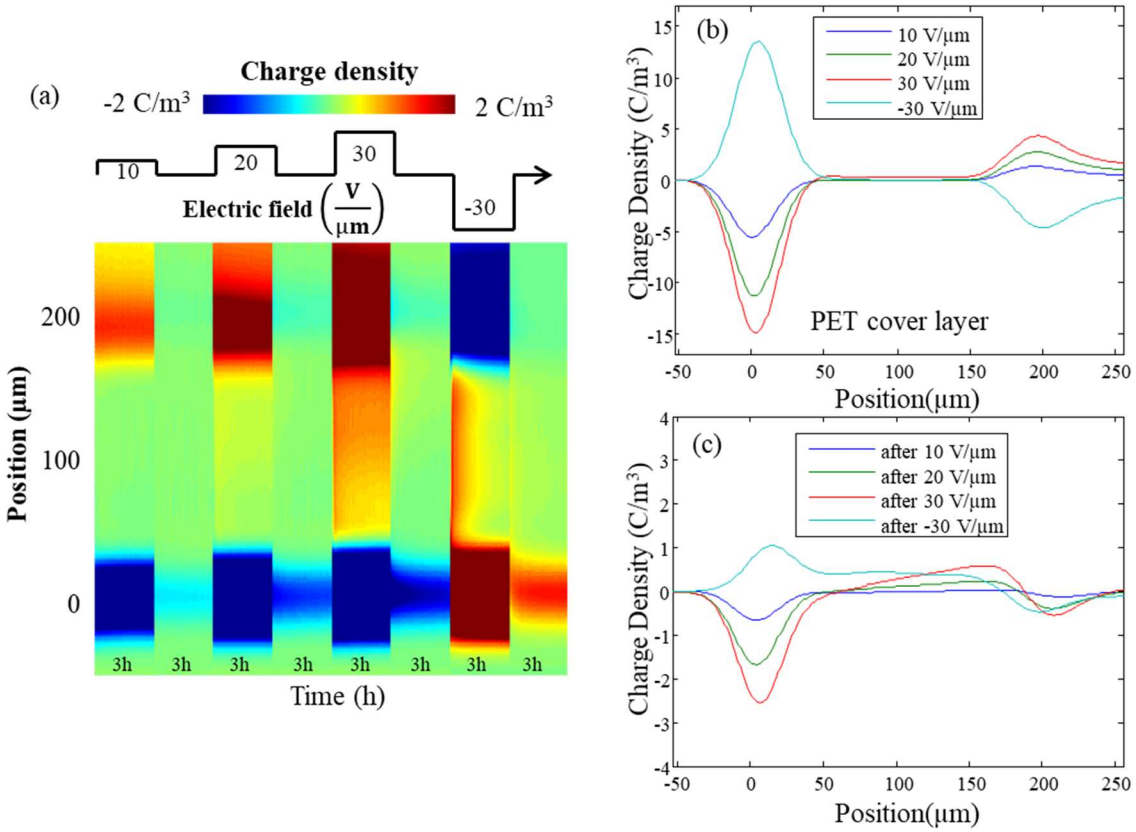

Figure 3-16 Space charge profiles obtained with LDPE realized with a PET protecting layer. (a) color map of the time dependence of the profile along the cycle; (b) charge density profiles just after voltage application c) charge profiles just after voltage removal.

In Figure 3-16a, it is possible to observe the space charge distribution variations, which correspond to the different charging-discharging time, each one with a duration of three hours. For the first three charging periods the anode corresponds to the top of the image while the bottom electrode represents the cathode. For the last charging time the polarity has been inverted. More intense charge density regions on the top and bottom part of the figure (red and blue ones) correspond to the polarization charge build up at the interfaces between each electrode layer and the LDPE film. This can be better appreciated considering the profiles shown in Figure 3-16b. Note here that the influence charge on the top electrode is underestimated presumably due to bad acoustic coupling with the top semiconducting electrode. Moreover, the graph in Figure 3-16b shows the charge profiles vs the spatial coordinate across the sample, evaluated immediately after the application of the external electric field and for each value of the electric field. The position 0 μm is assumed in correspondence of the peak related to the electrode/insulator interface closer to the piezoelectric sensor which measures the acoustic waves generated by the charge displacement in the insulator.

It can be noticed that for each values of the applied electric field, the signals at 0 μm is between 55% and 75% more intense with respect to the signals at the interface with the opposite electrode. This can be explained by two contributions: the first one is related to the fact that the signal generated at the interface far from the sensor may be dispersed and attenuated before being detected; the second one is represented by the destructive interference with the signal reflected from the metallic electrode – i.e. bad acoustic matching with the top semicon electrode of the PEA cell. To avoid the introduction of additional artifacts due to the data treatment, here only the deconvolution method, verified by Vissouvanadin [Viss11] on this setup, has been applied on the raw data. The charge density at the interface increases linearly with the electric field until, at high values of the electric field, a space charge builds up in the volume inducing the formation of an opposite image charge at the interface and interrupting the linear behavior.

We notice that the dominating charge in the volume of the insulator is positive, injected from the positive electrode and spreading into the insulation. The residual charge in the bulk of the insulator recorded just after voltage removal is shown in Figure 3-16c. At polarity reversal, positive charges dominate at short time and are progressively replaced or partly counterbalanced by negative charges in such a way that a low amount of charges remains in the final volt-off step. In this case, symmetric patterns are obtained with homocharges near both electrodes. Finally, we can also note that, whatever the sign of the electric field, a persisting homocharge is present at the bottom interface during the discharging time. This fact is probably related to the experimental setup.

Very similar qualitative features are observed in the LDPE films prepared using PI and Al with the only difference the net positive charge is more intense, Figure 3-17 and Figure 3-18. Note that the scale in volts-off profiles is magnified in Figure 3-16 to better appreciate the shape of the profile. After polarity reversal the sign of the charge tends to change from positive to negative during the time. This is even clearer for the Al protecting layer. During stressing under positive voltage at 30kV/mm, positive charges are generated in the all insulation. The residual positive charge has as consequence to enhance the electric field to the top electrode under the negative voltage step. Because of this field strengthening, a burst of negative charge is injected from the top electrode. Therefore, we interpret the phenomenon of negative charge generation during the last step as a consequence of the previously stored positive charges.

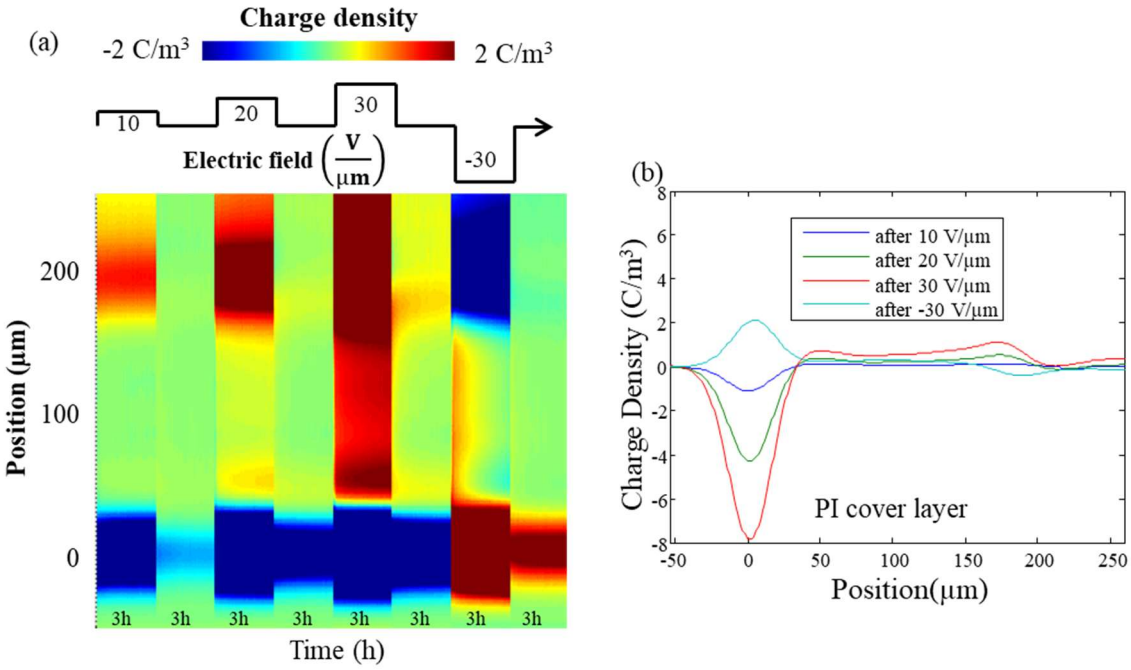

Figure 3-17 Space charge profiles obtained with LDPE realized with PI protecting layer. (a) colour map of time dependence of the profile along the cycle; (b) charge density profiles just after voltage removal.

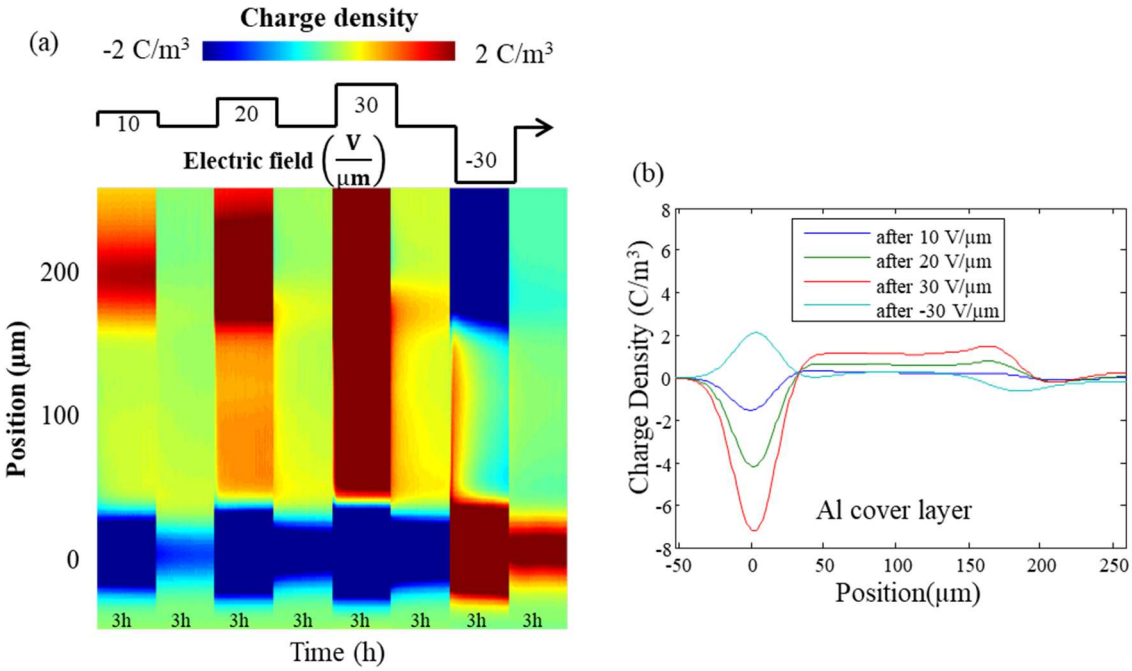

Figure 3-18 Space charge profiles obtained with LDPE realized with Al protecting layer. (a) colour map of time dependence of the profile along the cycle; (b) charge density profiles just after voltage removal.

Hence it can be inferred here, by comparing figures as it is depicted in Figure 3-16, Figure 3-17 and Figure 3-18, that changing the protecting layer does not affect qualitatively the behavior in terms of space charge accumulation. The amount of stored charges seems to grow when changing from PET to PI and to Al protecting layers. The stronger increase in stored charge density going from PET to

other protecting-layers could be related to the increase in surface roughness measured in the single layer topological analysis, cf. Table 3-2. The roughness would increase locally the field on the electrodes and would favor injection [Taleb09].

3.3.2 Kinetics of charge flow

Observing in detail the charge build up in the first ten minutes after the switch-on of the electric field we can notice that the positive charges progressively accumulate from the positive electrode spreading in the volume. This phenomenon is observed in all the samples with the deposited gold electrode from 10 V/µm of applied electric field, even if just above the noise threshold. In Figure 3-19 a series of profiles represents the time evolution of the charge density in the LDPE volume of a sample prepared using PET protecting layer under an applied electric field of 30 V/µm. A modest amount of charge, 0.2 C/m^3 persists from the previous charging periods and a further 0.8 C/m^3 is accumulated from the positive electrode in the first 10 minutes and is maintained almost the same state for the rest of the charging period.

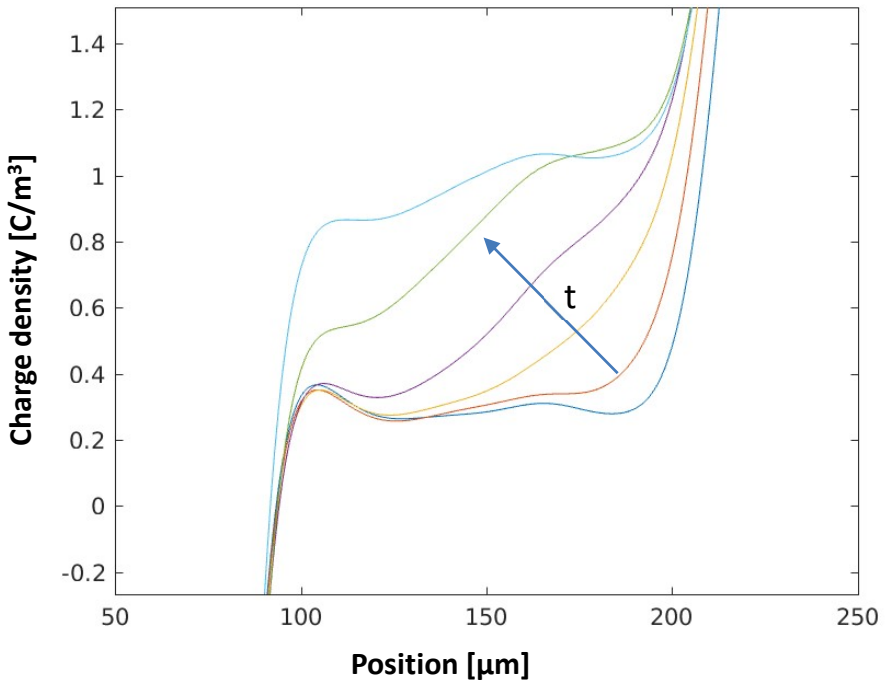

Figure 3-19 Selected charge profiles, during the first 10min of the step at 30V/µm, for LDPE realized with PET protective layer.

Subtracting the previous one from each profile it is possible to derive the variation in time across the sample profile of the charge density, cf. Figure 3-20. Considering the continuity equation:

$$\frac{\partial \rho(x,t)}{\partial t} = -\nabla \cdot j(x,t) \qquad 3\text{-}2$$

the time variation of the local charge density ρ is related to the spatial gradient of current density j (representing the unbalance between in-flow and out-flow of charges at a given position).

Supposing we are in the case of unipolar transport and diffusive current can be neglected, then:

$$\frac{\partial \rho(x,t)}{\partial t} = -\nabla \cdot (\rho(x,t)v(x,t)) = -\mu\nabla \cdot (\rho(x,t)E(x,t)). \qquad 3\text{-}2$$

Ahead the front of charges, the field is increased due to the space charge induced field. For this reason, the charge front is less and less steep as the front propagates. If there were an isolated charge front moving, the net charge under the differential profiles would be null. Here as charges are continuously provided at the anode, the net differential charge to the back of the front is slightly negative. Both processes of velocity increase at the head and charge provision to the back lead to a broadening of the differential charge profile. By monitoring the position of the peak in differential charge density profiles of Figure 3-20, we could estimate a velocity for the charges front, in a clearer way than can be done considering only the profiles, Figure 3-19.

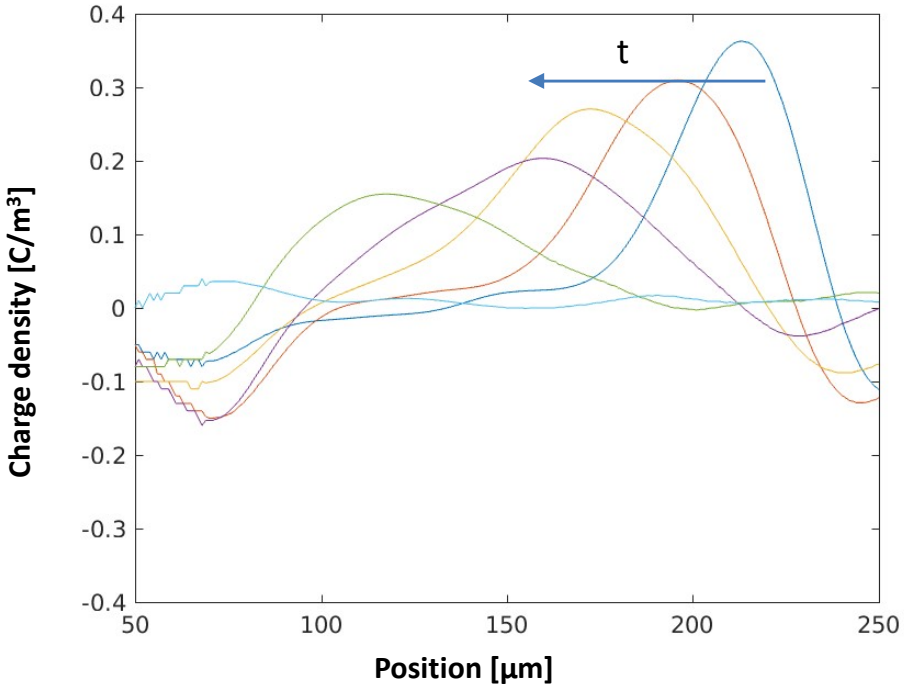

Figure 3-20 Difference between consecutive charge profiles obtained in 1 min intervals during the first 10min of the step at 30V/µm, for LDPE realized with PET protective layer

Indeed, from Figure 3-20 is clear how the front of charges moves through the insulating layer in a minute. Analysing the peak maximum displacement of all samples prepared with different protecting layers, cf. Table 3-3, it can be concluded that the speed of positive charge front propagation is not evidently dependent on the processing condition (for Au-metallized film). This is an expected behaviour as the surface conditions should not change substantially the propagation in the bulk insofar as the nature of carriers is the same. For the case of SC/PE/SC structures, which exhibit bipolar charging (see below), the trend is obviously not the same (cf. last column of Table 3-3) as the net charge is the result of propagating positive and negative charge fronts. Consequently, the apparent velocity is smaller, and the analysis leads to a different result. The velocity, for gold-metallized films is about 0.30 µm/s and the scatter does not allow evidencing the field dependence of speed. For an average field of 20kV/mm, the mobility would be of the order of 1.5×10^{-14} m²/V/s, which is consistent

with literature reports, being in between that reported by C. Thomas *et al* [Thom11] on another LDPE, as determined based on charge front propagation (1.2×10^{-14} m²/V/s) and the value (2×10^{-13} m²/V/s) used in charge transport models and based on fitting to space charge and current measurements [LeRoy06].

Electrode	**Gold**			**Semicon**
Protecting layer	PET	PI	Al	PI
Electric Field [kV/mm]	Speed charge density front [µm/s]			
10	-	0.15	0.25	-
20	0.33	0.42	0.22	-
30	0.31	0.33	0.23	0.11
-30	0.38	0.35	0.32	0.10

Table 3-3 Peak maximum displacement of all samples prepared with different protecting layer and different electric field.

3.3.3 Space charge in SC/PE/SC structures

Finally, in order to consider a more realistic case, the space charge distribution measurements have been performed on LDPE samples provided with semicon as 40 µm-thick electrode layers on both sides of the LDPE film, which is more like the real HV cable design, Figure 3-21. The film was processed using PI protecting layer. Compared to the samples realized with gold electrodes in Figure 3-17, the amplitude of the influence charge peak slightly differs from its opposite value (-17.4 C/m^3 for an applied electric field of 30 V/µm and 17.6 C/m^3 for the inverted polarity, Figure 3-21b). More importantly, the charge density measured at the interface on the top electrode is much less attenuated. The semicon electrode improves sensibly the transmission of sound through the sample avoiding reflections of the signal that destructively interfere by attenuating the response. The attenuation of the signal in the second electrode is between 15%-20%. Referring to the volts-off profiles, Figure 3-21b, the space charge accumulation in the LDPE volume appears to be substantially higher than in the previous cases. Also, the profile tends to be symmetric for positive and negative charges while positive charges dominated in case of gold electrodes. It is well known that the semicon is much more injecting for negative charges than a gold electrode can be [Mill16]. This explains the bipolar nature of charging. The coexistence of positive and negative charge clouds accounts for the apparent slower propagation velocity of charge clouds.

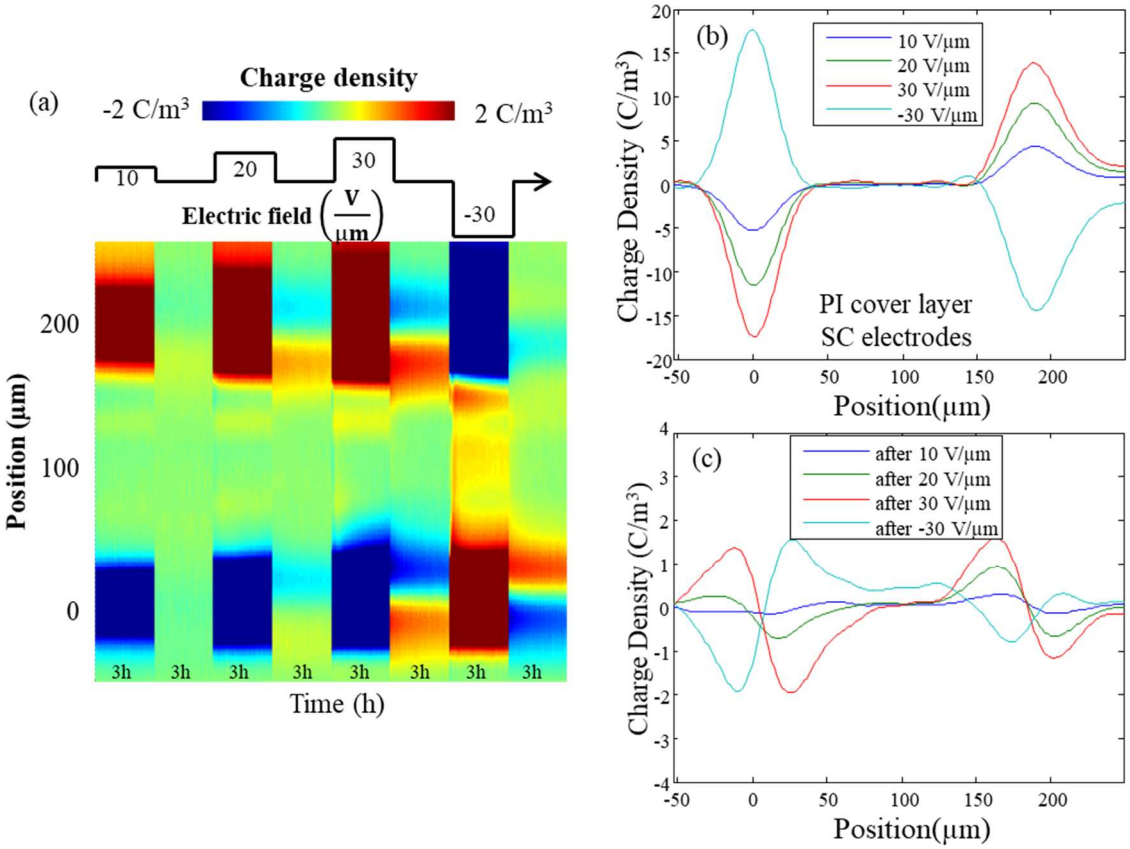

Figure 3-21 Space charge profiles obtained with LDPE realized with PI protecting layer and then provided with 40µm thick semicon electrodes on both sides (a) colour map of time dependence of the profile along the cycle; (b) charge density profiles just after voltage application c) charge profiles just after voltage removal.

The space charge profile obtained in volts-off after polarization under 30kV/mm is shown in some more detail in Figure 3-22. A volt-on profile is added for comparison. This is to highlight here the proximity of positive and negative charge fronts, and presumably the coexistence of the two types of carriers in the middle of the insulation. On the electrode, we can see that the net charge profile is the superposition of the image charge cloud, which in principle has the same shape as the capacitive charge peak in the volts-on profile, since both constitute influence charges. Because of the superposition of the internal space charge and influence charge clouds, and of the limited resolution of the technique, the charge densities in the both contributions are clearly underestimated. Comparing these results to those obtained with gold, it appears that the charge distribution, hence the interface field, are in an evident way dependent upon the electrodes used. The variation in space charge response is by far much more dependent on the nature of the electrode than on chemical or topological features at the surface. This is such at least when viewed from a semi-macroscopic point of view. In chapter 4 we present an investigation of these aspects at a microscopic scale. It remains therefore a great challenge to develop universal models of charge transport with realistic model of interface adapted to different nature of materials.

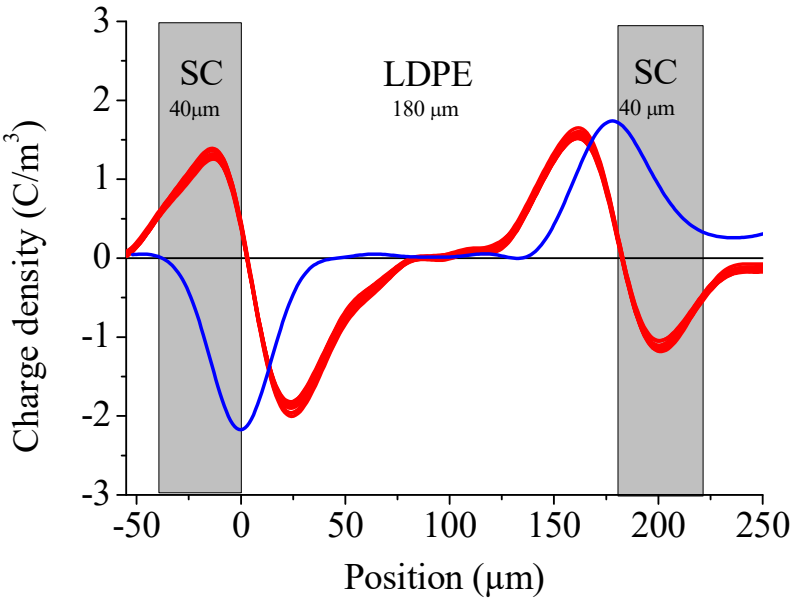

Figure 3-22 Volt-off profile obtained after the polarization step at +30kV/mm. In blue: volt-on profile (with arbitrary density scale) representing the response of capacitive charges

3.4 Polarization Current Measurements

For conductivity measurements, gold electrodes of 50 mm diameter and 30 nm thickness were deposited by sputtering. Measurements were achieved in air, at 25 or 50°C, using charging and discharging times of 3 h each. The sample holder was provided with a circulating fluid whose temperature was regulated by a thermo-cryostat. Hence the temperature was rigorously the same all along the experiments. Five field values in the range 5 to 30 kV/mm were applied consecutively to the same sample.

Figure 3-23 shows an example of charging and discharging current obtained at 25°C for a field of 20 kV/mm. The current measured in the depolarization stage is relatively noisy owing to the fact that the measurements were done with the DC supply regulating at 0V for the purpose of realizing continuous measurements over several days (the entire cycle of 5 field values lasts for 30h). Physical grounding of the sample would lead to much smoother signal, with the same overall shape. The important point here is that after 1h in volt-off the discharge current is significantly lower than the charging current. If a contribution from orientation polarization (originating from dipoles) was present in the charging current transient, then it should be the same, with opposite sign, in the discharge step. The fact that the discharge current is relatively low implies that the transient in the charging step is probably due to processes other than dipoles orientation, such as charge build-up in the insulation. The second consequence is that we can reasonably assume that the charging current measured beyond 1h is representative of conduction current.

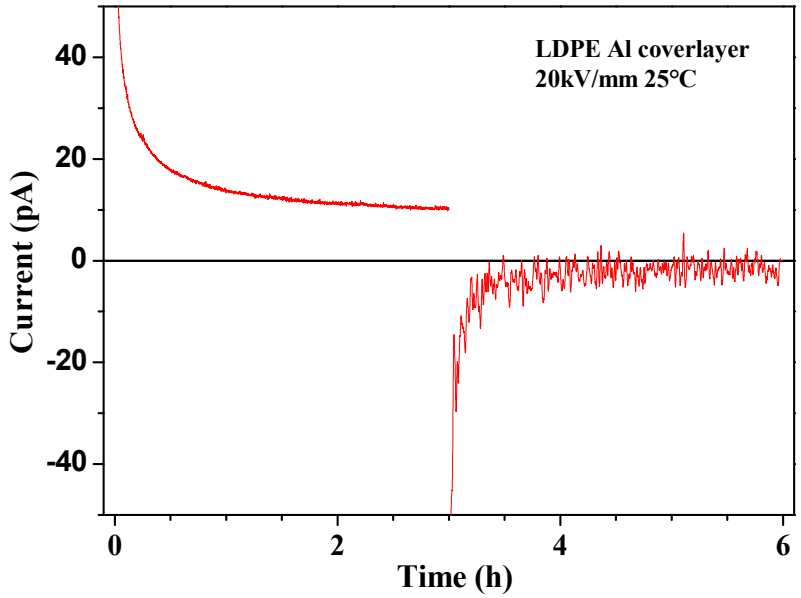

Figure 3-23 Charging and discharging currents measured for 3h under a field of 20kV/mm at 25°C. Sample is gold-metallized LDPE press-molded using Al protecting layer.

Figure 3-24 and Figure 3-25 show examples of transient charging currents recorded at room temperature for different fields and different materials. Qualitatively the transient currents for the different materials are very similar: in all cases, the current decreases with a slope less than 1 (in log-log scale) at short time (<100s), and then the decay slows down in the last decade in time. The approach to a nearly steady state at long time is more perceptible at the highest fields. For the lowest field of 5kV/mm, there is a wavier current decay, owing to the fact that steady state seems further in time.

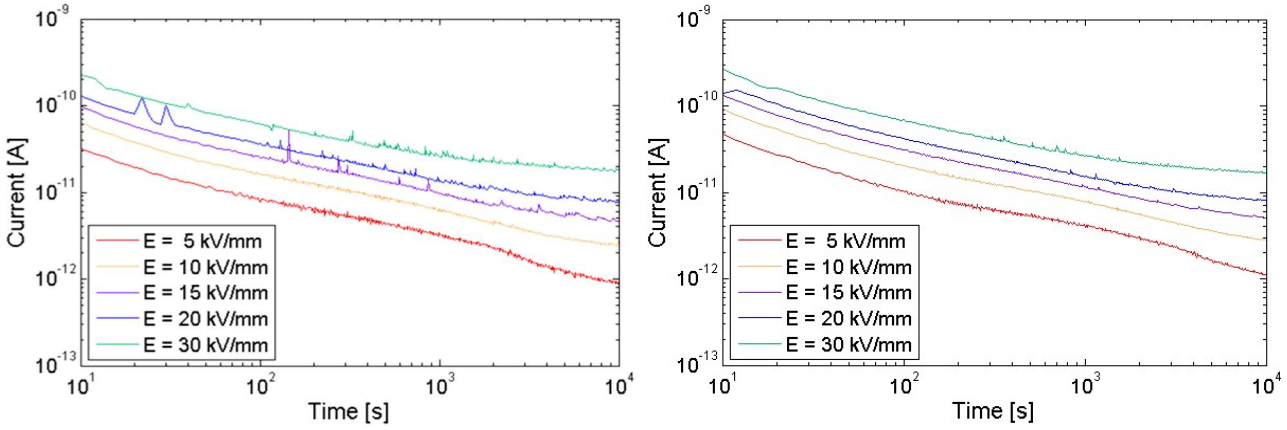

(a) PET protecting layer; Laplace process *(b) PET protecting layer, ABB process*

Figure 3-24 Charging current obtained at 25°C for different fields and different material processes.

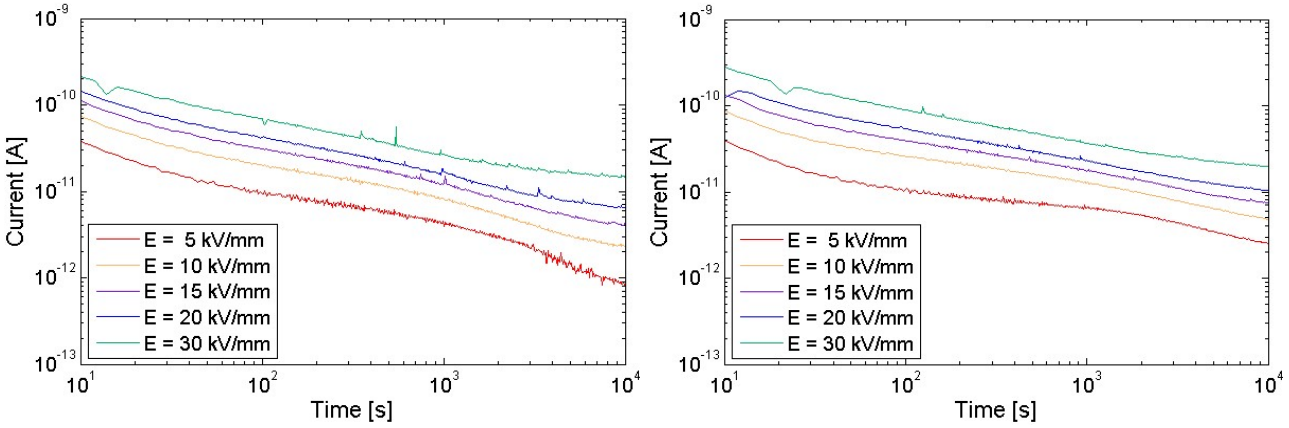

(c) PI protecting layer; Laplace process *(d) Al protecting layer; Laplace process*

Figure 3-25 Charging current obtained at 25°C for different fields and different material processes.

The current densities normalized to the field, i.e. j/E as 'transient' conductivities measured on a sample realized with PI protecting layer are shown in Figure 3-26 for the temperatures of 25 and 50°C. At 25°C, the normalized currents are perfectly superimposed over the first two decades in time. At long time, it tends to increase with the field featuring apparently non-linear conductivity. Considering data at 50°C, the normalized current appears higher for the lowest field value of 5 kV/mm. Then, it does not change with the field before increasing again for the step at 30 kV/mm. The feature possibly reflects previous observations by Ghorbani et al. on the long-term decrease in conductivity when polyethylene was stored continuously at 50°C for several months [Ghor16b] [Ghor17]. The decrease in conductivity was observed, whether or not the sample was put under DC stress. Therefore, it seems to correspond to a thermal conditioning of the material, with possibly slow structural evolution due to the temperature.

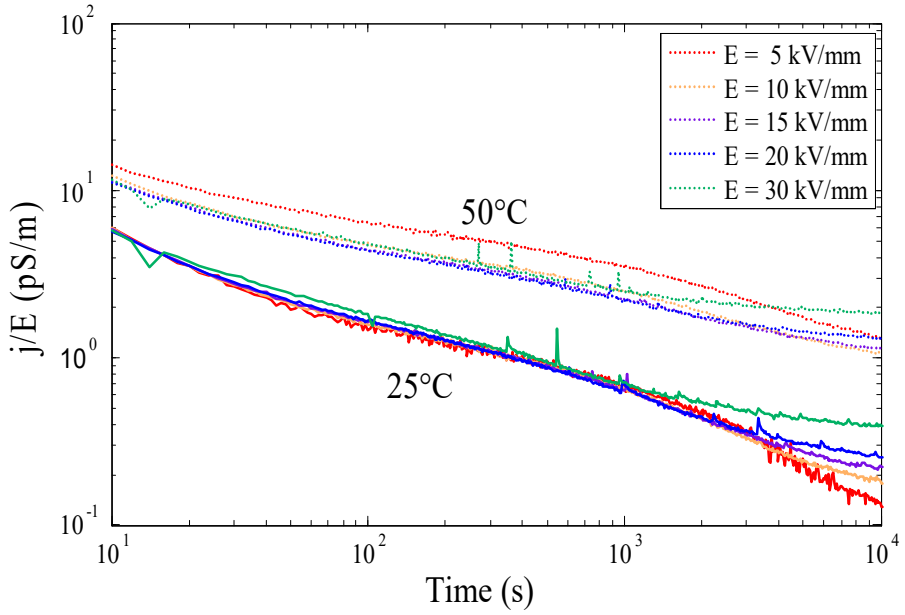

Figure 3-26; Normalized current transients obtained on LDPE processed with PI protecting layers.

The relatively higher normalized current obtained here for the first 3h at 50°C (plus possibly the discharging time) may correspond to this form of conditioning. Another noticeable information is the increase in apparent conductivity, by a factor of about 5 when increasing the temperature from 25 to 50°C. The slope of the transient current is clearly less at 50°C compared to 25°C.

Let us consider now how the conductivity evolves with the processing conditions. Figure 3-27 compares the conductivity vs. field characteristics as a function of the applied field, at room temperature. It can be seen that the conductivity for a given field span in a range 1÷3 depending on sample. However, the variation is not correlated in an evident way to the processing condition of the films. Samples processed with PI protecting layer for example are to the top and to the bottom of the plot. The same trend holds for data at 50°C. At the present stage one cannot argue on a possible effect of the press-molding condition on external current.

Clearly, in all cases the normalized current increases with the field featuring nonlinear conductivity beyond a field of 15kV/mm or less. The behavior appears in agreement with literature on the topic [Mont00].

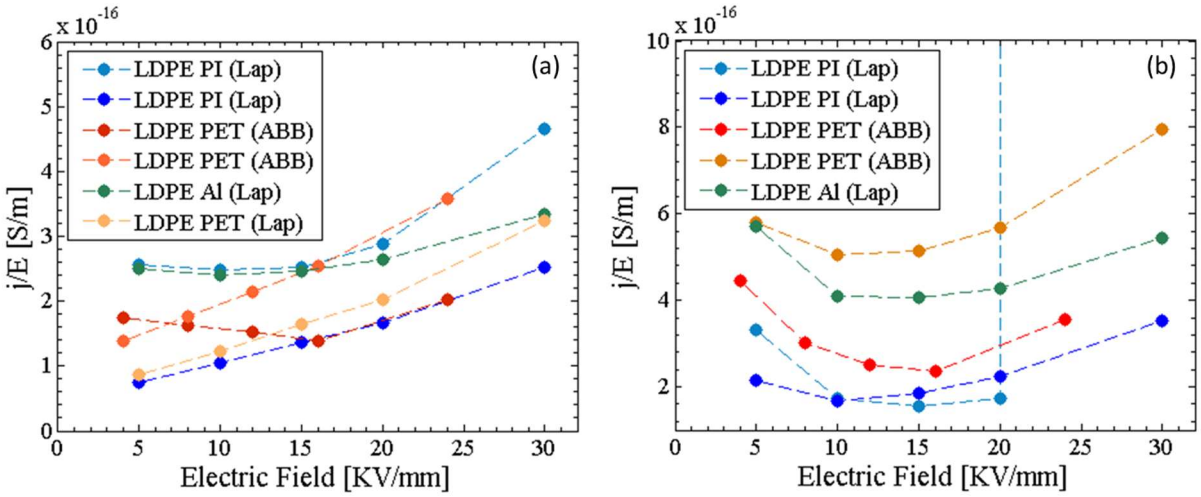

Figure 3-27 Apparent conductivity vs. field at 25°C (a) and 50°C (b) for film processed with different protecting layers processed in ABB and Laplace sites.

3.5 Synthesis: the impact of the press molding process on the macroscopic response

In this Chapter, we have evaluated the differences in chemical, structural and electrical properties that may arise from the use of different protecting layers when press-molding polyethylene. This is an essential step before coming into more detailed on the electronic properties of the interfaces.

In terms of methodology for insulation investigation, in particular surface investigation, we have proposed a roughness analysis based on image processing with increasing size in order to reveal features at specific scales. In space charge measurements, we proposed to use differential charge density profiles to evaluate the propagation speed of charge fronts and then apparent charge mobility.

The salient results obtained in this study are provided in Table 3-4. It provides a sum-up of the features identified as a function of the protecting layer. A clear feature of the results reported here is the observation of specific signature by PL and IR for the sample processed with PET protecting layers. In FTIR the response is characteristic of oxidized groups. In PL, a fluorescence band at 390 nm, which is not characteristic of LDPE known defects, is clearly identified. This band was detected in the PL spectrum of the PET protecting layers. The extra-signatures were therefore attributed to diffusion of oxidized groups –presumably decomposition products or oligomer chains from PET into the LDPE surface.

In terms of roughness, a direct impact of the protecting layer could be identified, with a clearly smoother surface using the PET protecting layer. The average roughness of the different samples differs: it changes from about 150 nm using PI or Al as press-molding layers to 33 nm using PET foils.

Protecting layer	Roughness	Fluorescence	FTIR	PEA	I(t)
Al	Rough	—	—	More space charge	Similar
PI	Rough	—	—		
PET	Smooth	Oxidized groups/PET	C=O and C-O groups	Less space charge	

TABLE 3-4 Sum-up of the impact of the protecting layer on structural and electrical properties.

The different press-molding conditions did not reveal substantial changes in the apparent conductivity of the materials. According to previous work by Taleb et al. [Taleb09] the injection current should be theoretically substantially dependent on the surface profile supposing thermionic emission: this is related to the field intensification and the non-linear field dependence of the injection current. This was reported for much more coarse structures, with roughness scale of the order of µm, and higher fields than investigated here (>30 kV/mm). Here the scattering of conductivity data did not allow making a reliable comparison.

The trend for the space charge results is an increase of the space charge amount with coarsening the structure. The situation is that of homocharges, lowering the electrode field. Possibly the trapped charge compensates field enhancement due to the roughness in such a way that the current does not change in a great extent. Besides, the sputtering process of gold electrodes, though achieved avoiding sample heating, possibly acts on the chemical state of the surface and in some way smooths the difference in injection efficiency that could appear in relation to oxidized groups. Present results on conductivity are clearly not consistent with those of Ghorbani et al. [Ghor16b] [Ghor17] who found a substantial difference in the measured conductivity as a function of the press-molding layer. The main difference with the present measurements concern the kind of electrodes used, i.e. massive brass electrodes. There is possibly the formation of small gaps between the electrode and the film surface when sputtered electrodes are deposited conforming to the film surface.

Finally, we obtained significant differences in space charge features with interposing semiconducting electrodes. The results indicate that, at the micrometer scale of the measurements, the nature of electrode is more influential on the apparent dielectric behavior than the surface features of the samples.

Chapter 4
Semicon / LDPE interface properties

4.1 Introduction

The objective of this chapter is to characterize the interface between semicon and LDPE from physical and electrical points of view. To reach this goal semicon/LDPE/semicon sandwiches will be used. As described in the chapter 2, these sandwiches were cut by ultra-cryo-microtomy to reach the interface. This interface will be characterized using PF-QNM and KPFM to attempt to determine the morphology and electrical properties. To try to interpret surface potential measurement a method is proposed to extract total charge density.

4.2 Physical characterization of the Semicon/LDPE interface

Every SC/LDPE/SC sandwich was investigated in cross-section using Scanning Electron Microscopy (SEM) and PF-QNM. Figure 4-1 summarizes results obtained for LDPE processed using PI protecting layer. The SEM picture shows a quite abrupt interface demonstrating no carbon black nanoparticles moving in the matrix hence no apparent concentration gradient between the two layers. This result was confirmed by PF-QNM measurement in topography (Figure 4-1b) or adhesion (Figure 4-1c). The physical interface appears abrupt with a certain roughness. Moreover, the difference in adhesion force in observed in the SC between LDPE matrix and carbon black nanoparticles it has been very useful for establishing the contrast between the two materials.

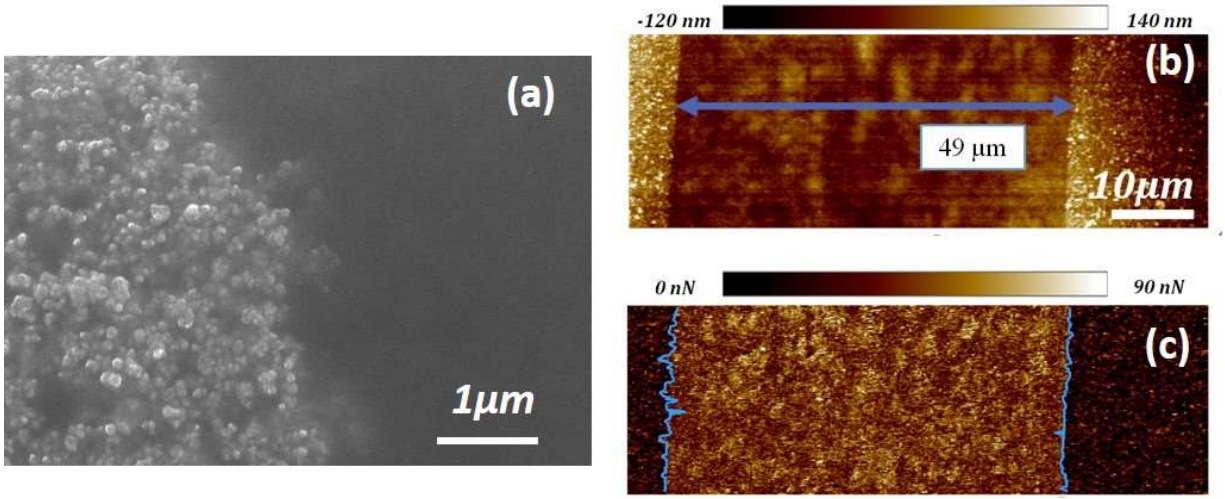

Figure 4-1 (a) Scanning Electron Microscopy (SEM) in Secondary Electron picture of Semicon/LDPE interface. (b) Topography and (c) adhesion map measured in PF-QNM of Semicon/LDPE/Semicon sandwich. LDPE was processed using PI protecting *layer.*

Quite the same results were obtained whatever LDPE process (temperature/pressure profile and protecting layer). Indeed, as shown on Figure 4-2 with adhesion map, the physical interface appears abrupt traducing no mixing between SC and LDPE.

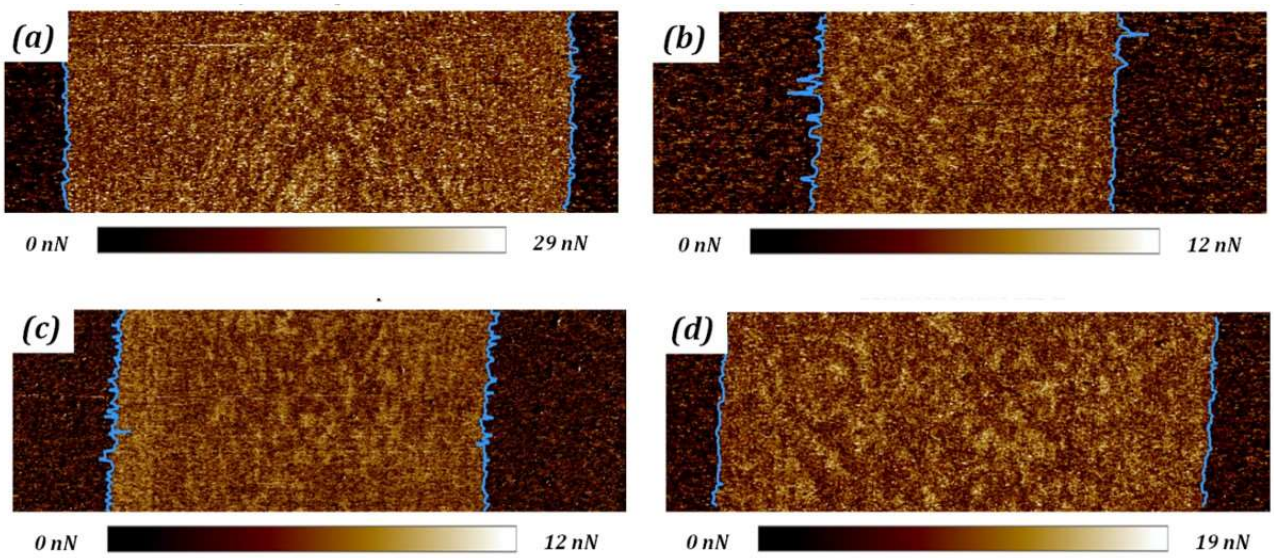

Figure 4-2 (a) Adhesion map measured in PF-QNM for Semicon/LDPE/Semicon sandwich whose LDPE is processed in Laplace using (a) PET or (b) Al protecting *layer or processed in ABB using (c) PET or (d) Al* protecting *layer.*

To identify the influence of protecting layer on the physical properties of the interface, the interface roughness was determined using the protocol described on Figure 4-3a. The first step consists in determining a reference which is LDPE adhesion. This reference corresponds to the adhesion mean value in reference surface and its standard deviation Σ, calculated in the red square on Figure 4-3b. Then the adhesion force on each point from right to left of the picture is compared to this reference. If the difference is lower than 5 Σ it is considered that this point does not belong to the interface and the following point is tested. When the difference is higher than 5 Σ the point is considered as interface. The deduced interface profile is represented in blue on Figure 4-2 and Figure 4-3b.

Results highlight that the process temperature/pressure has no influence on interface roughness whereas the nature of protecting layer strongly influences this parameter. Quantities related to the interface roughness are summarized in Table 4-1. The LDPE film processed with Al and PI protecting layers exhibit higher interface roughness which is consistent with our initial surface roughness conditions established before sandwich processing (cf. figure 3-10).

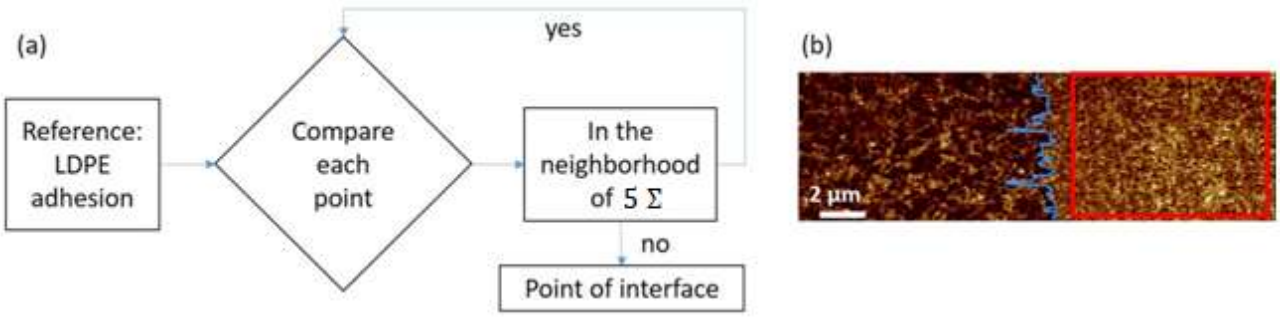

Figure 4-3 Algorithm for the interface profile determination.

Protecting layer	LDPE width	Interface roughness	Standard deviation
PI	47.8µm	480nm	2%
Al	42.6µm	525nm	2.5%
PET	57.6µm	265nm	0.9%

Table 4-1 Physical properties of Semicon/LDPE interface.

4.3 Electrical characterization of Semicon/LDPE interface

4.3.1 Process influence on Semicon/LDPE surface potential distribution

As shown previously, the physical interface between semicon and LDPE is abrupt, and its roughness is influenced by the protecting layer used to process the LDPE. To identify the influence of this protecting layer on electrical properties at interface, surface potential measurements were performed on SC/LDPE/SC cross-section using PF-KPFM.

Figure 4-4 shows results obtains for sandwich whose LDPE was processed in Laplace using a PI protecting layer. Comparison of the two maps shows that even if the physical interface is abrupt, the surface potential decreases slowly going from SC to LDPE. This result is confirmed on Figure 4-4c which compares three scans measured on the same KPFM picture (the one depicted on Figure 4-4b). All scans exhibit the same shape and the potential levels are similar. The maximum potential difference between SC and LDPE is around -0.5V. Moreover, the potential variation is over a range of around 15µm. So, the 'electrical' interface appears smooth.

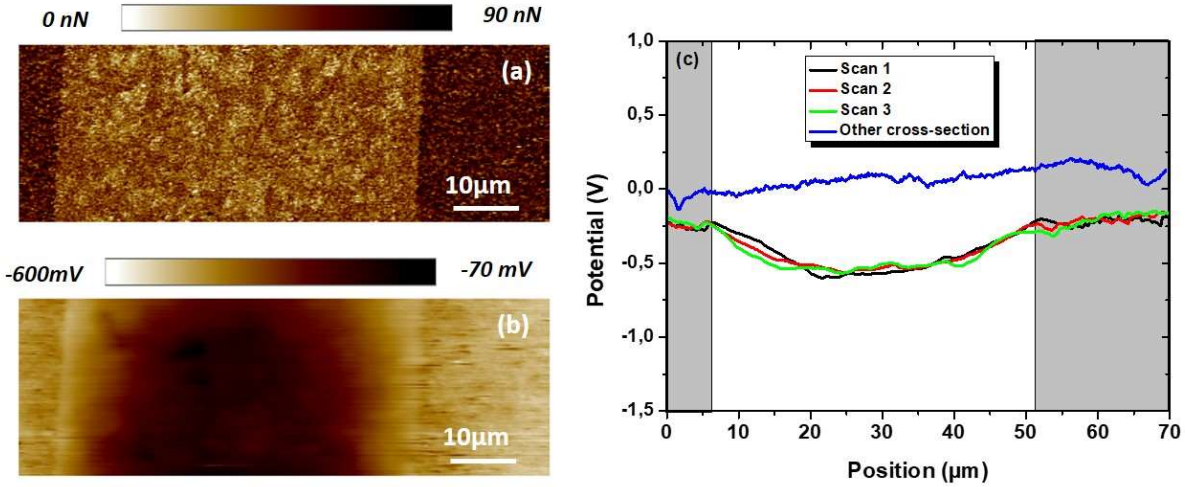

Figure 4-4 (a) Adhesion and (b) surface potential map measured by PF-QNM on sandwich whose LDPE was processed with PI protecting layer. (c) Comparison of surface potential profiles obtained in figure (b) and on another sample (same sandwich which was cut at different position). The grey area represents the SC.

To evaluate measurement reliability, another cross-section was prepared in another region of the same initial sandwich. The resulting surface potential profile is depicted on figure 4-4c over the label "other cross-section". This profile appears quite flat compared to the previous one, which is quite astonishing. This difference could be linked to sample properties heterogeneity, the influence of ambient condition (humidity, temperature …) which avoid the measurement of absolute surface potential [Nonn91] or a lack of measurement reliability. These two last ambient parameters, namely humidity and temperature, should influence all measurements in the same way whereas sample heterogeneity should depend on fabrication process. So before trying to interpret surface potential profile shape, the influence of LDPE process on surface potential profile will be investigated.

Figure *4-5* compares surface potential measurements for a sandwich whose LDPE was processed using an Al cover-layer. As previously and whatever the process, the surface potential slowly vary from interface to LDPE bulk to reach a maximum value. This varies substantially from one sample to another with the same process or with different processes. Indeed, for LDPE processed in Laplace with Al cover layer, the maximum potential value depends on the sample.

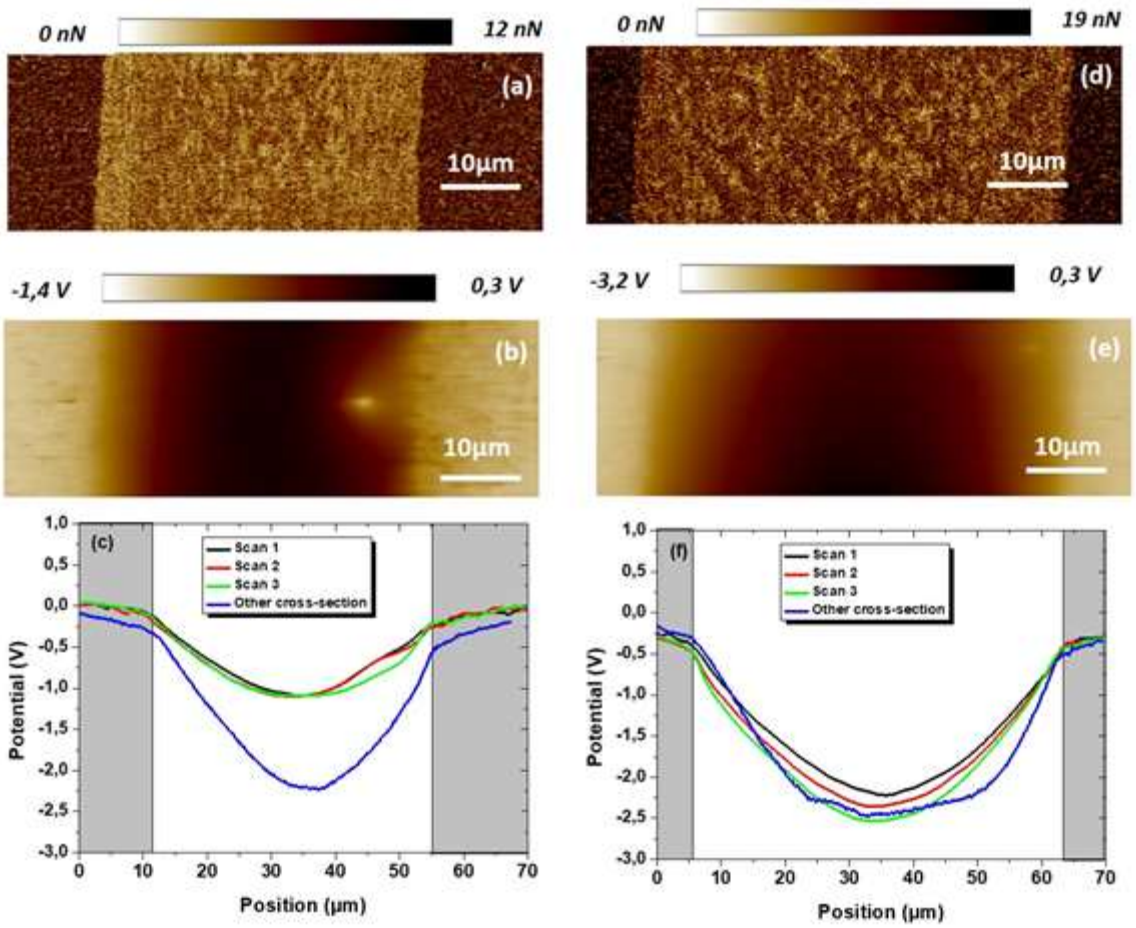

Figure 4-5 Comparison of (a; d) adhesion, (b; e) surface potential map and (c; f) surface potential profile for a sandwich whose LDPE was processed using Al in Laplace (left row) and ABB (right row). In figure (c) and (f) the grey areas represent SC and "other cross-section" corresponds to another sample (same sandwich which was cut in a different region).

Figure 4-6 compares surface potential profiles for sandwich whose LDPE was processed using a PET protecting -layer. As previously seen and whatever the process, the surface potential increases slowly from interface to LDPE bulk to reach a maximum value which is very different for samples and process. Indeed, for ABB and Laplace processes a huge difference is observed between to cross-sections obtained on the same sample.

The sample processed in ABB exhibits an anomalous behaviour because it is the only one for which maximum potential in LDPE bulk presents positive value. A noticeable difference between this sample and the other ones is its thickness, related to the sandwich processing. Indeed, this thickness is around 40µm whereas the other ones have thicknesses in the range 50-55µm. So, a sample of the same thickness should be processed to take appart possible thickness effect.

Regarding these results the common behaviour of all samples is to present a surface potential profile with a smooth transition between SC and LDPE which features a "bell-like" shape.

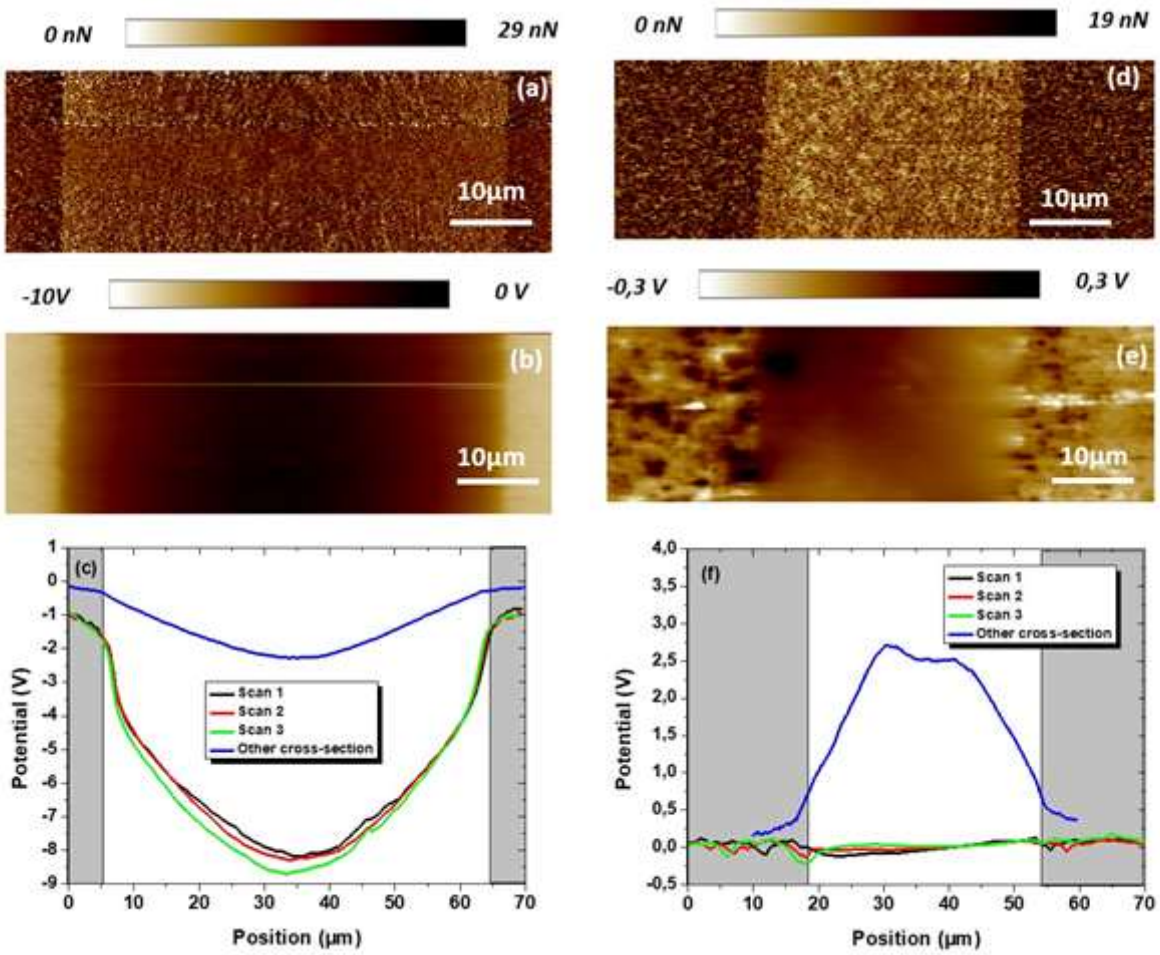

Figure 4-6 Comparison of (a; d) adhesion, (b; e) surface potential map and (c; f) surface potential profile for sandwich whose LDPE was processed using PET in Laplace (left row) and ABB (right row). In figure (c) and (f) grey areas represent SC and "other cross-section" corresponds to other sample (same sandwich which was cut at different position).

Table 4-2 summarizes the variation of surface potential difference between each material as function of process used for the LDPE. Due to the strong variation of surface potential maximum from one cross-section to another coming from the same sandwich, results interpretation is quite difficult. However, we can notice that the variation range is more important for the cross-section processed with PET protecting layer. This can be due to surface chemistry changes (cf. FTIR and PL results in section 3.1) which could be inhomogeneous over the surface, inducing differences between cross-sections coming from different sandwich areas. For the other protecting layers, the variation of the amplitude of the surface potential step is smaller. It seems to be smaller for the sample processed with PI protecting layer than with Al one. So, due to these variations, in the following we will focus on the interpretation of surface potential profile shape rather than on amplitude of the surface potential step. Our aim is to identify the origin of this shape which was already observed for Au/LDPE sandwich [Leroy16] or PEO/Al [Fali17].

Process	Laplace			ABB	
Protecting layer	PI	PET	Al	PET	Al
Range of surface potential step (V)	From 0V to -0.5V	From -2V to -8V	From -1V to -2V	From 0V to +2.5V	From -2V to -2.5V

Table 4-2 Comparison of maximum potential differences between semicon and LDPE as a function of LDPE process. A range is given to consider measurement reproducibility between different cross-sections on the same sample.

4.3.2 Interface properties: origins of differences

Before discussing the origin of the surface potential profile shape, a quick recall about the physical signification of this profile is needed. Figure 4-7a compares energy level of LDPE Conduction (BC) and Valence (BV) bands to surface potential of semicon whose value is unknown. Consequently, the surface potential profile should present a sharp variation of surface potential at SC/LDPE interface (Figure 4-7b) instead of this "bell-like" shape whose maximum vary independently from process. This smooth variation of surface potential may have different origins.

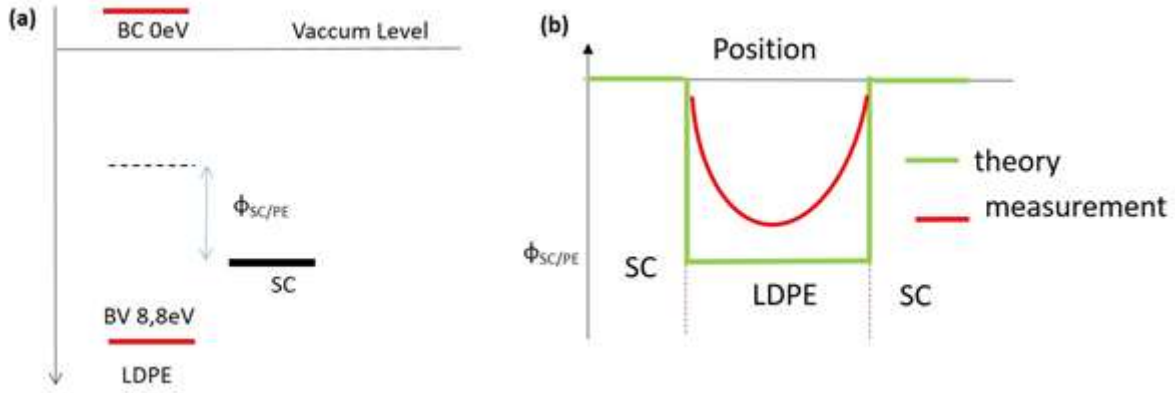

Figure 4-7 (a) Relative position of LDPE conduction (BC) and Valence (BV) bands compared to Semicon (SC) energy level. (b) Surface potential profile scheme related to energy levels.

First of all, a smooth transition could be the consequence of KPFM spatial resolution resulting from parasitic capacitance between AFM probe cantilever and sample [Jaco98]. To identify the impact of KPFM spatial resolution in our experimental conditions, the surface potential profile was measured over reference sample composed by Au and Al electrode deposited over silicon. In this structure, the surface potential profile presents a sharp transition (2µm width) at Au/Si and Si/Al interface (Figure 4-8a) and the difference of Al and Au surface potential (1.1eV) corresponds to the difference between their work functions (Figure 4-8b). This shows that even if the surface potential absolute value is unattainable under ambient conditions, relative measurements are possible.

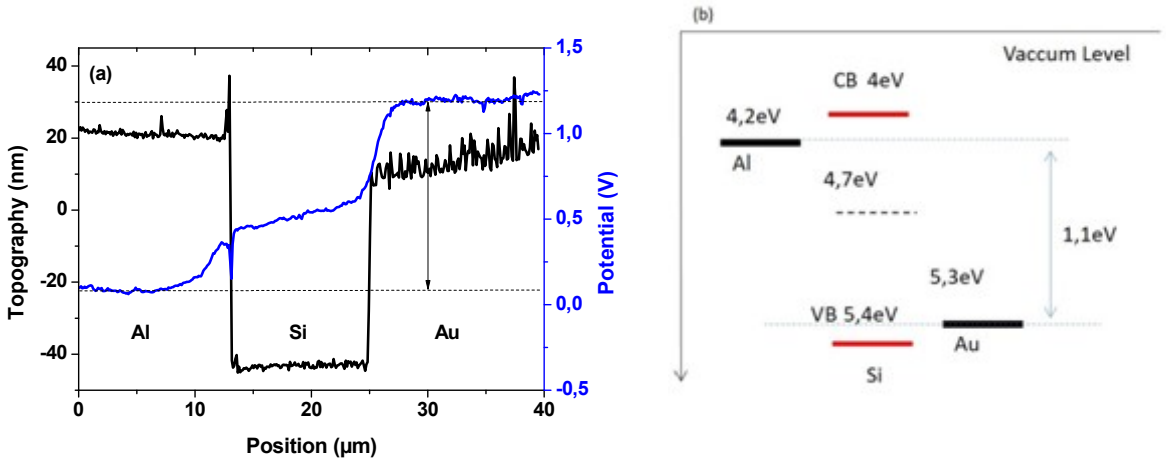

Figure 4-8 (a) topography and surface potential profile measured by KPFM on reference sample composed by Al and Au electrodes deposited on Si. (b) Comparison of Al and Au work function and Silicon Conduction (CB) and Valence (VB) Bands.

This kind of smooth interface was already observed in P-N junction [Dyms15] [Chen17]. In this case non-abrupt interface was attributed either to doping (i.e. electric charges) [Robi00] or material diffusion from one layer to another [Kryv16]. We can exclude the diffusion of carbon black particles in the SC/LDPE interface because the adhesion contrast in Figure 4-1 and Figure 4-2 is abrupt. This suggests that other sources of charges are involved in this phenomenon. In the following part a methodology to extract charge profile from surface potential measurement will be developed to confirm this hypothesis.

4.4 Interface charge quantification

This section is dedicated to the description of the mathematical approach used for the charges density quantification in LDPE layer close to interfaces. The numerical methods applied for the quantification of interface charges are then presented. It consists in a mathematical treatment of experimental surface potential profile followed by numerical computing of the charge density.

In the following, the 2-dimensional Savitzky-Golay (SG) filter will be used for the calculation of the surface potential and its impact on profile characteristics will be investigated.

4.4.1 Charges density extraction from surface potential measurements

To determine charge density ρ from the surface potential, we need to assume the fact that this potential reproduces the bulk potential. The validity of this hypothesis was demonstrated previously by Emmerich et al. [Emme16].

The charge density distribution and electric field $\vec{E}$ are determined from surface potential using the following equations:

$$\nabla^2\phi = -\frac{\rho}{\varepsilon_0} \qquad 4\text{-}1$$

$$\vec{E} = -\nabla\phi \qquad 4\text{-}2$$

Introducing polarization field $\vec{P}$ and the electric displacement field $\vec{D}$ these two equations could be expressed as:

$$\vec{\nabla}\cdot\vec{D} = \vec{\nabla}\cdot\left(\varepsilon_0\vec{E} + \vec{P}\right) = \rho_{free} \qquad 4\text{-}3$$

where ρ_{free} corresponds to the charge carrier density free to move in the volume.

The polarization $\vec{P}$ is related to electric field by the following relation

$$\vec{P} = \varepsilon_0 . \hat{\chi} \cdot \vec{E} \qquad 4\text{-}4$$

where $\hat{\chi}$ is the tensor of the electrical susceptibility.

In our configuration, due to interface between SC and LDPE, it is impossible to apply the isotropy condition. Consequently, a second approach has been proposed, which considers the charge density distribution as the sum of the components due to the free charge ρ_{free} and to the polarization charge ρ_{pol}. The later can be defined in the most general way as follows:

$$\rho_{pol} \equiv -\vec{\nabla}\cdot\ \vec{P} \qquad 4\text{-}5$$

Substituting the equation 4-5 in the 4-3

$$\nabla \cdot E = \frac{1}{\varepsilon_0}\left(\rho_{free} - \nabla \cdot P\right) = \frac{1}{\varepsilon_0}\left(\rho_{free} + \rho_{pol}\right) \qquad 4\text{-}6$$

This solution permits to calculate the total charge density distribution $\rho_{free}+\rho_{pol}$ in the interface region without further assumption about the polarization charge that cannot be easily correlated with the free charge.

4.4.2 Numerical methods for spatial charge calculation

As discussed in the previous paragraph, the electric field and the charge density distribution can be calculated as the first and second differential order of the surface potential using equation 4-2 and 4-6 respectively. We intend to apply this second derivative to KPFM surface potential map obtained in section 4-3-1 which consists in a matrix of numbers which represent the value of the surface potential in different points.

Four different methods have been implemented to calculate the first and second differential order of this matrix. Due to the symmetry of the sample, in order to simplify the calculation the derivative has been calculated only across the perpendicular direction of the interfaces. In order to make the different methods comparable, they have been defined in such a way as to use for the calculation of the second order derivative at most F consecutive data points, with $F \geq 3$.

- Method 1: Symmetric difference quotient

Considering one line of points, the derivative of the potential at the point (x_i, y_j) is calculated as the difference between surface potential at the point $\left(x_{i+\frac{F-1}{2}}, y_j\right)$ and (x_i, y_j) divided by an arbitrary distance of $\frac{F-1}{2}$ pixels between these two points:

$$\left.\frac{df}{dx}\right|_{(x_i,y_j)} = \frac{f\left(x_{i+\frac{F-1}{2}}, y_j\right) - f(x_i, y_i)}{\frac{F-1}{2}} \qquad 4\text{-}7$$

Using the Equation 4-7 on two consecutive points the second order derivative can be extracted as follows:

$$\left.\frac{d^2f}{dx^2}\right|_{(x_i,y_j)} = \frac{f\left(x_{i+F-1}, y_j\right) - 2f\left(x_{i+\frac{F-1}{2}}, y_j\right) + f\left(x_i, y_j\right)}{\left(\frac{F-1}{2}\right)^2} \qquad 4\text{-}8$$

This algorithm always uses the information from just three points along the x axis to calculate the second order derivative, the value of F increases the distance between these points reducing the impact of the high frequency noise.

- Method 2: Average of F neighbours

Another method to reduce the impact of the noise can be that of averaging F lines across the y direction, perpendicular to derivative direction.

This method uses the derivative function implemented in MATLAB which calculates the differences between adjacent elements. This method of averaging several similar profiles increases the signal-to-noise ratio using the symmetry of the sample.

- Method 3: Savitzky-Golay smoothing and differentiation filter 1D

The characteristic of this method is to fit by a polynomial curve of order O using the least squares method, in this case the third order, over F points of a single line. This method was developed as a smoothing method. With using the coefficient of the polynomial, the different derivative orders can be easily calculated. This method was previously used by Faliya et al. to extract charge density in PEO [Fali17].

- Method 4: Savitzky-Golay smoothing and differentiation filter 2D

Similarly, to the 1D version this method uses a polynomial fit, but in this case over a 2D patch area F×F around the point of coordinate (x_i, y_j), Figure 4-9a. For sake of simplification this method will be named SG-2D filter. A squared patch area permits to weight the result over more points close to (x_i, y_j) increasing the reliability of the calculation. As shown on Figure 4-9b, the algorithm especially implemented for this work consists of five steps.

The first step selects the image patch on the matrix (Figure 4-9a). The second step consists in fitting the profile at this point using the following polynomial:

$$f(x_i, y_j) = a_{00} + a_{10}x_i + a_{20}{x_i}^2 + a_{30}{x_i}^3 + a_{01}y_j + \\ + a_{02}{y_j}^2 + a_{03}{y_j}^3 + a_{11}x_i y_j + a_{21}{x_i}^2 y_j + a_{12}x_i {y_i}^2 \quad 4\text{-}9$$

The third one uses the evaluated polynomial coefficient to calculate the derivatives:

$$\frac{\partial f}{\partial x} = a_{10} + 2a_{20}x_i + a_{11}y_j + 3a_{30}{x_i}^2 + 2a_{21}x_i y_j + a_{12}{y_j}^2 \quad 4\text{-}10$$

$$\frac{\partial^2 f}{\partial x^2} = 2a_{20} + 6a_{30}x_i + 2a_{21}y_j \quad 4\text{-}11$$

Because we are interested in determining for each image patch the value of f, $\frac{\partial f}{\partial x}$ and $\frac{\partial^2 f}{\partial x^2}$ just in the center of coordinates (0,0) the Equations 4-9, 4-10 and 4-11 are simplified just to the calculation of the following coefficients: a_{00}, a_{10} and $2a_{20}$.

The forth step moves the image patch to scan the image and the last step is to evaluate the electric field and the charge density.

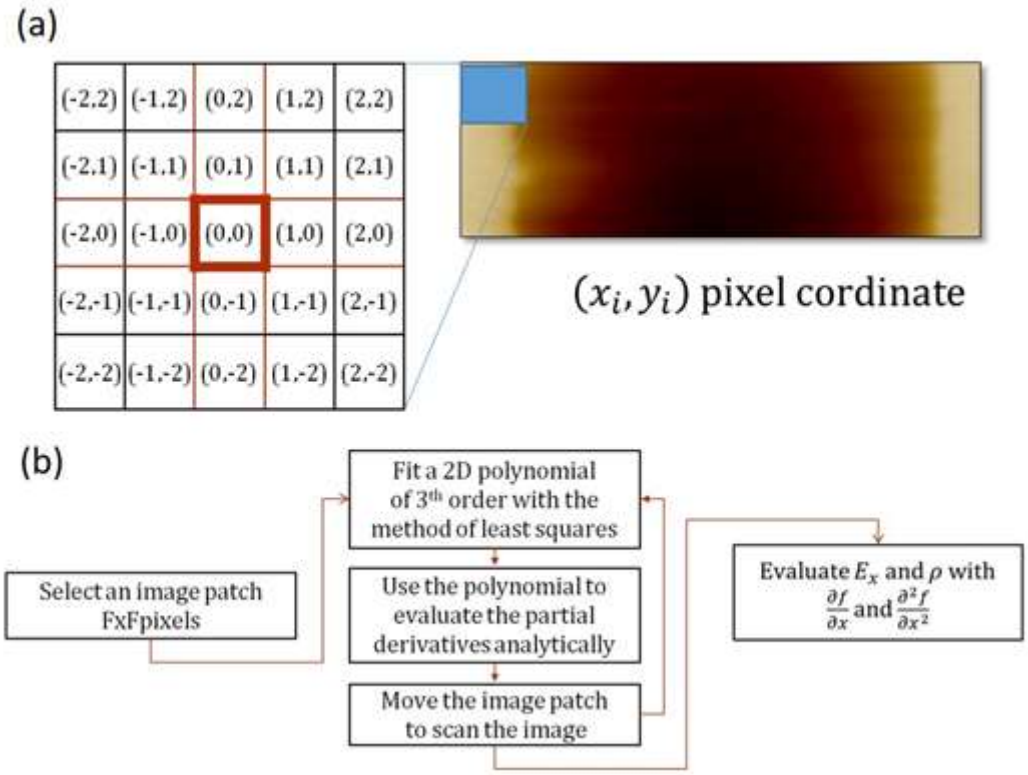

Figure 4-9 (a) Pixel definition and (b) algorithm scheme of SG 2D filter method.

These four methods are applied to surface potential profiles measured on sandwich structures made in Laplace using a PET cover layer (Figure 4-6a). In this configuration, the surface potential was measured using the PF-KPFM mode (best spatial resolution) with a single pixel resolution of about 136nm. The F parameter is equal to 9 for all the methods.

Results in terms of charge density profile are compared in Figure 4-10, highlighting that all methods provide comparable results. Close to each interface a negative charge density cloud is present in LDPE with corresponding positive image charges in the SC.

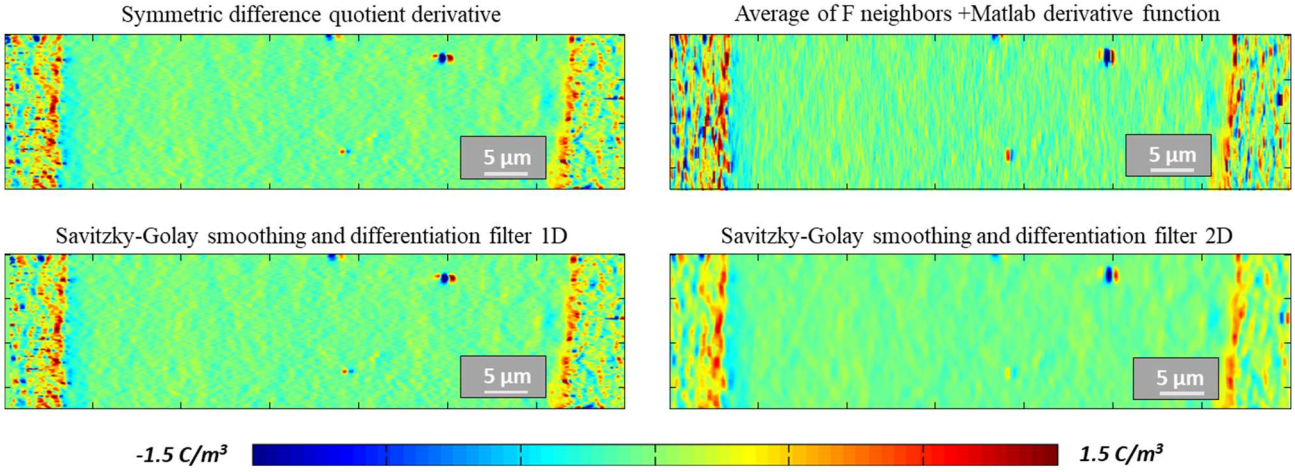

Figure 4-10 Comparison of charge density map obtained with four different methods applied on surface potential map measured on sandwich whose LDPE was processed in Laplace using PET cover layer. The surface potential was measured by PF-KPFM using 68nm-width pixel.

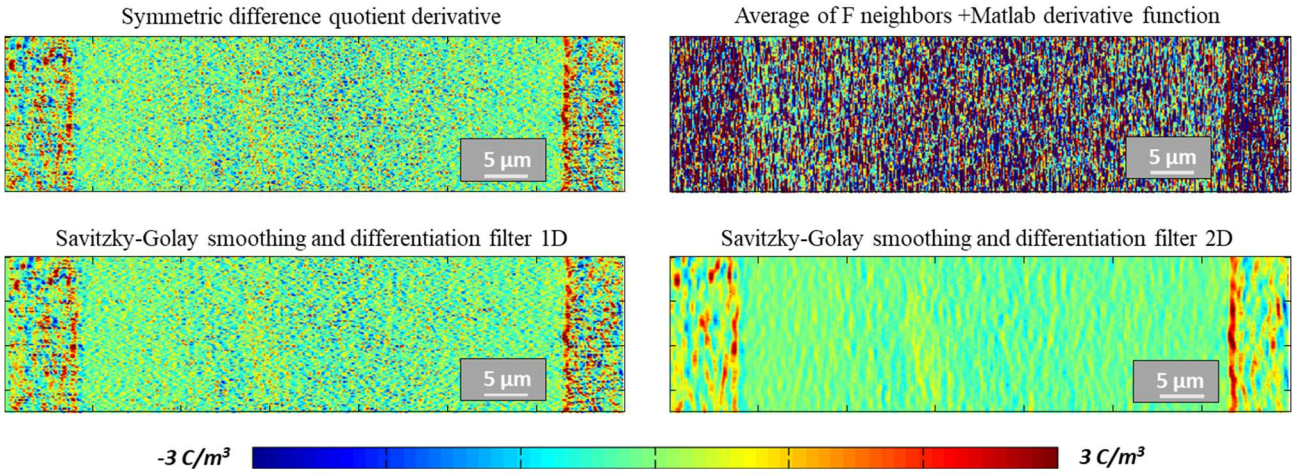

Figure 4-11 Comparison of charge density map obtained with four different methods applied on surface potential map measured on sandwich whose LDPE was processed in Laplace using PET cover layer. The surface potential was measured by AM-KPFM using 136nm-width pixel.

To emphasize the influence of the surface potential measurement condition, these four methods were equally applied on potential maps probed by AM-KPFM using a single pixel size of 136 nm. Figure 4-11 shows that due to the lower spatial sensibility of the AM-KPFM method, negative charges in LDPE are less detectable than with PF-KPFM. The method 2 termed "Average of F neighbours" appears noisier than the other methods.

To compensate the lower resolution and make comparable results, larger values of F must be considered. The SG-2D filter method, due to its 2D nature considers in its algorithm a higher density of points reducing the noise. It provides more reliable information.

These results also emphasize that the pixel size needs to be as small as possible to permit to extract accurately charge density profile from surface potential.

Figure 4-12 compares charge density profiles obtained with each method as function of pixel size. Whatever pixel size the Method 1 "symmetric difference quotient" is the noisiest one.

Whereas, when pixel size increases the most resilient method to the noise is the method 4 named Savitzky-Golay smoothing and differentiation 2D filter.

This method will be used in the following to extract charge density from surface potential measured.

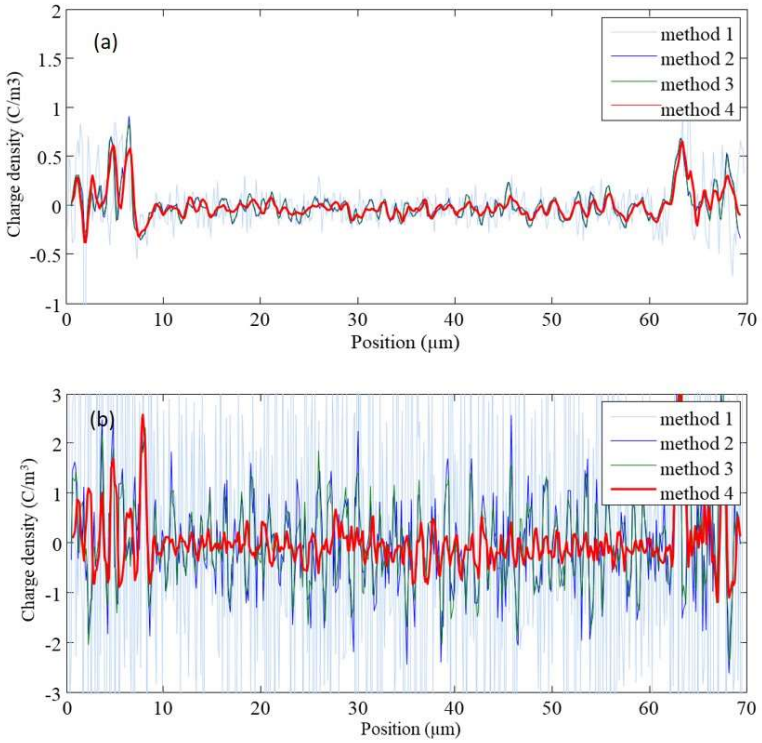

Figure 4-12 Comparison of charge density profile obtained with four different methods applied on surface potential map probed (a) by PF-KPFM using 68nm-width pixel and (b) by AM-KPFM using 136nm-width pixel.

To test the reliability of the SG 2D-filter method and quantify the effect of the filter in function of the image patch size, it has been applied on two matrices of data witch mimic two characteristic charge distributions defined by analytical functions. The first is a surface potential integrated from a Gaussian charge distribution with total charge normalized to 1, Figure 4-13a. The second surface potential corresponds to two Gaussian charge distributions of opposite signs placed at distance t, Figure 4-14a. Given the analytical form of these functions the result of the filter can be easily compared with its theoretical values. The effect of the filter became relevant when the standard deviation Σ_{theor} of the Gaussian distribution is under the patch image size. For broader distributions the filter manages to calculate the derivative with an excellent fidelity to the analytical value.

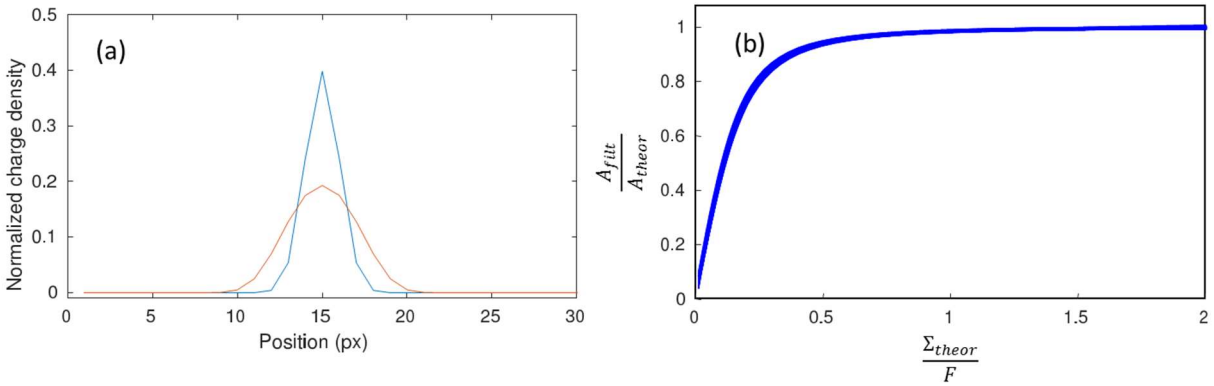

Figure 4-13 Effect of the SG-2D filter on a Gaussian charge density distribution. (a) filter effect on a normalized curve with Σ 1 px and patch image size 9 px. (b) amplitude damping trend compared to the theoretical value in function of sigma in unity of patch image size

The total charge for a single Gaussian distribution is not affected by the filter. Its effect is to spread the charges under the patch image size F, as shown in Figure 4-13a for a distribution with standard deviation $\Sigma = 1\ px$ and patch image size $F = 9\ px$. Normalized Gaussian curves have an inverse proportionality between amplitude and standard deviation. As appears in Figure 4-13a, the filtered amplitude is half that of the original and the standard deviation is doubled. The ratio between the filtered amplitude A_{filt} and its theoretical value saturates to 1 for standard deviation patch image size ratio $\Sigma_{theor}/F > 0.5$, and drops to 0 for lower values, Figure 4-13b.

Two Gaussian charge distributions, as studied for the second surface potential, Figure 4-14, have the characteristic to cancel each other when approaching a certain threshold distance and their tails overlap.

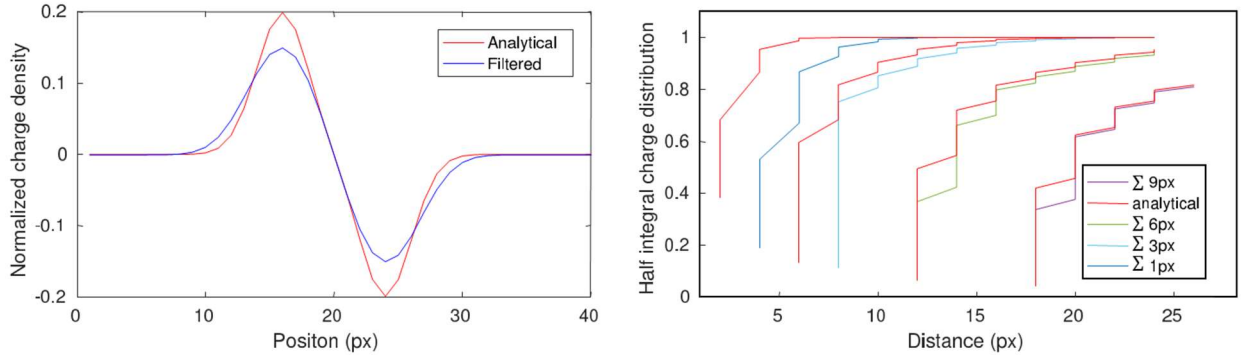

Figure 4-14 Effect of the SG-2D filter on two opposite Gaussian charge density distributions. (a) filter effect on two normal distributions with Σ 2 px, distance 8 px and patch image size 9 px. (b) half integral density charge distribution vs peak distance for different standard deviation and patch image size 9 px.

This behaviour is strengthened by the effect of the filter when the standard deviation for charge distribution is under the patch image size Figure 4-14b. In Figure 4-14a, an example of how this distribution is altered by the effect of the filter resolution is given. A parameter which permits to quantify this effect is the integral charge from the midpoint. To calculate this value and to avoid a further data manipulation, the values of the first derivative have been used. As shown in Figure 4-14b, this integral charge drastically drops when the peak distance approaches the characteristic threshold distance. This effect is more pronounced for large standard deviation of the charge distribution, but the effect of the SG-2D filter is to anticipate this threshold.

In conclusion, assuming a pixel resolution of 136 nm and an image patch area of 9 px, isolated charge density distributions with at least a standard deviation of about 500 nm are represented in this analysis without sensible attenuations. This limit can be extended also to opposite charge distributions distant at least by 1 µm. Under these limits the information can be averaged or spread. This study also suggests that the integral of a single charge distribution or a sum with the same sign is not altered by the filter.

4.4.3 Process influence on Semicon/LDPE surface potential distribution

Thanks to the methodology developed in the previous section, the influence of LDPE fabrication process is investigated.

4.4.3.1 PET cover layer

Figure 4-15 depicts the electric field and charge density profiles extracted using SG 2D-filter method.

For LDPE processed in Laplace, the electric field is constant in each SC layer, shows a maximum (minimum) at the left (right) interface and decreases linearly from left to right SC electrode. The charges density map presents charge accumulation close to interface with negative charge in LDPE and positive image charge in the SC.

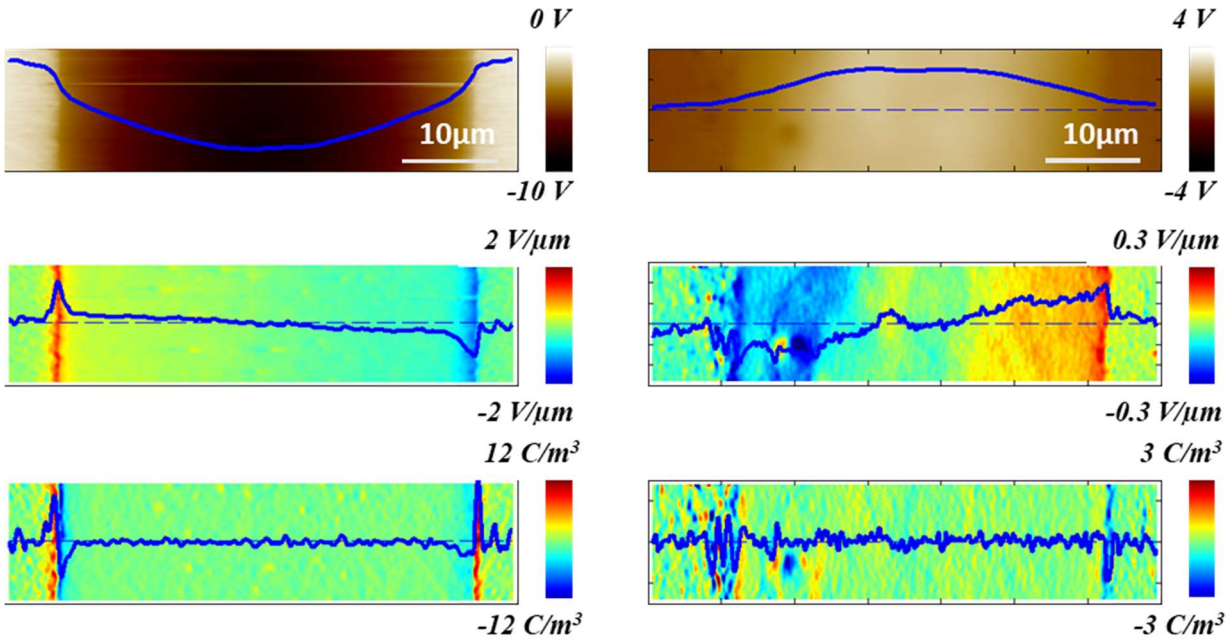

Figure 4-15 Comparison of (a; d) surface potential, (b; e) electric field and (c; f) charge density maps for sandwich whose LDPE was processed using PET in Laplace (left row) and ABB (right row). Charge density is computed using SG 2D method.

For LDPE processed in ABB, the electric field shows a similar profile. Indeed, it is constant in each SC layer; it presents a maximum (minimum) at right (left) interface and increases linearly from left to right SC electrode. The charge density map indicates charge accumulation close to the interface with positive charge in LDPE and negative image charge in SC.

The main difference is related to the charge present in LDPE close to interface. Indeed, LDPE processed in Laplace exhibit negative charges whereas ABB one has positive charges.

4.4.3.2 Al cover layer

The same procedure was applied on the SC/LDPE sandwich in which LDPE was processed using a Al cover layer. The results are summarized in Figure 4-16.

For LDPE processed in Laplace and ABB, the electric field is constant in each SC layer, exibit maximum (minimum) at left (right) interface and decreases linearly from left to right SC electrode. The Charge density map shows charge accumulation close to interface with negative charge in LDPE and positive image charge in the SC.

Contrary to LDPE processed with PET or LDPE using Al protecting layer leads to negative charge. Moreover, the amount of charge seems to be lower than previously.

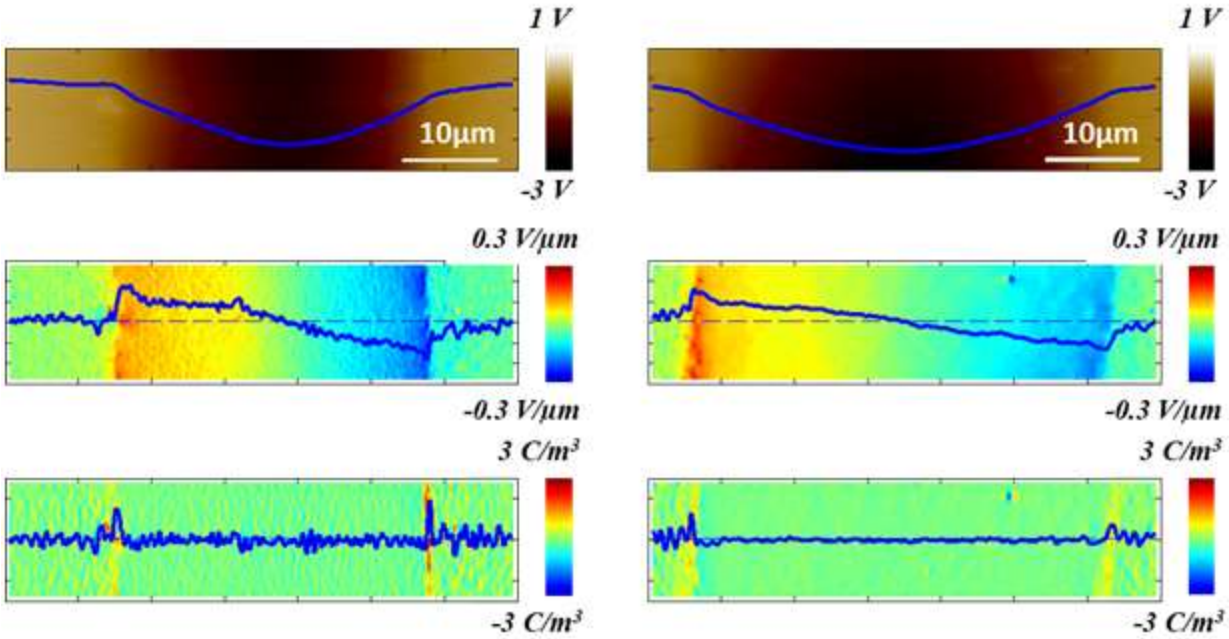

Figure 4-16 Comparison of (a; d) surface potential, (b; e) electric field and (c; f) charge density maps for sandwich whose LDPE was processed using Al in Laplace (left row) and ABB (right row). Charge density is computed using SG 2D method.

4.4.3.3 Comparison

Now, the charge density maps obtained for each process were compared. Whatever the process, negative or positive charge clouds spread over around 2-3µm in LDPE. However, the maximum density is strongly impacted by the fabrication process. Table 4-3 summarizes some characteristics of the charge density at the LDPE interface. The charge cloud spreading is estimated directly on the electric field profile, taking the distance from its relative maximum/minimum and the point in which the slope evidently changes. These two points have been used also to determine the surface charge density on the LDPE side of the plane traced by the interface. The maximum charge density is measured from the space charge profile.

Cover layer	Process	Interface charge depth (µm)	Maximum charge density (C/m^3)	Interface surface charge density ($\mu C/m^2$)
PET	Laplace	2.9 (3.7)	-7.1 (-3.0)	-8.5 (-6.7)
	ABB	1.9 (2.0)	+0.68 (+0.48)	+0.87 (+0.74)
Al	Laplace	3.5 (2.7)	-0.45 (-0.58)	-0.82 (-0.78)
	ABB	3.5 (2.7)	-0.28 (-0.22)	-0.65 (-0.34)

Table 4-3. Influence of process condition on charge density in LDPE close to SC/LDPE interface.

For Cu/LDPE or Au/LDPE interface, LeRoy et al. [Leroy16] reported contact charge density whose cloud spreads over 0.2 nm in LDPE with a density of $10^8 C/m^3$, as estimated by DFT (Density Functional Theory). It corresponds to a surface charge density of 0.02 C/m^2 and is a priori corresponding to the natural potential drop between the two materials. This value is higher than the value obtained experimentally in Table 4-3. This may be in part due to the fact that KPFM measurement spatial resolution (around 10 nm in air configuration) is lower than the real spatial distribution of charge. However, these results confirm that the bell-shape of the surface potential profile is due to charges located several micrometres away interface.

		Chemical characterization	Surface roughness	LDPE morphology	Injected charges (PEA)
PET	Laplace	Carbonyl groups	Low	Disordered lamella	Low ($0.2 C/m^3$)
	ABB			No spherulites	
Al	Laplace	Nothing	High	spherulites	Medium ($1 C/m^3$)
	ABB			No spherulites	

Table 4-4 Influence of process condition on properties of LDPE and on injected charge density. Results are extracted from figures presented in chapters 3 and 4.

Moreover, results presented in Table 4-3, highlight that charge density located close to interface is higher for LDPE processed with PET than with Al. To analyse these results, Table 4-4 summarizes LDPE properties and injected charge density measured by PEA in previous chapter. High charges in LDPE close to interface could be linked to the presence of carbonyl group due to the PET cover layer. This presence of charges close to interface seems to decrease the amount of injected charge.

As regards the variability of the potential profile and charge density and even change in sign of charge in case of PET cover layer, there is not definitive interpretation. LDPE processing may lead to

inhomogeneous dispersion of the oxidized groups, and given the local nature of measurements carried out by AFM, the dispersion of results is enhanced in respect to more macroscopic measurements.

4.4.4 Polarization influence on charge cloud located close to interface

Now an external electric field is applied on LDPE using external bias applied on SC. Two kinds of configuration are tested:

- Configuration A: +2V applied on left SC-electrode an -2V on right electrode
- Configuration B: -2V applied on left SC-electrode an +2V on right electrode

Figure 4-17 summarizes the results obtained for each polarization configuration.

Whatever polarization configuration, the surface potential profile is influenced by the applied potential. Indeed, the initial surface potential is now superposed to the linear one induced by the bias applied on the SC. This induced internal electric field and reverse behavior is observed in each polarization configuration, cf. Figure 4-17b and e.

Moreover, as explained previously, our method permits to extract the total charge density, i.e. free and polarization charges. So, negative charges are probed close to the anode and positive charges close to the cathode (Figure 4-17c and f). These charges are polarization charges, which confirms that our method is sensitive to free and polarization charges.

The following step will be to apply higher electric field to inject charges in LDPE, before surface potential probed by KPFM. This step was not yet performed but will be crucial to investigate at local scale charge injection and to compare injected charge density determined by KPFM and PEA.

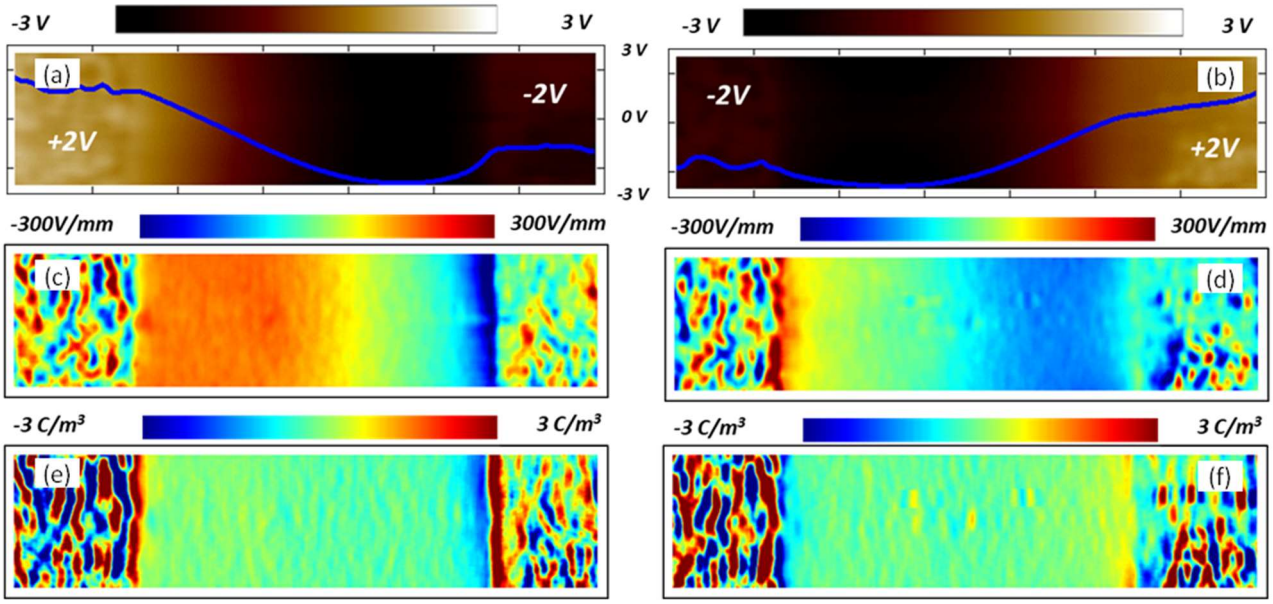

Figure 4-17 (a-d) Surface potential measured by PF-KPFM on sandwich with LDPE processed in ABB with Al cover layer measured applying polarization on SC layer. (b-e) Electric filed and (c-f) charge density profile computed using SG 2D method.

4.5 Wrap-up on information gained by AFM techniques

In conclusion, in this chapter the information gained by AFM techniques can be split into two parts: the first part is about the methodologies that have been settled to analyze the interfaces from the mechanical and electrical point of view; the second part concerns the knowledge and the open questions rose by the obtained results.

4.5.1 Methodologies

The methodologies described in this chapter involve, first of all, the physical characterization of the SC/LDPE interface, which also includes the characterization of the interface roughness or the eventual diffusion of CB into the LDPE volume; secondly, the electrical characterization by means of the surface potential measurements as well as the algorithm to calculate the electric field and the surface charge density.

A different approach has been proposed in order to identify the SC/LDPE interface based on the use of the PF-QNM mode, especially on the adhesion force cartography. This methodology represents an alternative technique to the more traditional optical microscope commonly used or the Raman microscopy scan [Bode06]. The exploitation of the PF-QNM allows a better resolution up to the nanoscale. Moreover, by means of the adhesion force contrast between the CB nanoparticles and the LDPE, the nanoparticles that diffuse into the LDPE can be detected. In addition, a precise measurement of the interface SC/LDPE has been defined since, by recognition of the CB nanoparticles embedded in the SC, it is possible to clearly distinguish the layer of SC with respect to the LDPE. Finally, thanks to this method, it is possible to measure the roughness of the SC/LDPE junction and confirm the absence of any diffusion of the CB nanoparticles in the LDPE layer.

The methodology for the electrical characterization can be applied on two KPFM modes: the AM-KPFM and the PF-KPFM modes. The first one simply measures the height in tapping mode and surface potential, with a very low impact on the sample. The second one couples the PF-QNM to the KPFM and has been used to compare the mechanical interface to the surface potential. The AM-KPFM has been preferred to probe the surface potential on sandwiches with an external bias applied to the two SC electrodes, because several measurements must be performed on exactly the same scanned area. As it has been said in the section 4.4.1, the approach used for the charge density quantification in LDPE layer even close to interfaces relies on the application of the Poisson's equation (4-6) to the surface potential and considers the resulting charge as the contribution of free and polarization charges. The different numerical computing methods lead to similar results when applied to the same PF-KPFM measurements. Using the AM-KPFM, the Savitzky-Golay 2D filter is the most resilient method to the noise. Assuming a pixel resolution of 136 nm and an image patch area of 9 px, isolated charge density spots, with at least a standard deviation of about 500 nm, are represented in this analysis without noticeable attenuation or deformation of the distribution. This limit can be extended also to opposite charge distributions distant by at least 1 µm. Under these limits the information can be averaged or spread. The approach using PF-KPFM is promising. Indeed, this technique permits to probe in the same time morphological and electrical properties of interface. By this way interface is characterized more completely than in previous studies [Tana05].

4.5.2 Interface physics

In this chapter, in order to study the physics of SC/LDPE interfaces, sandwiches prepared using different protecting layers, namely PI, Al and PET protecting layers, have been compared. In the case of PET and Al, we also compared sandwiches realized by the ABB and Laplace laboratories. All the samples exhibit the same sharp contrast of the adhesion force between the LDPE matrix and the CB nanoparticles. It has also been found that the LDPE films processed with Al and PI protecting layers exhibit higher interface roughness than the one processed with PET, consistently with our initial surface roughness conditions established before sandwich processing. For all the three protecting layers the absence of diffusion of CB from the SC to the LDPE is verified.

Comparison between adhesion and surface potential maps shows that, even if the physical interface is abrupt, the surface potential decreases slowly going from SC to LDPE. The potential variation is over a range of around 15µm and has a bell-shaped form, for all types of protecting layer. As it has been shown in section 4.3.1, due to the variations of the surface potential maximum from one cross-section to another in the same sandwich, the interpretation of the results is quite difficult. However, we can notice that the variation range is more important for the cross-section made using PET protecting layer. This can be due to surface chemistry changes (cf. FTIR and PL results in section 3.1) which could be non-homogenous over the surface, inducing differences between cross-sections coming from different areas of the same sandwich.

Moreover, from the measurement of the surface potential, charge density maps have been obtained for each process and compared. It has been found that, whatever the process, negative or positive charge clouds spread over around 2-3µm in LDPE. The maximum density is strongly impacted by the fabrication process changing from -7 C/m^3 to +0.7 C/m^3 for the PET layer, or, in terms of surface charge density, from -8 to +0.9 $\mu C/m^2$. This value is much lower than the value obtained theoretically. This is certainly due in part to the fact that KPFM measurement spatial resolution (around 10nm in air configuration) is poorer than the real spatial distribution of charge at contact. However, these results confirm that the bell-like shape of the surface potential profile is due to charges spreading over several µm away from the interface.

The charge density located close to interface is higher for LDPE processed with PET than with Al. High charge density in LDPE close to interface could be linked to the presence of carbonyl group due to PET cover layer. However, there is strong variation in the amount and sign of charge in the case of PET cover layer depending on process conditions. It is not clear whether this behaviour is a consequence of the interaction of the LDPE matter flow with PET surface during processing.

Finally, it has been found that the surface potential profile is influenced by the lateral bias through the SC electrode. Obviously, in this way, the initial surface potential is superposed to the linear one induced by the bias applied on the SC. This internal electric field induced by applying the dc voltage appears proportional to the applied voltage and there is no apparent evolution of the initial charge distribution under the moderate fields applied: this charge appears therefore relatively stable. The method presented here allows for the extraction of the total charge density, i.e. free and polarization charges. So, negative charges are probed close to the anode and positive charges close to the cathode. These charges are polarization charges, which confirms that our method is sensitive to both free and polarization charges. As future perspective of this work, the application of higher electric field to

inject charges in LDPE will be crucial to investigate at a local scale the charge injection and to compare injected charge density determined by KPFM and PEA.

Conclusion and Perspectives

In this thesis, which was conducted in a collaboration with ABB Corporate Research, the physical processes occurring at the polymer insulation/conductive filler interface were investigated. The intention was to understand the electrical behaviour at the interface of low-density polyethylene (LDPE) polymer insulation and its electrode, particularly the conductive "semicon" material which is the polymer filled with carbon black. Focus was therefore put on correlations between microscopic interface properties investigated with different AFM-based techniques, and the macroscopic electric behaviour, such as space charge accumulation and polarization currents.

In a first step, various LDPE samples have been realised, each one made by using different protecting layers during sample preparation, such as PI, PET and Al, in order to find out whether the cover layer has an impact on the physical properties of the final LDPE film surface, e.g. via influencing the surface roughness and/or chemical properties by creating surface contaminations. Additionally, different samples prepared by LAPLACE laboratories and ABB Corporate Research have been investigated. Hence, the most important results concerning the physical and electrical properties of the LDPE/SC interface are exposed in this thesis.

Firstly, in order to see whether the protecting layer used in press-molding polyethylene has an effect on the chemical, structural and electrical properties of a LDPE sample, photoluminescence (PL) and Fourier transformed infrared spectroscopy (FTIR), AFM and KPFM measurements have been performed, as detailed in Chapter 3. This issue is important because a significant effect of the cover-layer would make it impossible to electrically characterize the real application material by measurements on small lab-samples. The PL and FTIR spectra of LDPE processed with PET as protecting layer clearly indicated contamination by PET during the press-molding process. More specifically this can be attributed to the diffusion of oxidized groups, presumably decomposition products or oligomer chains from PET into the LDPE surface. Moreover, as revealed by the roughness analysis conducted via AFM, smooth surfaces are obtained using PET. However, in the present work, no noticeable variation of the conductivity has been found related to the different press-molding processes. This finding is dependent on the order of magnitude of the electric field used to evaluate the conductivity as well as the specific electrodes deposited on the film surface.

Chapter 4 reports on the physical and electrical characterization of the SC/LDPE interface. The numerical method to calculate the electric field and the interface charge density map from the surface potential measurements is also described here. The PF-QNM technique, exploited to accomplish the physical characterization, allowed to distinguish the CB nanoparticles encapsulated in the SC by means of adhesion force contrast between CB and SC. Thus, it has been possible to discern that no inter-diffusion of CB nanoparticles in the LDPE layer occurred during the molding process. As the CB nanoparticles are embedded in the SC layer and modify the mechanical properties accordingly, the interface between SC and LDPE and its roughness could be identified. As a result, all the samples exhibit the same sharp contrast of the adhesion force between the LDPE matrix and the CB nanoparticles. It has also been found that the LDPE films processed with Al and PI protecting layers exhibit higher interface roughness than the one processed with PET, consistently with the surface roughness results concerning the LDPE before sandwiching, as mentioned above. For all the three protecting layers, the absence of diffusion of CB from the SC to the LDPE and the absence of voids

have been verified. The PF-QNM technique represents a novel approach for the study of the interface, allowing for a better resolution down to the nanoscale.

In order to achieve the characterization of the electrical properties for the SC/LDPE interface in terms of a quantitative mapping of the space charge density, Poisson`s equation has been applied starting from the surface potential measurements performed via the AM-KPFM technique. Importantly, this numerical approach allows for the distinction of free and polarization charges. Furthermore, PF-KPFM technique has been also applied, allowing for the simultaneous accomplishment of AM-KPFM surface potential measurements and the PF-QNM measurements of interface localization, representing a powerful tool for the comparison of morphological and electrical properties of the interface. In this way, it has been unveiled that, although the physical interface is abrupt, the surface potential decreases slowly going from SC to LDPE. The potential varies over a range of around 15µm and has a bell-shaped form for all the samples independently of the protecting layer. However, from a more quantitative viewpoint, the surface potential maximum values change from one cross-section to another in the same sandwich. This variation is more distinct for the cross-section made using PET protecting layer. It can be due to surface chemistry changes, as indicated by FTIR and PL spectra, which could be non-homogenous over the surface, inducing differences between cross-sections coming from different areas of the same sandwich. Furthermore, after calculation of space charge maps, it has been noted that the maximum value of space charge density at the interface, evaluated via PF-KPFM, depends on the different fabrication process, being higher in the case of LDPE processed with PET and decreasing for Al-processed LDPE films, which could be linked to the presence of carbonyl group due to PET cover layer. However, there is strong variation in the amount and sign of charge in the case of PET cover layer depending on process conditions. It is not clear whether this behaviour is a consequence of the interaction of the LDPE matter flow with PET surface during processing. These results confirm that the bell-like shape of the surface potential profile is due to charges spreading over several µm away from the interface. By applying a lateral dc voltage through the SC/LDPE/SC structure, it has been also evidenced that the internal electric field induced is proportional to the applied voltage and there is no apparent evolution of the initial charge distribution under the moderate fields applied which means that the charge appears relatively stable.

Finally, the synergetic use of AFM-based techniques, such as PF-QNM, AM-KPFM and PF-KPFM, has been demonstrated here to represent not only a novel approach for the most complete and thorough characterization of insulating material interfaces, but, more importantly, to constitute a valid method for the study of electrical phenomena at the interface, such as space charge accumulation and injection, allowing for the simultaneous correlation of the electrical properties to the physical interface characteristics, like roughness. The scatter in the results of surface potential profiles obtained by KPFM in case of LDPE processed with PET protective layer are suspected to be linked to the dispersion in amount of surface contamination.

A future continuation of this work should include the challenging task of measuring the microscopic potential after charge injection at high fields and to compare injected charge density determined by KPFM and PEA method. Also the achievement of a better control of the fabrication process should be addressed in order to improve the reproducibility of the surface potential measurements. Finally, the achievement of charge injection control via tailoring the properties of LDPE/SC interface may be

addressed by exploiting the novel approach proposed here, thus providing a possible way to control the injection in power cables and other electrical components.

List of Figures

List of Tables

References

A

[Aida97] F. Aida, S. Wang, M. Fujita, G. Tanimoto, Y. Fujiwara, "Study of the Mechanism of Space Charge Formation in Polyethylene", Journal of Electrostatics, vol. 42, pp. 3-15, 1997.

[Alle77a] N. S. Allen, J. Homer, J. F. Mckellar, "Origin and role of the luminescent species in the photo-oxidation of commercial polypropylene", Journal of Applied Polymer Science, Vol. 21, pp. 2261-2267, 1977.

[Alle77b] N. S. Allen, J. Homer, J.F. Mckellar, "Identification of the luminescent species in low-density polyethylene", Journal of Applied Polymer Science, vol. 21, pp. 3147-3152, 1977.

[Alle78] N. S. Allen and J. F. Mckellar, "Luminescence and photo-oxidation of commercial Poly(4-methylpent-1-ene)", Journal of Applied Polymer Science, vol. 22, pp. 625-631, 1978.

[Alle79] N. S. Allen and J. McKellar, "The role of luminescent species in the photooxydation of commercial polymers, in Developments in Polymer Degradation", N. G. Grassie, Applied Science Publishers Ltd., London, 1979.

[An09] Z. An, C. Xie, Y. Jiang, F. Zheng, Y. Zhang, "Significant suppression of space charge injection into linear low density polyethylene by surface oxyfluorination", Journal of Applied Physics, vol. 105, pp. 104112-104112-4, 2009.

[And06] T. Andrews, R. N. Hampton, A. Smedberg, D. Wald, V. Waschk, W. Weissenberg, "The Role of Degassing in XLPE Power Cable Manufacture", IEEE Electrical Insulation Magazine, vol. 22, pp. 5-16, 2006.

B

[Bard47] J. Bardeen, "Surface States and Rectification at a Metal Semi-Conductor Contact", Physical Review, vol. 71, pp. 717–727, 1947.

[Bass81] D. C. Bassett and A. M. Hodge, "On the Morphology of Melt-Crystallized Polyethylene. III. Spherulitic Organization", Proceedings of the Royal Society A: Mathematical, Physical and Engineering Sciences, vol. 377, pp. 61–71, 1981.

[Benne15] R. Bennewitz, "Friction force microscopy", Fundamentals of Friction and Wear on the Nanoscale", Springer Cham, pp. 3-16, 2015.

[Bode04] R. Bodega, G.C. Montanari, and P.H.F. Morshuis, "Conduction Current measurements on XLPE and EPR insulation", Proceedings IEEE Conference Electrical Insulation and Dielectric Phenomena, pp. 101–105, 2004.

[Bode06] R. Bodega, "Space charge accumulation in polymeric high Voltage DC Cable systems", PhD Thesis, Delft University of Technology, 2006.

[Bous67] I. Boustead and A. Charlesby, "Identification of luminescence centres in low density polyethylene", European Polymer Journal, vol. 3, pp. 459-471, 1967.

C

[Cao88] T. Cao, S. N. Magonov, R. Qian, "Effect of crystallinity on the excimer fluorescence of poly (ethylene terephthalate) film", Polymer communications, vol. 29, pp. 43-44, 1988.

[Capp99] B. Cappella, G. Dietler, "Force-distance curves by atomic force microscopy", Surface Science Reports, vol. 34, pp. 1-104, 1999.

[Charl65] A. Charlesby and R. H. Partridge, "The identification of luminescence centres in polyethylene and other polymers", Proceedings of the Royal Society of London A: Mathematical, Physical and Engineering Sciences, vol. 283, pp. 312-328, 1965.

[Chen04] G. Chen, Y. Tanaka, T. Takada and L. Zhong, "Effect of polyethylene interface on space charge formation", IEEE Transactions on Dielectrics and Electrical Insulation, vol. 11, pp. 113-121, 2004.

[Chen16] L. Chen, T. D. Huan, Y. C. Quintero and R Ramprasad "Charge injection barriers at metal/polyethylene interfaces", Journal of materials science, vol. 51, pp. 506-12, 2016.

[Chen17] Y. J. Chen, M. J. Zhang, S. Yuan, Y. Qiu, X. B. Wang, X. Jiang, Z. Gao, Y. Lin and F. Pan, "Insight into interfaces and junction of polycrystalline silicon solar cells by kelvin probe force microscopy", NanoEnergy, vol. 36, pp. 303-312, 2017.

[Chow74] A. Chowdry, C. R. Westgate, "The role of bulk traps in metal-insulator contact charging", Journal of Physics D: Applied Physics, vol. 7, pp. 713–725, 1974.

[Chr10] T. Christen, L. Donzel, and F. Greuter, "Nonlinear resistive electric field grading Part 1: Theory and Simulation", IEEE Electrical Insulation Magazine vol. 26, pp. 47-59, 2010.

[Chr15] T. Christen, "HVDC insulation boundary conditions for modeling and simulation", IEEE Transactions on Dielectrics and Electrical Insulation, vol. 22, pp. 35–44, 2015.

[Clau92] B. Clauss, D.R. Salem, "Characterization of the non-crystalline phase of oriented poly (ethylene terephthalate) by chain-intrinsic fluorescence", Polymer, vol. 33, pp. 3193-3202, 1992.

[Coel93] R. Coelho, B. Aladenize, "Les Diélectriques: Propriétés Diélectriques des Matériaux Isolants", Hermes, 1993.

D

[Delp08] S. Delpino, D. Fabiani, G.C Montanari, C. Laurent, G. Teyssedre, P.H.F. Morshuis, R. Bodega, L.A. Dissado, "Polymeric HVDC Cable Design and Space Charge Accumulation. Part 2: Insulation Interfaces," IEEE Electrical Insulation Magazine, vol. 24, pp. 14–24, 2008.

[Diss92] L. A. Dissado, J. C. Fothergill, "Electrical degradation and break down in polymers", London: Peter Peregrinus Ltd., 1992.

[Diss95] L. Dissado, G. Mazzanti, G.C. Montanari, "The incorporation of space charge degradation in the life model for electrical insulating materials", IEEE Transactionson Dielectrics and Electrical Insulation, vol.2, pp. 1147-1158, 1995.

[Dyms15] A. Dymshits, A. Henning, G. Segev, Y. Rosenwaks and L. Etgar, "The electronic structure of metal oxide/organo metal halide perovskite junctions in perovskite based solar cells", Scientific Reports, vol. 5, no. 8407, 2015.

E

[Emme16] F. Emmerich, C. Thielemann "Real-space measurement of potential distribution in PECVD ONO electrets byKPFM", Nanotechnology, vol. 27, no. 205703, 2016.

[Elme15] P. Elmer, "FT-IR Spectroscopy Attenuated Total Reflectance (ATR)", Technical Note, Available from: <http://www.utsc.utoronto.ca/~traceslab/ATR_FTIR.pdf> (Retrieved Oct. 2017).

F

[Fali17] K. Faliya, H. Kliem, C. J. Dias, "Space charge measurements with Kelvin Probe Force Microscopy", IEEE Transactions on Dielectrics and Electrical Insulation, vol. 24, pp. 1913-1922, 2017.

[Four00] R. Fournié and R. Coelho, "Diélectrique - Bases théoriques", Techniques de l'Ingénieur, vol. D3, no. D2300, pp. 1-18, 2000.

[Fowl28] R. H. Fowler, L. Nordheim, "Electron Emission in Intense Electrical Field", Proceedings of the Royal Society, vol. 119, pp. 173, 1928.

G

[Ghor16a] H. Ghorbani, M. Saltzer, F. Abid, H. Edin, "Effect of heat-treatment and sample preparation on physical properties of XLPE DC cable insulation material", IEEE Transactions on Dielectrics and Electrical Insulation, vol. 23, pp. 2508-2516, 2016.

[Ghor16b] H. Ghorbani, M. Saltzer, C.O. Olsson, "Observation of non-monotonic dependence of leakage current with temperature during thermal cycling", IEEE Electrical Insulation Conference, pp. 488-491, 2016.

[Ghor17] H. Ghorbani, T. Christen, M. Carlen, E. Logakis, L. Herrmann, H. Hillborg, L. Petersson, J. Viertel, "Long-term conductivity decrease of polyethylene and polypropylene insulation materials", IEEE Transactions on Dielectrics and Electrical Insulation, vol. 24, pp. 1485-1493, 2017.

[Gilb89] R. Gilbert, J.-P. Crine, B. Noirhomme, S. Pélissou, "Measurement of Organic and Inorganic Ions in Cable Insulation and Shields", Proceedings Conference on Electrical Insulation and Dielectric Phenomena, Leesburg, USA, pp. 235-240, 1989.

[Gome99] S. Gomès, N. Trannoy, P. Grossel, "D.C Thermal Microscopy: Study of the thermal exchanges between a probe and a sample", Measurement Science and Technology, vol. 10, pp. 805-811, 1999.

[Grob 07] M. Grobosch, M. Knupfer, "Charge-Injection barriers at realistic metal/organic interfaces: metals become faceless", Advanced Materials, vol.19, pp.754-756, 2007.

H

[Han03] T. L. Hanley, R. P. Burford, R. J. Fleming, K. W. Barber, "A general review of polymeric insulation for use in HVDC cables", IEEE Electrical Insulation Magazine, vol. 19, pp. 13-24, 2003.

[Hart99] M. Hartmann, "Magnetic Force Microscopy", Annual Review of Materials Science, vol. 29, pp. 53-87, 1999.

[Hash93] H. Hashimoto, M. Hasegawa, K. Horie, T. Yamashita, H. Ushiki, I. Mita, "Fluorescence study of thermotropic liquid-crystalline polyesters", Journal of Polymer Science Part B: Polymer Physics, vol. 31, pp. 1187-1196, 1993.

[Hemk88] D. J. Hemker, C. W. Frank, J. W, Thomas, "Photophysical studies of amorphous orientation in poly (ethylene terephthalate) films", Polymer, vol. 29, pp. 437-447, 1988.

[Henn86] M. Hennecke, J. Fuhrman, "Polarized fluorescence spectra of poly (ethylene terephthalate) films", Macromolecular Symposia", vol. 5, pp. 181-186, 1986.

[Ho01] Y. F. F. Ho, G. Chen, A. E. Davies, R. N. Hampton, S. G. Swingler, and S. J. Sutton, "Do Semicons Affect Space Charge?", Proceedings International Conference on Solid Dielectrics, pp. 105-108, 2001.

[Hoan10] T.V. Hoan, "Injection de charges dans le polyéthylène téréphtalate a partir de la méthode de l'onde de pression induite par impact laser (lipp): modélisation physique et optimisation de la méthode, influence des paramètres de l'interface métal-isolant", PhD Thesis, Université de Grenoble, 2010.

[Hoff 91] R. Hoffmann, C. Janiak, C. Kollmar, "A chemical approach to the orbitals of organic polymers", Macromolecules Journal, vol. 24, pp. 3725-3746, 1991.

[Huan17a] Y. Huang, J. Jämbeck, M. Unge, "Understanding the ionic conduction in dielectric polymers at high electric fields using molecular dynamics simulations," ACS Macro Letters, vol. 6, pp. 571-574, 2017.

[Huan17b] Y. Huang, L.S. Schadler, "Understanding the strain-dependent dielectric behavior of carbon black reinforced natural rubber–An interfacial or bulk phenomenon?", Composites Science and Technology, vol. 142, pp. 91-97, 2017.

[Hutt93] J. L. Hutter and J. Bechhoefer. "Calibration of atomic-force microscope tips", Review of Scientific Instruments, vol. 64, pp. 1868-1873, 1993.

[Huza10] A. Huzayyin, S. Boggs, R. Ramprasad, "Quantum mechanical studies of carbonyl impurities in dielectric polyethylene," IEEE Transactions on Dielectrics and Electrical Insulation, vol. 17, pp. 920–925, 2010.

I

[Ieda84] M. Ieda, "Electrical conduction and carrier traps in polymeric materials", IEEE Transactions on Electrical Insulation, vol. 19, pp.162-178, 1984.

[Ishi99] H. Ishii, K. Sugiyama, E. Ito, K. Seki, "Energy Level Alignment and Interfacial Electronic Structures at Organic/Metal and Organic/Organic Interfaces", Advanced Materials, vol. 11, pp. 605–625, 1999.

[Ishi10] M. Ishii, "Static states and dynamic behavior of charges: observation and control by scanning probe microscopy", Journal of Physics: Condensed Matter, vol. 22, no. 173001, 2010.

J

[Jaco98] H. O. Jacobs, P. Leuchtmann, O. J. Homan, A. Stemmer, "Resolution and contrast in Kelvin probe force microscopy", Journal of Applied Physics vol. 84, pp. 1168-1173, 1998.

[Jacq93a] P. P. L. Jacques, R. C. Poller, "Fluorescence of polyolefins. 1. Effect of thermal degradation on fluorescent excitation and emission spectra", European polymer journal, vol. 29, pp. 75-81, 1993.

[Jacq93b] P. P. L. Jacques, R. C. Poller, "Fluorescence of polyolefins. 2. Use of model compounds to identify fluorescent species in thermally degraded polymers", European polymer journal, vol. 29, pp. 83-89, 1993.

[Joh04] S. G. Johansson, G. Asplund, E. Jansson, R. Rudervall, "Power system stability benefits with VSC DC-transmission systems", Conseil International des Grands Réseaux Électriques, pp. 1-8, 2004.

K

[Kali00] S. V. Kalinin, D. A. Bonnell, "Surface potential at surface-interface junctions in SrTiO3 bicrystals", Physical Review B, vol. 62, pp. 10419-10431, 2000.

[Kao 81] K. C. Kao, W. Hwang, "Electrical Transport in Solids", Pergamon Press, vol.14, p.76, 1981.

[Kitt05] C. Kittel, "Introduction to solid state physics", Wiley, 2005.

[Koen66] J. L. Koenig, D. E. Witenhafer, "Infrared studies of polymer chain folding I. Linear polyethylene", Macromolecular Chemistry and Physics, vol.99, pp. 193–201, 1966.

[Krim56] S. Krimm, C.Y. Liang, G. Sutherland, "Infrared spectra of high polymers. II. Polyethylene", The Journal of Chemical Physics, vol. 25, pp. 549-562 1956.

[Kryv16] O. Kryvchenkova, I. Abdullah, J. E. Macdonald, M. Elliott, T. D. Anthopoulos, Y. H. Lin, P. Igić, K. Kalna, R. J. Cobley, "Non destructive method for mapping metal contact diffusion in InO3 thin film transistors", ACS Applied Material& Interfaces, vol. 8, pp. 25631-25636, 2016.

L

[Lamp70] M. A. Lampert, P. Mark, "Current Injection in Solids", Academic Press, 1970.

[Lanz17] M. Lanza "Conductive Atomic Force Microscopy", John Wiley and Sons, 2017

[Laur95] C. Laurent, F. Massines, C. Mayoux, D. M. Ryder, C. Olliff, "Comparison between photo- and electro-induced luminescence spectra of polyethylene", Annual Report Conference on Electrical Insulation and Dielectric Phenomena, p. 93-96., 1995.

[LDPE15] "ExxonMobilTM LDPE LD 101BA Wire & Cable", Available from: <https://exxonmobilchemical.ides.com/datasheet.aspx?I=58933&FMT=PDF&CULTURE=en-US&PS=PE&E=243942> (Retrieved Oct. 2017).

[Leng66] G. Lengyel, "Schottky Emission and Conduction in Some Organic Insulating Materials", Journal of Applied Physics, vol. 37, pp. 807–810, 1966.

[LeRoy04] S. Leroy, "Modélisation numérique des phénomènes de transport électrique dans un isolant polyéthylène sous contrainte électrique", PhD Thesis Université de Toulouse III, 2004.

[LeRoy05] S. Le Roy, F. Boufayed, G. Teyssedre, C. Laurent, P. Segur, R. Bodega, P. H. F. Morshuis, G. C. Montanari, L. A. Dissado, "Computer simulation of space charge distribution in an XLPE-EPR sandwich", Annual Report Conference on Electrical Insulation and Dielectric Phenomena, pp. 661-664, 2005.

[LeRoy06] S. Le Roy, G. Teyssedre, C. Laurent, G.C. Montanari, F. Palmieri, "Description of charge transport in polyethylene using a fluid model with a constant mobility: fitting model and experiments", Journal of Physics D: Applied Physics, vol. 39, pp. 1427-1436, 2006.

[LeRoy16] S. Le Roy, C. Villeneuve-Faure, A. Huzayyin, J.H. Chang, "Coupling molecular modeling, fluid modeling, and KPFM measurements to characterize an interface at the nanoscale", Dielectrics (ICD), 2016 IEEE International Conference on, vol. 2, pp.897-900, 2016.

[Lewi94] T.J. Lewis, "Nanometric dielectrics", IEEE Transactions on Dielectrics and Electrical Insulation, vol. 1, pp. 812-825, 1994.

[Liang59] C.Y. Liang, S. Krimm, "Infrared spectra of high polymers: Part IX. Polyethylene terephthalate", Journal of molecular spectroscopy, vol. 3, pp. 554-574, 1959.

M

[Maug00] D. Maugis, "Contact, adhesion and rupture of elastic solid", Springer, 2000.

[McNi11] T. McNichol "AC/DC: The Savage Tale of the First Standards War", John Wiley & Sons, 2011.

[Meli11] W. Meliz, J. Shen, A. C. Kummel, S. Lee, "Kelvin probe force microscopy and its application", Surface Science Reports, vol. 66, pp.1-27, 2011.

[Meun00] M. Meunier, N. Quirke "Molecular modeling of electron trapping in polymer insulators", The Journal of Chemical Physics, vol. 113, pp. 369-376, 2000.

[Meun01] M. Meunier, N. Quirke, "Molecular modelling of electron traps in polymer insulator: chemical defects and impurities", The Journal of Chemical Physics, vol. 115, pp. 2876-2881, 2001.

[Mill16] L. Milliere, K. Makasheva, C. Laurent, B. Despax, L. Boudou, & G. Teyssedre, "Silver nanoparticles as a key feature of a plasma polymer composite layer in mitigation of charge injection into polyethylene under dc stress", Journal of Physics D: Applied Physics, vol. 49, pp. 015304, 2016.

[Mizu76] T. Mizutani, Y. Takai, T. Osawa, M. Ieda, "Barrier heights and surface states of metal-polymer (PET) contacts", Journal of Physics D: Applied Physics, vol. 9, pp.2253-59, 1976.

[Mizu86] T. Mizutani, S. Ikeda, M. Ieda, "Oxidation enhanced TSC and TSSP of polyethylene", Japanese Journal of Applied Physics, vol. 22, pp. 22-26, 1986.

[Mizu94] T. Mizutani, "Space Charge Measurement Techniques and Space Charge in Polyethylene" IEEE Transactions on Dielectrics and Electrical Insulation, vol. 1, pp. 923–933, 1994.

[Mont00] G. C. Montanari, “The electrical degradation threshold of polyethylene investigated by space charge and conduction current measurements”, IEEE Transactions on Dielectrics and Electrical Insulation, vol. 7, pp. 309–315, 2000.

[Mors05] P.H. F. Morshuis, “Degradation of solid dielectrics due to internal partial discharge: some thoughts on progress made and where to go now”. IEEE Transactions on Dielectrics and Electrical Insulation, vol. 12, pp. 905-913, 2005.

[Mors13] P. H. F. Morshuis, “Interfaces: to be avoided or to be treasured?”, IEEE International Conference on Solid Dielectrics, pp. 1-9, 2013.

[Mott48] N. F. Mott, R. W. Gurney, “Electronic Processes in Ionic Crystals”, Oxford University Press, 1948.

[Mott71] N. F. Mott and E. A. Davis. “Electronic process in non-crystalline materials”, Oxford University Press, 1971.

N

[Nea09] E.R. Neagu, C. J. Dias, “Charge injection/extraction at metal-dielectric interface: an experimental validation”, IEEE Electrical Insulation Magazine, vol. 25, pp. 15-22, 2009.

[Nels14] J.K. Nelson, “Nanodielectrics – the first decade and beyond”, Proceedings of International Symposium on Electrical Insulating Materials, pp. 1-11, 2014.

[Nonn91] M. Nonnenmacher, M. P. O’Boyle, and H. K. Wickramasinghe “Kelvin probe force microscopy”, Applied physics letters, vol. 58, pp. 2921-2923, 1991.

O

[O'dw73] J. J. O'Dwyer, “The Theory of Electrical Conduction and Breakdown in Solid Dielectrics”, Clarendon, 1973.

[Ohler07] B. Ohler, "Practical advice on the determination of cantilever spring constants", Application Note Veeco Instruments Inc, 2010.

P

[Pele13] A. Peled, J. Castro and W.J. Weiss “Atomic Force and Lateral Force Microscopy (AFM and LFM) examinations of cement and cement hydration products”, Cement and Concrete Composites, vol. 36, pp. 48-55, 2013.

[Piet16] G. Pietrini, D. Barater, G. Franceschini, P. Mancinelli and A. Cavallini, "An open problem for More Electrical Aircraft (MEA): How insulation systems of actuators can be qualified?", IEEE Energy Conversion Congress and Exposition, Milwaukee, WI, pp. 1-8, 2016.

[Pitt10] B. Pittenger, N. Erina, & C. Su, “Quantitative mechanical property mapping at the nanoscale with PeakForce QNM” Application Note Veeco Instruments Inc, pp. 1-12, 2010.

[Pope76] D. P. Pope, H. H. Wills, “Characterization of Oriented Low-Density Polyethylene Samples by Differential Scanning Calorimetry”, Journal of Polymer Science Polymer: Physics Edition vol. 14, pp. 811-820, 1976.

[Ples16] I. Plesa, P.V. Notingher, S. Schlögl, C. Sumereder, M. Muhr, "Properties of polymer composites used in high-voltage applications", Polymers, vol. 8, pp. 1-63, 2016.

Q

[Qiao15] B. Qiao "Electrical ageing of insulating polymers: approach through electroluminescence and cathodoluminescence analyses", PhD Thesis Université de Toulouse III, 2015.

[Qiao16] B. Qiao, C. Laurent, G. Teyssedre, "Electroluminescence and cathodoluminescence from polyethylene and polypropylene films: spectra reconstruction from elementary components and underlying mechanisms", Journal of Applied Physics, vol. 119, p. 024103, 2016.

R

[Radm94] M. Radmacher, M. Fritz, J. P. Cleaveland, D. A. Walters, P. K. Hansma, "Imaging adhesion Forces and elasticity of Lysozyme adsorbed on Mica with AFM", Langmuir, vol. 10, pp. 3809-3814, 1994.

[Reze09] C. A. Rezende, R. F. Gouveia, M. A. Da Silva, F. Galembeck, "Detection of charge distributions in insulator surfaces", Journal of Physics: Condensed Matter, vol. 21, no. 263002, 2009.

[Ried09] C. Riedel, R. Arinero, P. Tordjeman, M. Ramonda, G. Lévêque, G. A. Schwartz, D. G. De Oteyza, A. Alegria, J. Colmenero "Determination of the nanoscale dielectric constant by means of a double pass method using electrostatic force microscopy", Journal of Applied Physics, vol. 106, no. 024315, 2009

[Robi00] F. Robin, H. Jacobs, O. Homan, A. Stemmer, W. Bachtold, "Investigation of the cleaved surface of a p –i –n laser using Kelvin probe force microscopy and two-dimensional physical simulations", Applied physics letters, vol. 76, pp. 2907-2909, 2000.

S

[Sze81] S. M. Sze, "Physics of Semiconductor Devices", Wiley, 1981

[Sko10] J. Skog, H. Van Asten, T. Worzyk, T. Andersrod, "NorNed - world's longest power cable", CIGRE (Conseil International des Grands Réseaux Électriques) Report B1-106, 2010.

[Shock48] W. Shockley, G. L. Pearson, "Modulation of conductance of thin films of semi-conductors by surface charges", Physical Review, vol.74, pp.232-233, 1948.

T

[Takai78] Y. Takai, T. Mizutani, M. Ieda, "Photoluminescence study in polymers", Japanese Journal of Applied Physics, vol. 17, pp. 651-658, 1978.

[Take99] T. Takeda, N. Hozumi, H. Suzuki, and T. Okamoto, "Factors of Hetero Space Charge Generation in XLPE under DC Electric Field of 20 kV/mm", Electrical Engineering in Japan, vol. 129, pp. 13-21, 1999.

[Taleb09] M. Taleb, G. Teyssèdre, S. Le Roy, "Role of the interface on charge build-up in a low-density polyethylene: surface roughness and nature of the electrode", Proc. IEEE Int. Conf. on Electrical Insulation and Dielectric Phenomena, pp. 112-115, 2009.

[Taleb13] M. Taleb, G. Teyssedre, S. Le Roy, C. Laurent, "Modelling of charge injection and extraction in a metal/polymer interface through an exponential distribution of surface states". IEEE Transactions on Dielectrics and Electrical Insulation, vol. 20, pp. 311-320, 2013.

[Tana05] T. Tanaka, M. Kozako, N. Fuse, Y. Ohki, "Proposal of a multi-core model for polymer nanocomposite dielectrics", IEEE Transactions on Dielectrics and Electrical Insulation, vol. 12, pp. 669-681, 2005.

[Tana11] T. Tanaka, "Nanodielectrics: how does the presence of interfaces influence behaviour", International Conference on Power and Energy System, 2011.

[Tamm33] I. Tamm, "A possible binding of the electrons on a crystal surface", Journal of Experimental and Theoretical Physics, vol. 3 pp. 34-35, 1933.

[Taw05] T. M. Tawalbeh, S. Saq'an, S. F. Yasin, A. M. Zihlifi and G. Ragosta "Low temperature electrical conductivity of low-density polyethylene/carbon black composites", Journal of Materials Science: Materials in Electronics, vol. 16, pp. 351-354, 2005.

[Tear59] P. W. Teare, "The crystal structure of orthorhombic hexatriacontane, C36H74", Acta Crystallographica, vol. 12, pp. 294-300, 1959.

[Teys98] G. Teyssedre, L. Cisse, C. Laurent, F. Massines, P. Tiemblo, "Spectral analysis of optical emission due to isothermal charge recombination in polyolefins", IEEE transactions on dielectrics and electrical insulation, vol. 5, pp. 527-535, 1998.

[Teys01a] G. Teyssedre, C. Laurent, A. Aslanides, N. Quirke, L. A. Dissado, G. C. Montanari, A. Campus, L. Martinotto "Deep trapping centers in crosslinked polyethylene investigated by molecular modeling and luminescence techniques", IEEE Transactions on Dielectrics and Electrical Insulation, vol. 8, pp. 744-752, 2001.

[Teys01b] G. Teyssedre, J. Menegotto, and C. Laurent, "Temperature dependence of the photoluminescence in Poly(ethylene terephthalate) ", Polymer, vol. 42, pp. 8207-8216, 2001.

[Teys09] G. Teyssedre, C. Laurent, G. Perrego and G.C. Montanari, "Charge recombination induced luminescence of chemically modified crosslinked polyethylene materials", IEEE Transactions on Dielectrics and Electrical Insulation, vol. 16, pp. 232-240, 2009.

[Teys17] G. Teyssedre, S. T. Li, K. Makasheva, N. Zhao, L. Milliere, C. Laurent, "Interface tailoring for charge injection control in polyethylene", IEEE Transactions on Dielectrics and Electrical Insulation, vol. 24, pp. 1319-1330, 2017.

[Tiem99] P. Tiemblo, J. M. Gomez-Elvira, G. Teyssedre, F. Massines, C. Laurent, "Chemiluminescence spectral evolution along the thermal oxidation of isotactic polypropylene". Polymer Degradation and Stability 65, pp. 113-121, 1999.

[Thie96] A. Thielen, J. Niezette, G. Feyder, J. Vanderschueren, "Thermally stimulated current study of space charge formation and contact effects in metal-Polyethylene Terephthalate film-metal systems. I. Generalities and theoretical model", Journal of Physics and Chemistry of Solids, vol. 57, pp. 1567-1580, 1996.

[Thom11] C. Thomas, G Teyssedre, C. Laurent, "Space charge dynamic in polyethylene: from DC to AC stress", Journal of Physics D: Applied Physics, vol. 44, pp. 015401, 2011.

U

[Unge13] M. Unge, C. Törnkvist, T. Christen, "Space charges and deep traps in polyethylene—Ab initio simulations of chemical impurities and defects", IEEE International Conference on Solid Dielectrics, pp. 935-939, 2013.

V

[Vand94] W. Vandervorst, M. Meuris, "Method for resistance measurements on a semiconductor element with controlled probe pressure", U.S. Patent, No. 5369372, 1994.

[Viss11] B. Vissouvanadin, "Matériaux de câble à isolation synthétique pour des applications au transport d'energie HVDC", PhD Thesis Université de Toulouse III, 2011.

[Von 37] A. Von Hippel, "Electrical breakdown of solid and liquid insulators", Journal of Applied Physics, vol.8, pp. 815-832, 1937.

[Vu13] T. T. N. Vu, G. Teyssedre, B. Vissouvanadin, S. Le Roy, C. Laurent, M. Mammeri, I. Denizet, "Electric field profile measurement and modeling in multi-dielectrics for HVDC application", Proceedings IEEE International Conference on Solid Dielectrics, pp. 413–416, 2013.

[Vu14] T. T. N. Vu, "Étude des phénomènes de charges d'espace dans des matériaux de cables et câbles modèles destinés à des applications au transport d'énergie en Haute Tension Continue (HVDC)", PhD Thesis Université de Toulouse III, 2014.

[Vu15] T. T. N. Vu, G. Teyssedre, B. Vissouvanadin, S. Le Roy, C. Laurent, "Correlating Conductivity and Space Charge Measurements in Multi-dielectrics Under Various Electrical and Thermal Stresses", IEEE Transactions on Dielectrics and Electrical Insulation, vol. 22, pp. 117-127, 2015.

W

[Wag14] K.W. Wagner, "Erklärung der dielektrischen Nachwirkungsvorgänge auf Grund Maxwellscher Vorstellungen". Archiv für Elektrotechniek, Vol. 2, pp. 371-387, 1914.

[Whee14] P. Wheeler and S. Bozhko, "The more electric aircraft: Technology and challenges," IEEE Electrification Magazine, vol. 2, pp. 6–12, 2014.

[WPP15] "World Population Prospect: the 2015 Revision", Department of Economic and Social Affairs, Population Division, 2015.

X

Y

[Yaha80] K. Yahagi, "Dielectric properties and morphology in polyethylene", IEEE Transactions on Electrical Insulation., vol. 15, pp.241-250, 1980.

[Yi98] X.-S. Yi, G. Wu, D. Ma, "Properties balancing for polyethylene-based carbon black-filled conductive composite", Journal of applied polymer science, vol. 67, pp. 131-138, 1998.

[Youn11] T.J. Young, M. A. Monclus, T.L. Burnett, W.R. Broughton, S.L. Ogin, P.A. Smith "The use of the PeakForceTM quantitative nanomechanical mapping AFM-based method for high-resolution Young's modulus measurement of polymers", Measurement Science and Technology, vol. 22, no. 125703, 2011.

Z

[Zagh10] U. Zaghloul, G. J. Papaioannou, F. Coccetti, P. Pons, R. Plana, "A systematic reliability investigation of the dielectric charging process in electrostatically actuated MEMS based on Kelvin probe force microscopy", Journal of Micromechanics and Microengineering, vol. 20, no. 064016, 2010.

[Zieg08] D. Ziegler, N. Naujoks, and A. Stemmer, "Feed-forward compensation of surface potential in atomic force Microscopy", Review of Scientific Instruments, vol. 79, no. 063704, 2008

[Zieg11] D. Ziegler and A. Stemmer, "Force gradient sensitive detection in liftmode Kelvin probe force microscopy" Nanotechnology, vol. 22, no. 075501, 2011.

CV and publications

Francesco Gullo was born on the 9th of May 1988 in Catania, Italy. In 2007, he began his studies in Physics at the University of Catania, graduating in 2011 and 2014 respectively with the bachelor's and master's degree. During his studies, he worked for six months as Erasmus Placement guest researcher at the IMEC laboratories in Leuven, Belgium. The researched topic is related to soft matter, interfaces, living cellular and tissue technologies in the group of Dr. Dries Braeken and Dr. Danny Jans.

From 2015 to 2018 he undertook doctoral studies at the University of Toulouse III Paul Sabatier Toulouse, France, in the Diélectriques Solides et Fiabilité research group of the LAPLACE laboratory, under the supervision of. Dr. Gilbert Teyssedre and Dr. Christina Villeneuve-Faure Its Ph.D. project was realized jointly with the research group of Dr. Thomas Christen and Dr. Henrik Hillborg respectively from the ABB Corporate Research centers of Dätwill, Switzerland, and Västeras, Sweden.

In this time, he shed light on the physical process at the interface of a polymer insulation/conductive filler contact. The major contribution of this work is related to the use of Atomic Force Microscopy (AFM) to measure at nanoscale interface properties like: interface roughness, surface potential and from that calculate the electric field and the charge density.

The main results of his research are described in this thesis as well as a number of publications.

Correlated publications:

F. Gullo, T. Christen, C. Villeneuve-Faure, C. Törnkvist, S. Le Roy, C. Laurent, H. Hillborg, G. Teyssedre, "Nano-Scale Characterization of Insulator-Semicon Contacts" IEEE International Conference on Dielectics, pp. 792-795, 2016.

F. Gullo, C. Villeneuve-Faure, S. Le Roy, C. Laurent, G. Teyssèdre, T. Christen, H. Hillborg, "Impact of Press-Molding Process on Chemical, Structural and Dielectric Properties of Insulating Polymers", International Symposium on. IEEE Electrical Insulating Materials, pp. 69-72, 2017.

F. Gullo, T. Christen, C. Villeneuve-Faure, H. Hillborg, C. Laurent, S. Le Roy, G. Teyssedre, "Field and charge distribution at semicon/polyethylene interfaces from combinations of probe force microscopy measurements" 16th International Symposium on Electrets, 2017.

R. Kochetov, T. Christen, F. Gullo, "FTIR analysis of LDPE and XLPE thin samples pressed between different protective anti-adhesive films" 1st International Conference on Electrical Materials and Power Equipment - Xi'an - China, pp. 49-52, 2017.

F. Gullo, T. Christen, C. Villeneuve Faure, H. Hillborg, C. Laurent, S. Le Roy, G. Teyssedre, "Dependence of the field and charge distribution at semicon/polyethylene interface on the press-molding process derived from Kelvin Probe Force Microscopy", Proceeding IEEE Conference on Electrical Insulation and Dielectric Phenomena, 2018

Résumé :

Une des propriétés fondamentales des diélectriques est d'accumuler des charges sous l'effet d'un champ électrique. Si cet effet est exploité dans certaines applications telles que les mémoires il est la plupart du temps la cause de défaillance dans de nombreux systèmes tels que les câbles haute tension ou les microsystèmes. De nombreuses études ont démontré que l'interface entre le diélectrique et l'électrode jouait un rôle prédominant dans le fonctionnement du système complet et en particulier influençait le phénomène d'injection de charge à l'origine des défaillances. Au cours des dernières années le phénomène d'injection de charges à l'interface électrode/diélectrique a largement été étudié. Pour expliquer la différence entre les résultats expérimentaux et les modèles, l'hypothèse la plus plausible est la présence d'états d'interfaces entre l'électrode (métal ou semiconducteur) et le diélectrique. Cette hypothèse permet en particulier d'expliquer l'indépendance de la quantité de charge injectée vis-à-vis du métal servant d'électrode. Toutefois, les propriétés des interfaces restent mal connues en particulier car ces phénomènes nanométriques sont caractérisés à partir de mesures microscopique.

L'objectif de cette thèse est de caractériser les propriétés chimiques et électriques de l'interface grâce à un contrôle rigoureux de son procédé de fabrication. L'apport majeur de ces travaux est lié à l'utilisation de la microscopie à force atomique pour déterminer les propriétés de l'interface à l'échelle nanométrique. Nous avons en particulier caractérisé morphologiquement (mesure de propriétés mécaniques par PFQNM – Peak Force Quantitative NanoMechanical) et électriquement (mesure de potentiel de surface par KPFM – Kelvin Probe Force Microscopy).

Nous avons ainsi pu montrer que le procédé de fabrication influençait les propriétés chimiques (oxydation de surface…) de l'interface sans que cela ait de conséquences notables sur les propriétés électriques. En effet, la quantité de charges injectées reste du même ordre de grandeur quel que soit le procédé de fabrication. Les mesures AFM ont montré que l'interface morphologique était abrupte alors que l'interface électrique était progressive (plusieurs microns). Grâce à un modèle nous avons pu extraire des mesures de potentiel de surface KPFM la densité de charge d'interface.

Abstract :

One of the fundamental properties of dielectrics is to accumulate charges under an electric field. Even if this phenomena is exploited in some applications such as memories, it is the main cause of failure in a large amount of applications such as high voltage cables or microsystems.

Numerous studies have demonstrated that dielectric/electrode interface has strong impact on complete system and particularly on charge injection phenomenon which induce failures.

During the past decades, charge injection phenomena electrode / dielectric interface has been extensively studied. To explain the difference between experimental and modelling, the most plausible hypothesis is the presence of interface states between the electrode (metal or semiconductor) and the dielectric. This hypothesis explain the independence of injected charge density respect to the electrode meta (work function). However, interfaces properties remain poorly understood mainly because all nanometric phenomena accuring at its localization are characterized thanks to microscopic measurements.

The aim of this PhD thesis is to characterize chemical and electrical properties of the interface through a rigorous control of its manufacturing process. The major contribution of this work is related to the use of Atomic Force Microscopy (AFM) to determine interface properties at nanoscale. In particular, interfaces are characterized morphologically (mechanical properties measurements by PFQNM - Peak Quantitative Quantum NanoMechanical) and electrically (surface potential measurements by KPFM - Kelvin Probe Force Microscopy).

Thus, results demonstrate that the manufacturing process influenced the chemical properties (surface oxidation ...) of the interface without having any significant influence on the electrical properties. Indeed, the amount of injected charges remains quite the same regardless of the manufacturing process. AFM measurements showed that the morphological interface was abrupt whereas the electrical interface was progressive (several microns). A Matlab model permits us to extract interface charge density to KPFM surface potential measurements.